Velocity Structure along the Western Trans-Hudson Orogen as Determined from Seismic Refraction Data

By

Denise Thérèse Long

BSc (Honours), University of New Brunswick

A THESIS SUBMITTED IN PARTIAL FULFILLMENT OF

THE REQUIREMENTS FOR THE DEGREE OF

MASTER OF SCIENCE

in

THE FACULTY OF GRADUATE STUDIES

DEPARTMENT OF EARTH AND OCEAN SCIENCES

We accept this thesis as conforming

to the required standard

THE UNIVERSITY OF BRITISH COLUMBIA

April 1998

© Denise Thérèse Long , 1998

In presenting this thesis in partial fulfilment of the requirements for an advanced degree at the University of British Columbia, I agree that the Library shall make it freely available for reference and study. I further agree that permission for extensive copying for scholarly purposes may be granted by the head of my department or by his or her representatives. It is understood that copying or publication of this thesis for financial gain shall not be allowed without my written permission.

Earth and Ocean Sciences

The University of British Columbia

129-2219 Main Mall

Vancouver, BC, Canada

V6T 1Z4

Date: 30 April, 1998

Abstract

During the summer of 1993, a seismic refraction /wide-angle reflection experiment was conducted over the exposed and sediment-covered part of the Paleoproterozoic Trans-Hudson Orogen in Saskatchewan and Manitoba. Three seismic lines, up to 750 km in length, were surveyed. One extended E-W across the orogen, one ran N-S along the eastern central region, and one extended N-S along the western part of the orogen. The latter, Line R3, is the focus of this study. From north to south it crosses exposed Archean rocks of the deformed and reworked Wollaston and Peter Lake domains, the 1855 Ma magmatic arc Wathaman batholith, the Paleoproterozoic metasedimentary Rottenstone domain, the arc-volcanic La Ronge belt and the gneissic-plutonic Glennie domain, and continues south beneath Phanerozoic cover. Based on Archean basement windows and reflection data, the Glennie and adjacent Paleoproterozoic domains are underlain by an Archean microcontinental block, the Sask craton. Principal objectives of the study are to determine the velocity structure of the different domains, crustal thickness and the northward and southward extent of the Sask craton.

The data show very good Pg, Pn and PmP phases which are, respectively, waves turning in the upper crust, below the Moho and reflecting off the Moho. Many sections also show reflections from intracrustal structures. The phases are interpreted through iterative travel time inversion and synthetic seismogram forward modelling for amplitude comparisons to provide velocity structural models. Results show significant lateral variation in velocities and crustal thickness. The crust is thickest ($\approx$ 50 km) below the southern part of the line; it thins rapidly for 200 km to the north until it is less than 40 km thick. Below the exposed Glennie domain, crustal thickness increases to about 45 km; below the domains

to the north, however, it remains near 40 km. Uppermost mantle velocities are generally high, 8.1-8.2 km/s, but in one region below the Phanerozoic cover where crust is thinnest, well constrained values of 8.5 km/s are determined. This region lies below Prince Albert in the area where diamondiferous kimberlites have been found. Similar results, high uppermost mantle velocities associated with regions of diamondiferous kimberlites, have been documented in Russia.

The velocity structure sections are compared to nearly coincident reflection data collected in 1994. Generally, there is good agreement between characteristics of the velocity models and the reflections sections. Somewhat higher lower crust velocities for the Sask craton tend to end below the La Ronge-Rottenstone domains, indicating the northern limit of the Sask craton (and consistent with interpretations from the reflection data). Three relatively higher lower crustal velocities extend southward to the end of the line, indicating the southward continuation of the Sask craton.

Variations of the crustal thickness and upper mantle velocities are explained by the process of eclogitization in which lower-density, lower-velocity materials in the lower-most crust are metamorphosed to high-density, high-velocity materials. Exactly why this occurs in this particular region is uncertain. Perhaps the thrusting of the thick (?) Archean craton alters the state of the lower crust making it more susceptible to eclogitization. Much further study is needed to justify this hypothesis.

Contents

List of Tables

List of Figures

Acknowledgement

Many thanks to:

The participants of the Trans-Hudson Orogen Experiment for making the project a success and a lot of fun to be on. THORE was funded through NSERC Lithoprobe funds. Analysis support came from NSERC research grants to R.M. Clowes and R.M. Ellis.

Charly Bank, Andrew Gorman, John Amor, Holger Mandler, Dave Baird and Phil Hammer without whom this thesis would have not materialised. Their willingness and enthusiasm to help have saved my sanity many times.

Ron Clowes, Bob Ellis and Michael Bostock for reading this thesis at the very last minute when they could easily have said no. I am truly grateful.

Everyone in the Geophysics department for your friendship and support through very difficult times. You have made me smile when I needed it the most. To you all, a great big hug!

Charly, Katharina and Johnathan, Andrew and Sandy (and Kyle), and Olga whose couches proved to be very comfy.

A very special thanks to Pete, Mrs Joel, G.C. and M. for giving me the courage to continue...

À Dave, Mindy et Amy,

sans qui, je ne serais pas ici

1 Introduction

The Trans-Hudson Orogen (THO) is the remnant of an ancient orogenic belt developed during the closing of the Manikewan ocean at $\approx$ 1890-1835 Ga (Stauffer, 1984; Van Schmus et al., 1987). It is the largest and best preserved orogenic belt of a network of orogens accommodating early Paleoproterozoic assembly of much of the North American continent. It extends from the eastern end of Hudson Bay, through Manitoba and Saskatchewan and terminates in North Dakota (Fig. 1.1). Geologically, it lies between the Rae-Hearne and Superior cratons (Hoffman, 1988; Bickford et al., 1990) and is believed to be 'bound' to the south by the Sask craton (Ansdell et al., 1995).

To better understand the structure and evolution of the North American continent, *LITHOPROBE* (a national multidisciplinary Earth Science program) is studying characteristic geological regions in Canada. Recognising the importance of the THO in the assembly of North America, *LITHOPROBE* selected the THO as one of its ten principal study areas within Canada (Clowes, 1993). The broad objective of the THO study is to improve the understanding of the tectonic processes that occurred during the early Proterozoic by utilising a broad array of multidisciplinary investigations to: a) locate the buried margins of Archean crust below juvenile rocks of the internal zone; b) ascertain the extent to which postulated subduction polarity governed deep crustal orogenic structure; c) determine the three-dimensional geometry of major shear zones and domain boundaries; and d) compare and contrast features of THO with present day orogens such as the Himalayas. The various studies conducted in the region include: seismic reflection and refraction, gravity, magnetics, surface geological mapping, heat flow analysis, paleomagnetism, geochronology, geochemistry and igneous and metamorphic petrology.

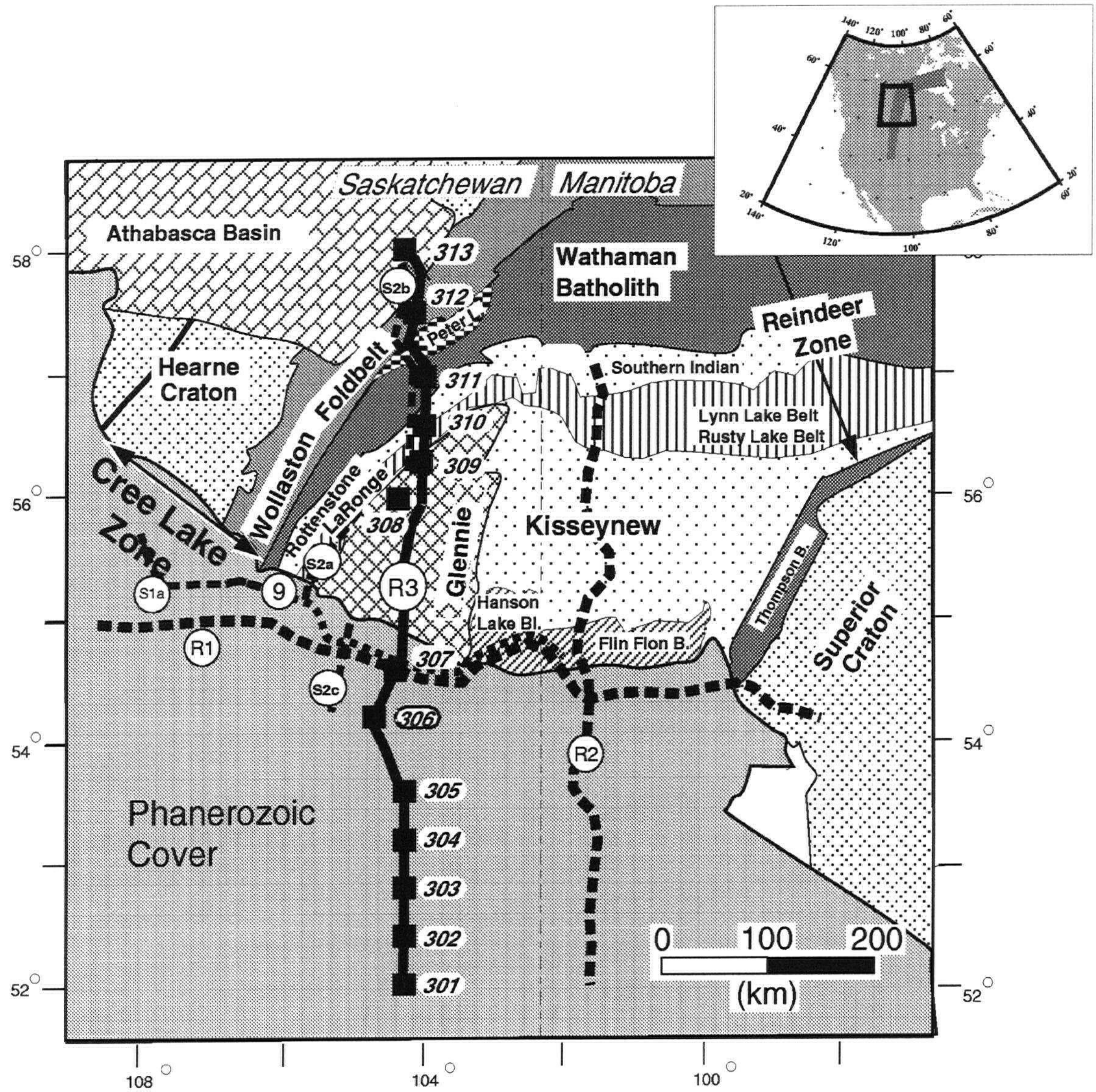

Figure 1.1: Simplified tectonic sketch of the Trans-Hudson Orogen within Manitoba and Saskatchewan. Solid line represents the R3 refraction line. The large dotted lines show the locations of refraction lines R1 and R2. The smaller dotted lines represent reflection lines 9, S1a, S2a, S2b and S2c. Shot locations for R3 are shown as black squares. Inset shows the entire extent of the THO on the North American continent.

In 1993, a large wide-angle reflection and refraction experiment was conducted in northern Saskatchewan and Manitoba. Three lines were shot, two extending ~700-750 km (R1, oriented east-west, and R3, oriented north-south), and one, R2, running ~550 km north-south (Fig. 1.1). The objective of this thesis is to construct a representative crustal velocity model for line R3 which will indicate the variations in crustal thickness as well as determine the north and south boundaries of the Sask craton. Various techniques such as raytracing, eigenimaging and relative true and synthetic amplitude comparisons are used. In turn, this will provide a more constrained velocity structure of the area and will add to the understanding of its tectonic history.

1.1 General Geology of the Area

The Canadian section of the THO in eastern Saskatchewan and western Manitoba, ≈ 49-60°N and 089-110°W (Fig. 1.1), is discussed in this study. It is exposed north of 54-55°N and is overlain to the south by Phanerozoic sediments increasing in thickness from 0 to a maximum of 3 km at the Canadian-American border.

Within the study area, the THO can be divided from east to west into four composite lithotectonic zones comprising the Thompson, Reindeer, Wathaman batholith and Cree Lake zones (Fig. 1.1) (Hoffman, 1989; Lewry and Stauffer, 1990; Lewry and Collerson, 1990; Lewry et al., 1994).

The Thompson belt is composed of reworked Archean basement gneisses of the adjacent

Pikwitonei terrain which is a high grade segment of the western edge of the Archean Superior province. The Thompson belt also contains metasediments and mafic rocks which are thought to be continental margin deposits in a narrow foreland zone.

The Reindeer zone is a collage of arc-related volcanic and plutonic rocks associated with volcanoclastic sediments, arkosic molasse and late post-kinematic intrusions derived from oceanic arc or back arc settings (Walters and Pearce, 1987; Syme, 1990; Stern et al., 1992). This zone is divided from east to west into different domains consisting (Fig. 1.1) of the : Kisseynew, turbiditic greywackes presumably deposited in a marginal basin (Zwanzing, 1990); Flin Flon, island arc and back-arc assemblages and alluvial-fluvial sedimentary rocks (Bailes and Syme, 1989; Syme, 1990); Glennie and Hanson Lake juvenile arc, oceanic, basinal sedimentary, and plutonic rocks (Gordon et al., 1990, Lewry et al., 1990); LaRonge-Lynn Lake, abundant metavolcanic rocks with subordinate metasediments to the west and of high-grade metasedimentary migmatites to the east (Lewry et al., 1994); and Rottenstone-Southern Indian domains (Lewry et al., 1994), deformed granitoid rocks. Both the Glennie and Hanson Lake domains contain basement windows of Archean rock. Drill cores beneath the Phanerozoic cover also contain rocks of the same age (Collerson et al. 1990) indicating Archean rocks may underlie some or most of the Reindeer zone. Further details on the origin of these domains and Archean rocks will be discussed in section 1.2.

The Wathaman-Chipewyan batholith is a homogeneous continental margin batholith surrounded by reworked Archean basement, Proterozoic metasedimentary rocks of the Cree Lake zone and the juvenile terrains of the Reindeer zone. It is generally comprised of a granitic plutonic complex with calkalkaline geochemical signature (Lewry et al., 1981;

Halden et al., 1990; Meyers et al., 1992). The batholith is considered to be the product of westward subduction between the LaRonge arc and the continental margin (Bickford et al., 1990).

The Cree Lake zone consists mainly of reworked Archean basement (Lewry and Sibbald, 1980) and is believed to be a broad reworked hinterland created during the final episode of subduction (Lewry and Collerson, 1990).

1.2 Tectonic Evolution of the Trans-Hudson Orogen

Lewry (1981) was one of the first to postulate a collisional history for the THO. He recognised juvenile crust and various other types of rocks and structures associated with orogens. Since then, many studies have been undertaken to comprehend the tectonics that formed the THO approximately two billion years ago (Lucas et al., 1993; Baird et al., 1995). The latest tectonic interpretation (Fig. 1.2) presented to the scientific community is a combination of theories by Lewry et al. (1996) and Andsell et al. (1995) describing the processes which may have led to the present-day structure of the THO.

Approximately 2.1 Ga ago, a supercontinent, speculated to be the Kenoran (Aspler and Chiranrenzelli, 1996), began to rift forming the Manikewan ocean. The ocean spread and is thought to have reached a maximum width of 5000 km (Stauffer, 1984; Van Schmus et al., 1987) after which it began to close as the Superior margin moved northward. From 1.970-1.870 Ga, many subduction-related ocean arcs, such as the LaRonge, Lynn Lake, Flin Flon and Snow Lake arcs, developed (Fig. 1.2). The Wollaston passive margin was

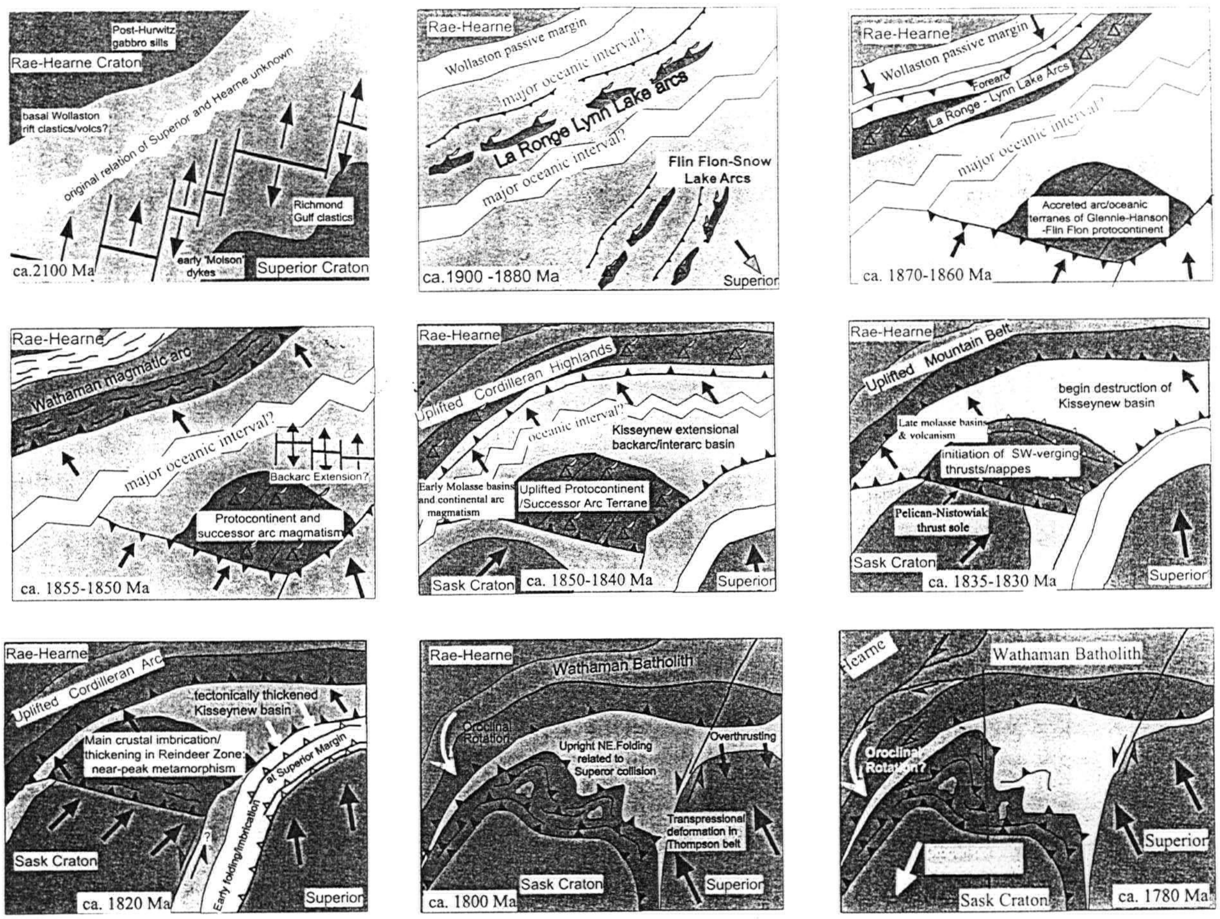

Figure 1.2: Preliminary summary of the tectonic evolution of the Trans-Hudson Orogen for the period 2100 Ma to 1780 Ma. See text for discussion. (From John Lewry, University of Regina, pers. comm., 1997; developed for synthesis of THOT)

at this time (Fig. 1.2). The Rae-Hearne craton commenced its shift towards the south-east at approximately 1.870-1.860 Ga and oceanic subduction created the LaRonge and Lynn Lake arcs (Fig. 1.2). During this time, the Glennie, Hanson, and Flin Flon arcs (GHFF) and Flin Flon arcs (GHFF) were accreted to form a proto-continent. At 1.860 Ga, the LaRonge-Lynn Lake arcs collided with the Rae-Hearne and subduction polarity changed to the north-west (Fig. 1.2) from which the Wathaman batholith started to develop. The initiation of the Kisseynew basin by back arc spreading occurred at approximately 1.855 Ga (Fig. 1.2).

Final closure of the Manikewan ocean commenced from 1.850-1.835 Ga, thus initiating the collisional features preserved today. At this point, subduction adjacent to the GHFF proto-continent changed polarity to the north-east and north-west forming arcs on GHFF (Fig. 1.2) which began to lift due to the impact of the Sask craton from the south-west. The LaRonge and Lynn Lake arcs also were uplifted as the ocean closure continued. Near 1.835-1.820 Ga, the Kisseynew basin was destroyed. The final stages of closure of the Manikewan ocean occurred from 1.820-1.805 Ga, and caused the main crustal imbrication/thickening and peak metamorphism in the Reindeer zone as well as some early folding/imbrication at the Superior margin (Fig. 1.2). Terminal closure accompanied by transpression and strike -slip faulting was complete by approximately 1.800 Ga although some convergence and thrusting continued. Post-collisional erosion, cooling and thermal equilibrium followed (Fig. 1.2).

1.3 Previous Geophysical Studies of the THO

To understand the nature of the THO, many studies have been undertaken over the past couple of decades. In the following subsections, only those pertaining to the crustal structure of the western THO will be described.

1.3.1 COCRUST Refraction Experiment

During the late 1970's and early 1980's, the Consortium for Crustal Reconnaissance Using Seismic Techniques (COCRUST) conducted seismic refraction experiments in south-central Canada. Approximately 2250 km of in-line reversed refraction data were recorded along eight profiles (Fig. 1.3). The crustal structure and respective velocities of lines D and E are shown in Figures 1.4 and 1.5 (Morel-à-l'Huissier et al., 1987). They found average velocities of approximately 6.12, 6.41 and 7.10 km/s for the upper, mid- and lower crust respectively. Crustal thicknesses range from 40-45 km thinning towards the south. Upper mantle velocities were determined at 8.4 km/s. The models are not very well constrained however, due to limitations in data acquisition (such as large, uneven instrument spacing), but they give a preliminary view of the crustal structure in the western section of the THO. The results from this study will be given in greater detail and compared to the crustal structure derived from this thesis in Chapter 6.

1.3.2 THOT Reflection Study

In 1991 and 1994, more than 2000 km of vertical-incidence seismic reflection data were collected as part of the *LITHOPROBE* project (Clowes, 1993). The locations of reflection lines 9, S1a, S2a, S2b and S2c of this study are shown in Figure 1.1. Line 9 cuts the THO perpendicular to strike and images a crustal thickness ranging from approximately 41-43 km and a 50 km-wide crustal root extending 38-48 km in depth (Fig. 1.6) (Lucas et al., 1993). The block including the root is believed to comprise mid-to-late Archean rocks as

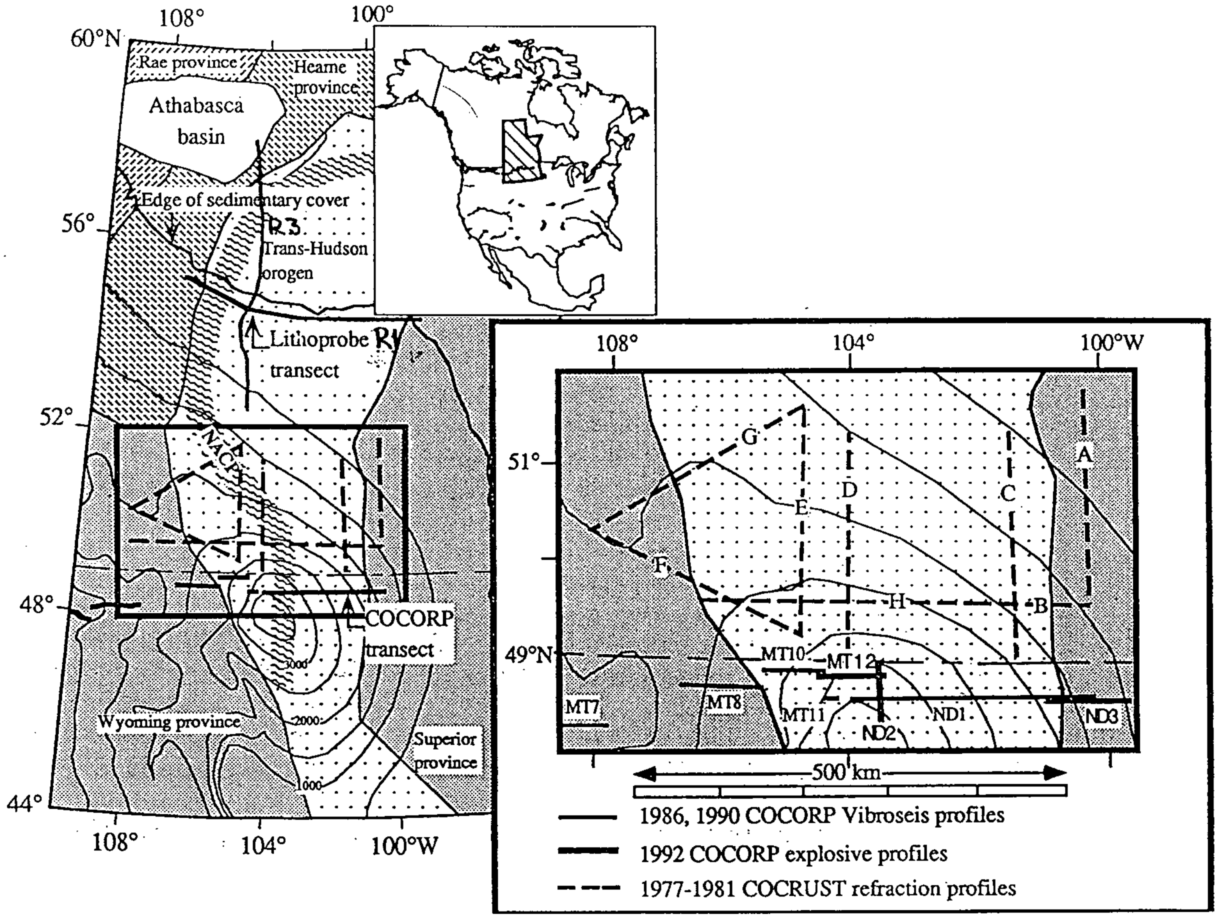

Figure 1.3: Locations of COCORP deep seismic reflection profiles and COCRUST seismic refraction profiles across Trans-Hudson Orogen and Williston Basin. Contours (500 m interval) are to top of Precambrian basement. NACP is North American Central Plains conductivity anomaly (Baird et al., 1995)

evidenced by such rocks found in basement windows of the Glennie domain and in drill cores beneath the Phanerozoic cover (Collerson et al., 1988, 1990). Lines 2a, 2b and 2c

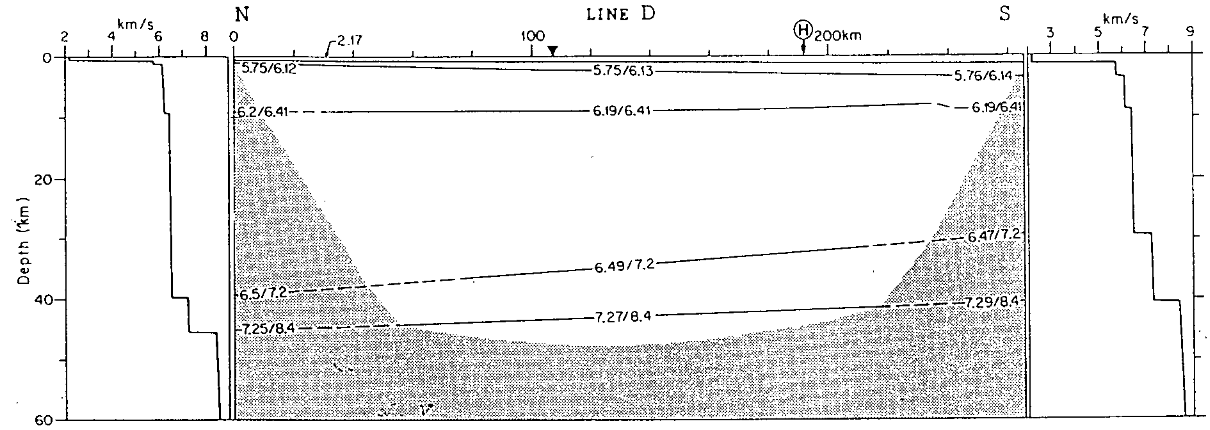

Figure 1.4: Final crustal model for line D. Velocities in kilometres per second indicate values above/below the interface. Solid lines are interfaces for which reflections exist. Dashed lines represent the extension of the boundaries as used by the modelling program. The shaded area indicates zones that have not been investigated by modelling. Vertical exaggeration 2:1. The velocity function for each of the extremities is also given (Morel-à-l'Huissier et al., 1987).

run north-south in proximity to line R3. Final interpretations of these data have not been published at present, but initial results show varying crustal thicknesses ranging from 36-45 km. More detail will be presented in Section 6.1.2 where the results will be compared to the crustal model of this thesis.

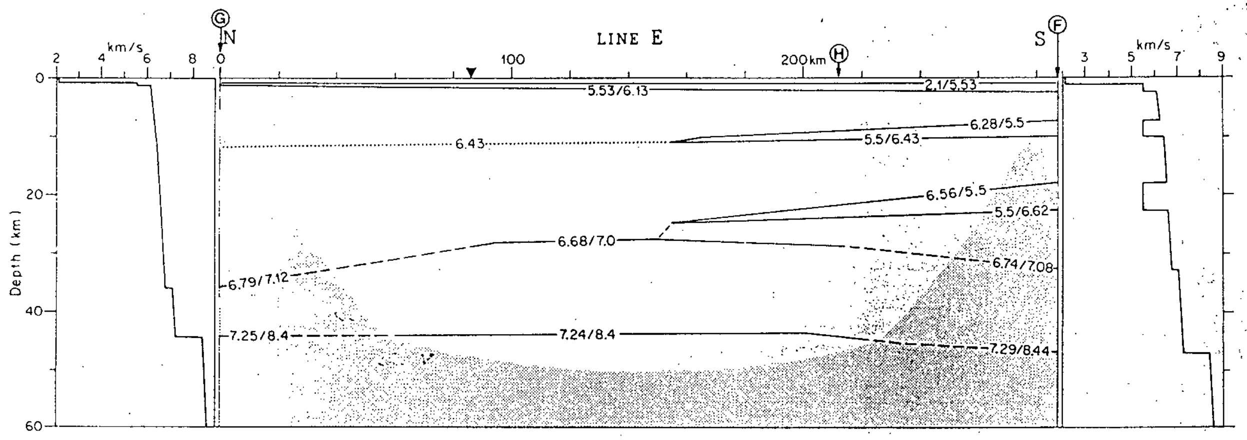

Figure 1.5: Final crustal model for line E. Velocities in kilometres per second indicate values above/below the interface. Solid lines are interfaces for which reflections exist. Dashed lines represent the extension of the boundaries as used by the modelling program. Dotted line shows a change in the gradient. The shaded area indicates zones that have not been investigated by modelling. Vertical exaggeration 2:1. The velocity function for each of the extremities is also given (Morel-à-l'Huissier et al., 1987).

1.3.3 COCORP Reflection Experiment

In the summer of 1990, COCORP (Consortium for Continental Reflection Profiling) collected approximately 400 km of Vibroseis seismic reflection data across the Williston Basin in Montana and North Dakota (Fig. 1.3). Final interpretation of this study is shown in Figure 1.7 and is similar to the results found in the*LITHOPROBE* 1991 reflection survey (Fig. 1.6). One major difference, however, is the reflectivity of the Moho (at ≈ 45 km) between the two surveys. *LITHOPROBE* lines have a much higher Moho reflectivity than that

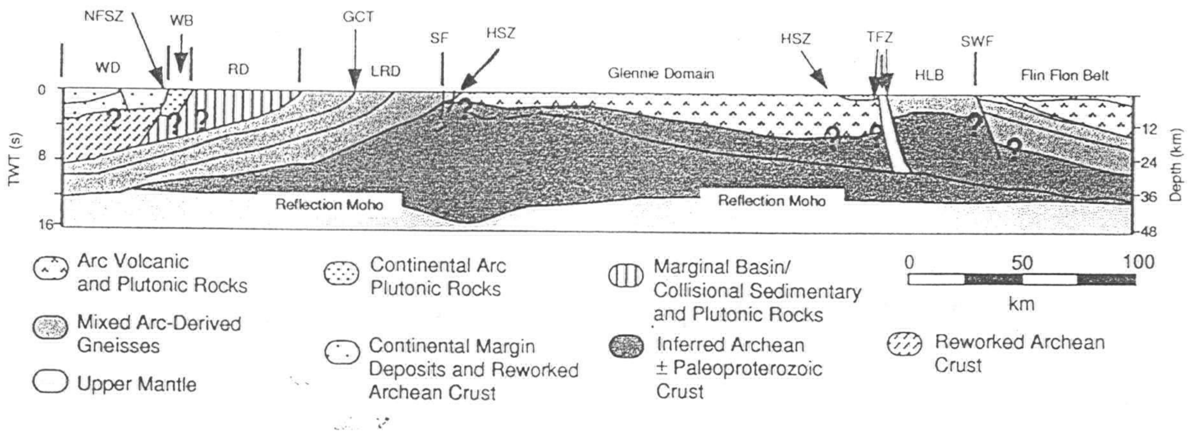

Figure 1.6: Geological cross section showing the principal tectonostratigraphic units of the Trans-Hudson Orogen as constrained by THOT reflection profile 9. WD = Wollaston domain, RD = Rottenstone domain, LRD = LaRonge domain, HLB = Hanson Lake block, NFSZ = Needle Falls shear zone, WB = Wathaman batholith, GCT = Guncoat "thrust", SF = Stanley fault, HSZ Hartley shear zone, TFZ = Tabbernor fault zone, SWF = Sturgeon Weir fault. (Lucas et al., 1993).

of the COCORP experiment. Baird et al. (1995) attribute this difference to the eclogitization of the older crustal keel which in turn initiated the subsidence forming the Williston Basin. This will be discussed in greater detail in Chapter 6.

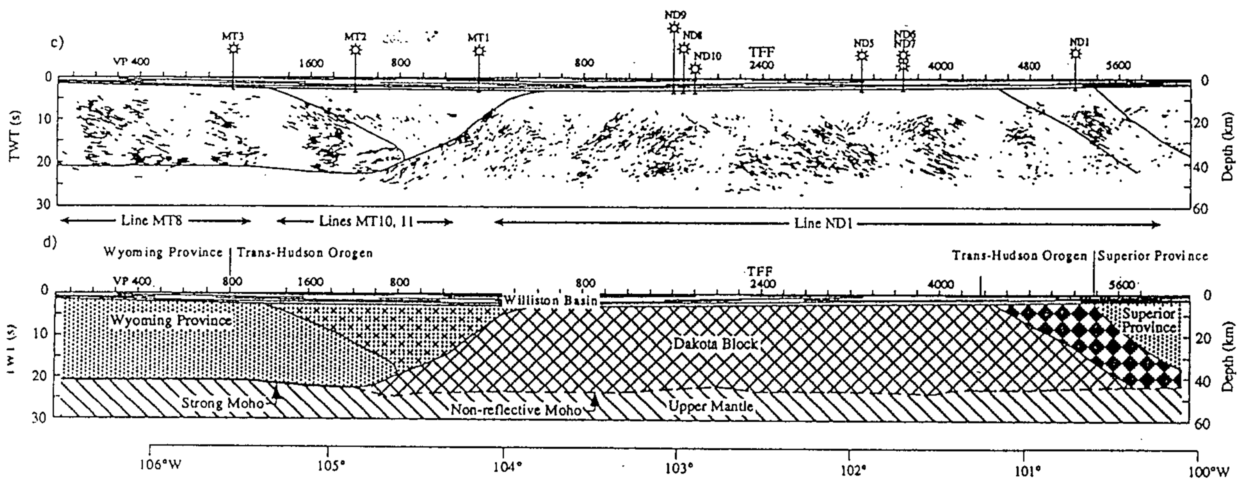

Figure 1.7: COCORP interpretation from reflection data. Data set reveals west-dipping structures in the western part of the Orogen and east-dipping structures in the eastern part of the Orogen, similar to the *LITHOPROBE* reflection interpretation of Line 9 (Baird et al., 1996).

2 THO Wide-Angle Reflection and Refraction Experiment

During the last two weeks of July 1993, the Trans-Hudson Orogen Wide-Angle Reflection and Refraction Experiment (THORE) was conducted in western Manitoba and eastern Saskatchewan. The objective was to a) outline the broad crustal framework of the THO, b) determine the velocity structure of tectonic elements, c) delineate the deep crustal signature of the Rae-Hearne and Superior boundary zones, and d) complement the seismic reflection surveys conducted in 1991 and 1994 (section 1.3.2). Over fifty scientists from the Geological Survey of Canada (GSC), the United States Geological Survey (USGS), IRIS/PASSCAL, and the Universities of Alberta, British Columbia, Duke, Saskatchewan and Victoria participated in the project.

2.1 The Three Transect Lines

Three lines were surveyed across the THO: R1 ran east to west on the southern end of the transect, R2 ran north-south on the eastern section of the THO, and R3, also north-south, was shot in the western section (Fig. 1.1).

Line R1 extends 750 km perpendicular to the strike of the domains and is adjacent to some of the reflection lines surveyed in 1991 and 1994. Line R2, 550 km long, transects the Paleoproterozoic oceanic rocks of the Flin Flon and Lynn Lake belts and the Kisseynew domain. The main focus of this analysis, however, is line R3. It extends 750 km crossing the Wollaston, Peter Lake, Rottenstone, LaRonge and Glennie domains and continues over the Phanerozoic cover.

2.2 Shot Points and Instrumentation

The sources were chemical charges of 800-3000 kg in a TNT based slurry in boreholes 43-60 m deep and spaced at $\approx$ 50 km. Lines R1, R2 and R3 had fifteen, twelve and thirteen shots respectively. All receiver and shot sites were located by Global Positioning Satellite (GPS). The accuracy of the site positions are $\pm$ 5 m horizontally and $\pm$ 10 m vertically.

Three types of seismographs were used to record the data: Portable Refraction Seismographs (PRS), Seismic Group Recorders (SGR) and REFTEK. The instrumentation set-up is shown in Table 1.

The internal clocks of all instruments were synchronised to a Geocentric Orbiting Earth Satellite (GOES) clock to provide an initial time base accurate to $\pm$ 1 ms. Clocks drifts were corrected before merging the data into SEG-Y format. Combined clock and instrument timing errors are $\approx$ 0.005 sec, which is a scale factor smaller than the phase picking errors and thus are not a concern for this thesis.

Instrument name	Number	Geophone name	Supplied by
PRS-1	185	2 HZ Mark Products L4A	GSC
PRS-4	35	2 HZ Mark Products L4A	
SGR	185	4 HZ L28 LBH (135) single 2 HZ (50) 8 HZ strings	USGS
Reftek	120		IRIS/PASSCAL

Table 1: Instrumentation for 1993 THORE experiment.

3 Data Processing

The data quality of the profiles is generally good considering the large offset distances of up to 750 km. Prior to interpretation, the data were reduced by 8 km/s, truncated to -5 to 55 seconds, resampled to 125 Hz and finally merged before being transferred onto exabyte tape in SEG-Y format. Further processing details can be found in Bzdel et al., 1995. The PRS and SGR instruments had data recovery of over 95%; however, the REFTEK data recovery along line R3 was only 50% and is thought to have been caused by assigning inappropriate record time windows during initial programming. Thus, many traces are missing in the northern section of line R3. Nevertheless, since the thirteen shots span the whole line, complete coverage of the profile was available and a model could be constructed representing the whole profile.

3.1 Processing Routines

To interpret the thirteen sections of line R3, the routines of 'plotsec' (Amor, 1996) were used to manipulate the data. Originally developed to create true distance plots of refraction data, it performs the following processes: automatically updates parameters in the SEG-Y header file, bins and stacks data, picks phases interactively, applies variable velocity reductions, merges multiple data sets in time and/or offset, reads/writes SEG-Y files and plots screen/hardcopy sections by offset or azimuth. These routines are described in detail in Appendix A.

3.2 Filtering

The noisy and dead traces were selected manually using the plotsec_pick routine and were eliminated from the section using plotsec_filt. No bandpass filtering was applied to this data set since no benefit was observed when initially viewing the data.

3.3 True Relative Amplitude Sections

Scaling within the true relative amplitude sections was necessary to compensate for the different instruments used. The PRS-1 data was scaled by 0.8; PRS-4 by 0.5; SGR by 0.1 and the REFTEKS by 5.5. These scaling corrections were chosen by trial and error according to the improvement in the visual appearance of the data, and consistency at the change of instrument types.

To correct for the decrease in amplitude with offset, each trace was multiplied individually by their source-receiver distance raised to the power 1.55. This value was selected according to the visual appearance of the section in which the strength of the signal at further offsets was relatively similar to that near the shot point.

3.4 Eigenimaging

The majority of seismic refraction sections for line R3 show a good upper mantle reflection. However, in some cases it is difficult to select this phase with certainty. Eigenimage analysis (Ulrych et al., 1998) was applied to most sections to decrease picking error. This procedure had never been previously applied to seismic refraction data and thus additional development was required. Full details are described in the following chapter.

4 Eigenimage Analysis Applied to Seismic Refraction Data

Of the many phases that can be seen in seismic refraction profiles, arrivals reflecting off the Moho, PmP, best give an indication of crustal thickness. However, these phases are sometimes difficult to distinguish from other phases and/or noise. In this chapter, a particular application of covariance analysis of seismic sections, called eigenimaging, will be discussed as a method of improving the identification of this particular event.

4.1 Theory of Eigenimaging

Typically, the Karhunen-Loève (KL) transform is used for one- or two-dimensional data compression and pattern recognition (Loève, 1951; Anderson, 1971). However, eigenimaging has been proven to be more efficient in the seismic case for it uses Singular Value Decomposition (SVD) instead of the KL transform. SVD could be called a partial KL transform since it is calculated using the zero-lag covariance matrix derived from the KL transform. The advantage of using SVD is that the original image can be obtained using only a few eigenvectors, whereas the KL transform would require an evaluation and sum of all the time series. A more detailed explanation of the differences between the two methods can be found in Ulrych et al. (1998).

The eigenimage method decomposes a matrix (in this case a seismic section) into a weighted sum of orthogonal rank one matrices called eigenimages. Each one of these images will emphasise a particular feature of the section, whether it be signal or noise. For example, a matrix X has M traces (rows of X) and N data points per trace. The equation for the SVD would be as follows:

$$\boldsymbol{X} = \sum_{i=1}^{r} \sigma_i \boldsymbol{u}_i \boldsymbol{v}_i^T \tag{4.1}$$

where r is the rank of matrix $\boldsymbol{X}$, $\boldsymbol{u_i}$ is the $\boldsymbol{i}$ th eigenvector of $\boldsymbol{XX^T}$, $\boldsymbol{v_i}$ is the $\boldsymbol{i}$th eigenvector of $\boldsymbol{X^TX}$ and $\boldsymbol{\sigma_i}$ is the $\boldsymbol{i}$th square root of eigenvalues of $\boldsymbol{U}$ and $\boldsymbol{V}$ or the $\boldsymbol{i}$th singular value of $\boldsymbol{X}$.

It is obvious from Equation 4.1 that the eigenimage depends on the magnitude of $\boldsymbol{\sigma_i}$. If all the traces were linearly independent, all of the eigenvectors and singular values would be needed to reproduce the initial image since the values would be very similar. But, if all the traces were linearly dependent, the original image could be reproduced using only one singular value. Generally, the data lie somewhere in the middle of these extremes and thus the first few eigenimages are usually needed to obtain the desired picture.

The success of the eigenimaging depends on the horizontal coherency of the traces. Thus if the feature of interest is dipping, the traces must be shifted to obtain the desired horizontal coherency. In this study, the features were shifted manually to a specific time as shown in the following sections.

4.2 Eigenimaging of Synthetic Data

Before eigenimaging real data, a synthetic seismic section was created to determine whether eigenimaging is possible and useful for this type of data set and to set up some general procedures.

4.2.1 Generation of Synthetic Data

A synthetic seismic section (Figure 4.1 a) was generated using the forward modelling program of Zelt and Ellis (1988) for a crustal model which is expected to be similar to the properties of the area. An initial wavelet vector, w=0...,0,1,-1.5,1,-1,0.33,0...,0 is assumed according to first arrival wavelets in the THORE data, but it is impossible to ascertain if this is an accurate replica of the true input wavelet; however, for the purposes of this experiment, it will suffice. Phases refracting through the crust (Pg), reflecting off the Moho (PmP) and refracting within the upper mantle (Pn) are used for this eigenimage study.

The synthetic section was converted to a matrix and sampled to 0.01 s compared with 0.008 s for the observed data. However, for crustal velocities between 4-8 km/sec, the time difference of 0.002 seconds would only cause an error in depth of 8-12 metres which is negligible for the scale of this study.

4.2.2 Phase Shifting and Noise Addition

The phase under consideration must lie horizontally to determine its horizontal coherence dependency. The shifts, in which the signal of a particular phase is shifted to a common time, are shown in Figure 4.1 b, c and d.

To obtain more realistic sections, white random noise was added to the original as well as the shifted synthetic traces. Figure 4.2 shows the original synthetic plot with added noise

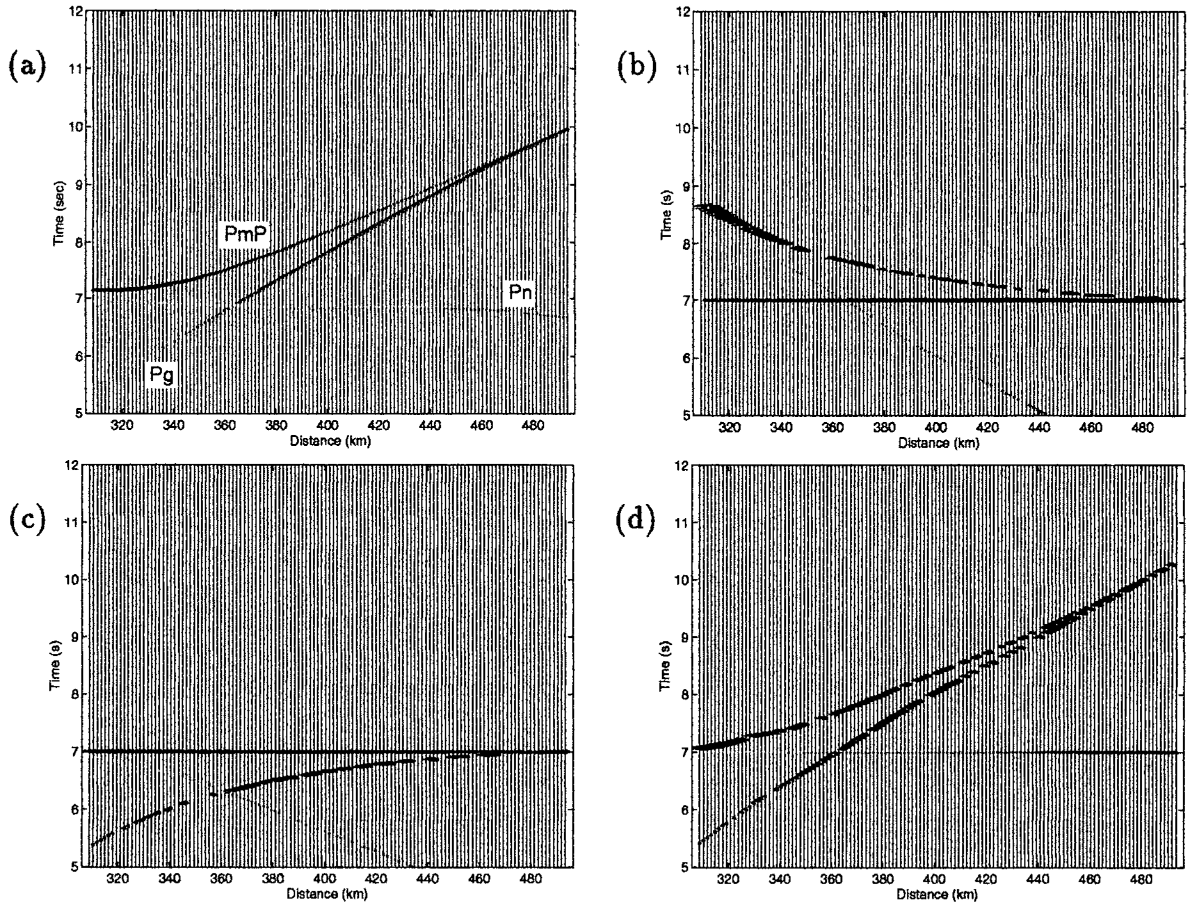

Figure 4.1: Synthetic section: a) original Pg, PmP and Pn phases, b) shifted Pg phase, c) shifted PmP phase and d) shifted Pn phase. The phases were shifted to 7 seconds.

and the shifted phases with the added noise. The relative strength of the signal and noise is similar to a recorded refraction section.

4.2.3 Eigenimaging

The singular values of the Pg, Pn and PmP arrivals were determined and are shown in Figure 4.3 a, b and c respectively. For the Pg and PmP phases, one singular value is much

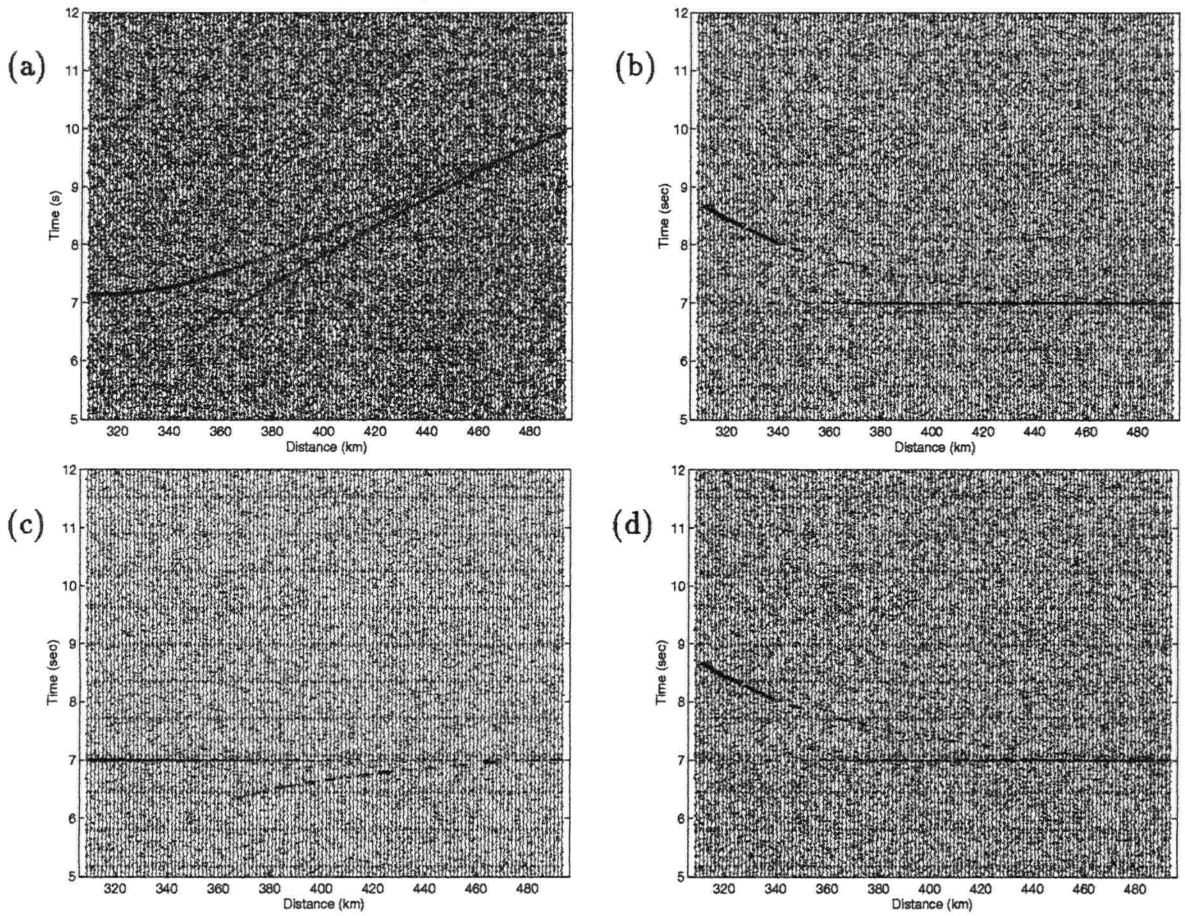

Figure 4.2: Shifted images with noise. a) original non-shifted section, b) shifted Pg, c) shifted PmP and d) shifted Pn. Phases were shifted to 7 seconds.

greater than the others, but there is not a large difference between the first few singular values of the Pn phase. This is most likely due to its smaller amplitude. As mentioned in section 4.1, a particular singular value will greatly influence the resulting eigenimage. To demonstrate this, the Pg phase was eigenimaged using the first three singular values of 50.5817, 37.5037 and 37.2520. From the results shown in Figure 4.4 a, b and c, it is clear the first singular value represents the signal whereas the other two depict the noise. The same test was done with the other phases with the same results, even with Pn for which

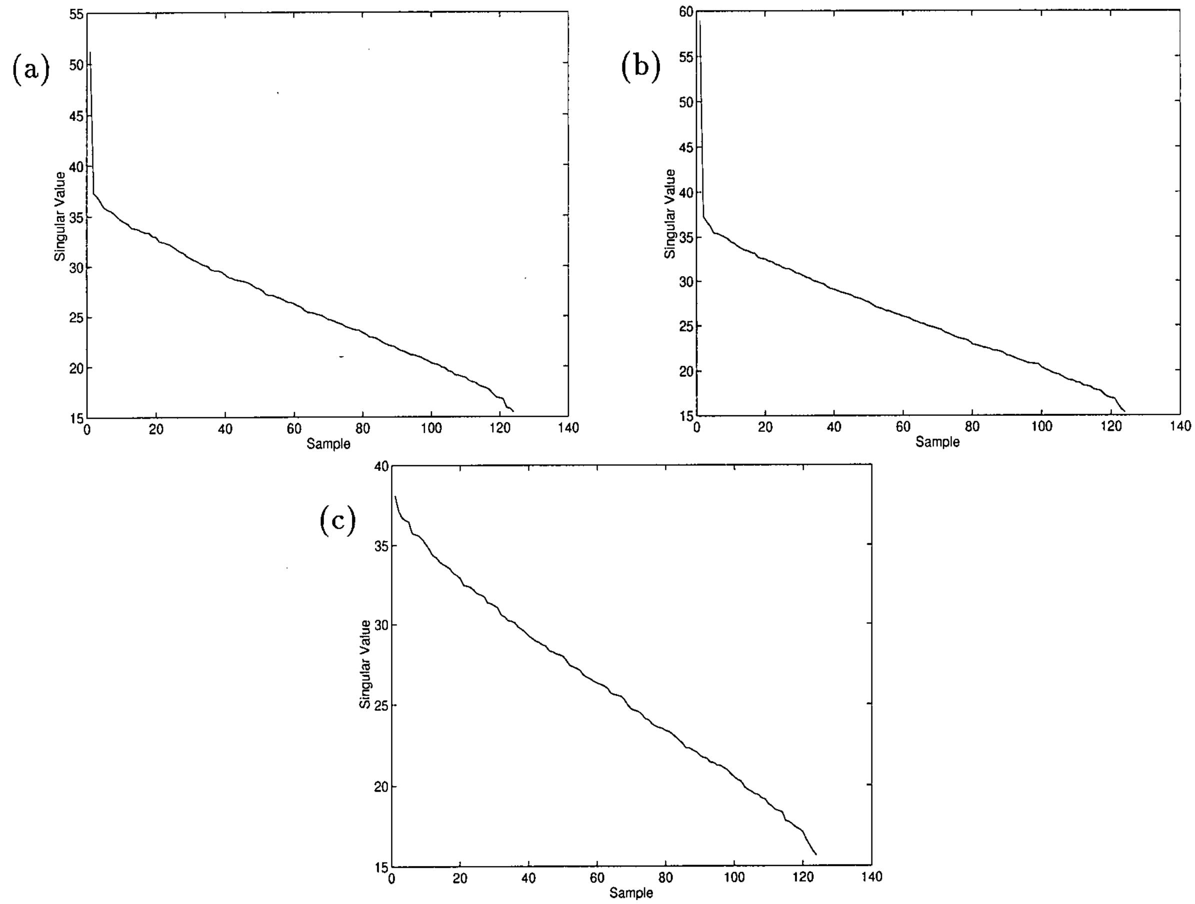

Figure 4.3: Singular values for a) Pg, b)PmP and c) Pn.

the first three singular values are similar.

Once the eigenimages were constructed, the individual phases were reshifted to their original positions as depicted in Figure 4.5 a, b, and c. In all cases, there is significant noise reduction and good retrieval of the original signals. Note particularly the Pn phase. It was greatly obscured by the noise but is now very apparent. The three eigenimages were summed together and the final result is shown in Figure 4.5 d. There is a clear difference between the original synthetic section with added noise and the final eigenimage. The

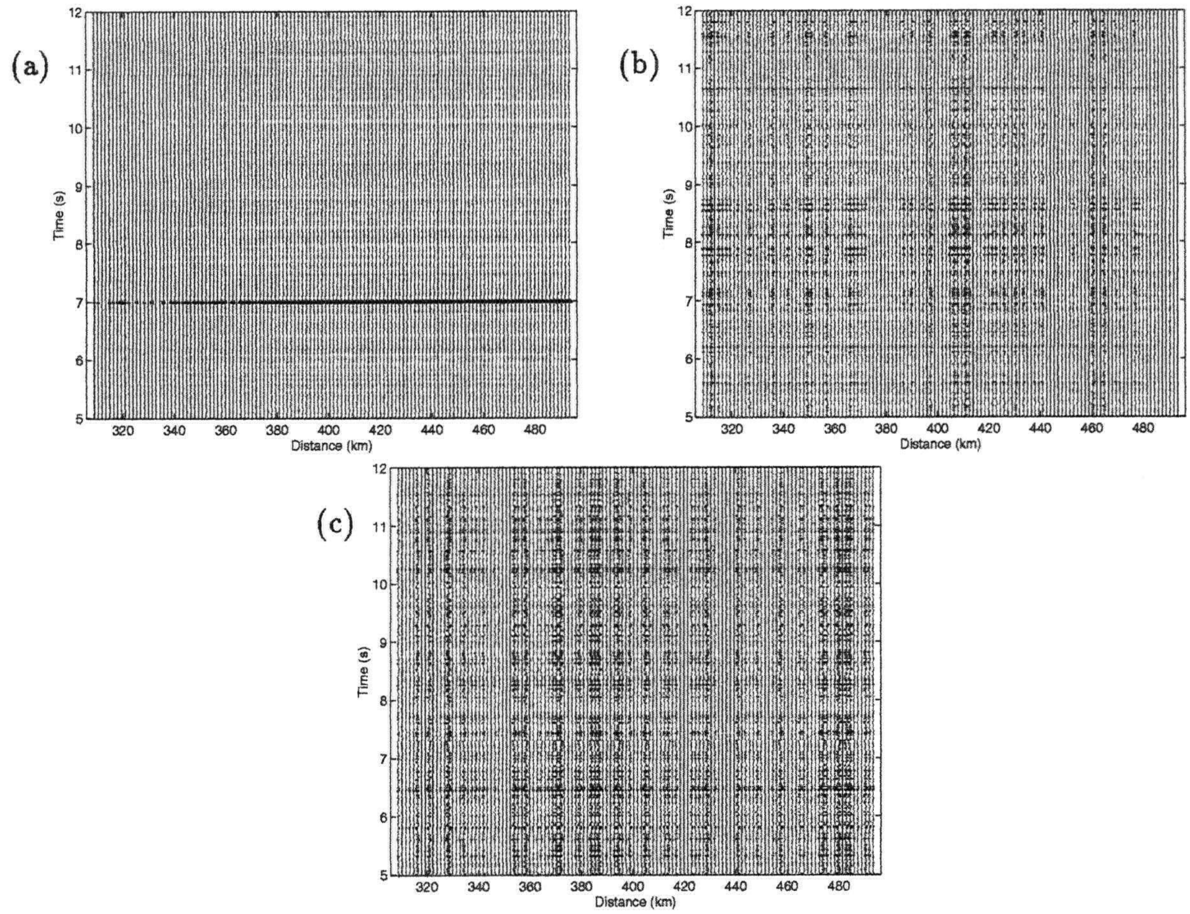

Figure 4.4: First three eigenimages of Pg: a) 50.5817, b) 37.5037 and c) 37.2520

arrivals are much clearer and noise is greatly attenuated. Such improvement suggests that the real data may be significantly improved by this procedure.

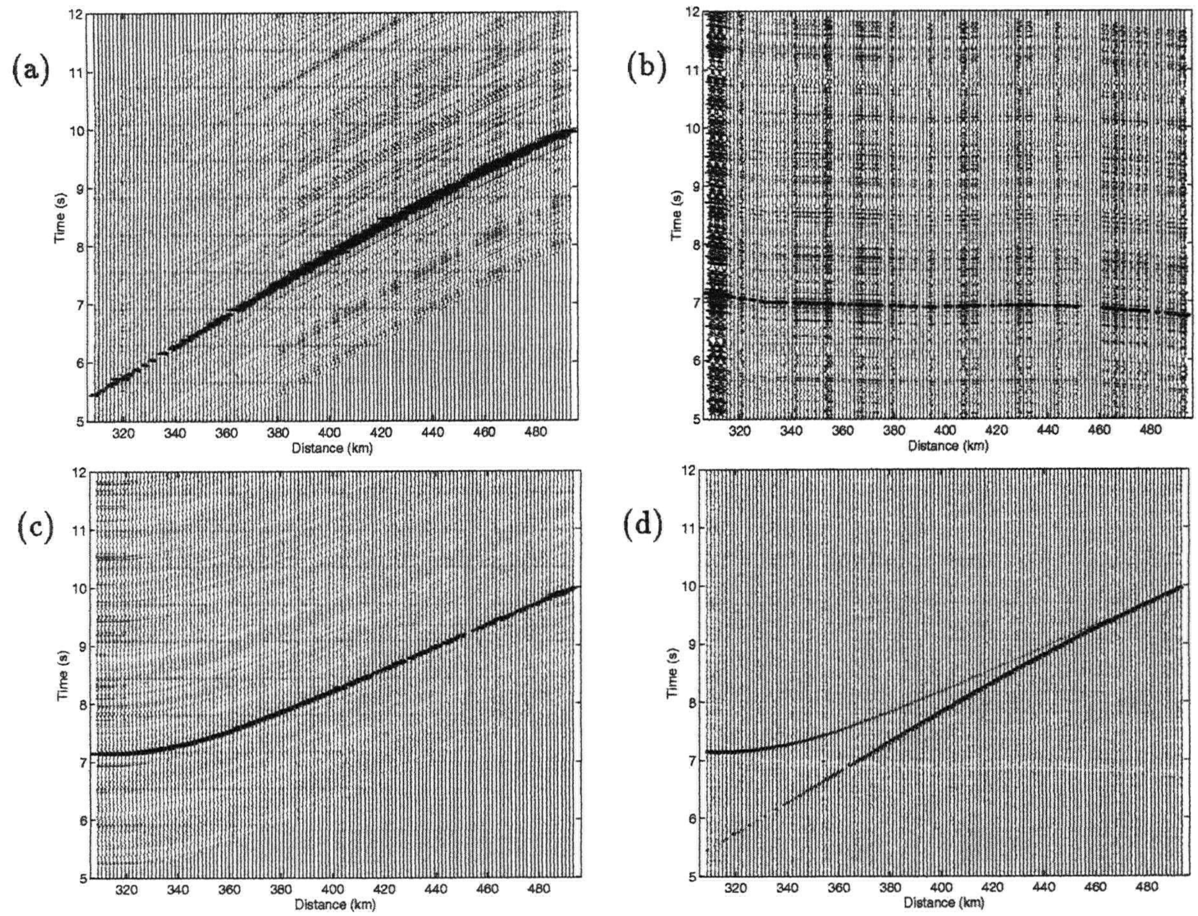

Figure 4.5: Eigenimages reshifted to original times a) Pg, b) Pn, c) PmP and d) sum of all three eigenimages

4.3 Eigenimaging of Real Data

Only the PmP phase will be imaged in this study since the Pg and Pn phases are relatively clear on the seismic sections. Eigenimaging is performed on all sections, but section 305 (Figure 4.6) is shown for illustrative purposes.

4.3.1 Eigenimage of Section 305

Figure 4.6 shows the PmP phase of shot 305 (located 190 km to the north of shot 301). Only the traces containing PmP arrivals not asymptotic to Pg are used for eigenimaging since this procedure cannot distinguish between parallel PmP and Pg phases. Figure 4.7 shows traces for 50-137 km offset from shot 305. The same basic steps as applied to the synthetic data were used, i.e., shifting to the horizontal, determining the singular values, eigenimaging and reshifting to the original positions.

Figure 4.8a contains the singular values for PmP. The first value produced an eigenimage with a faint signal and little noise. The second, had a better signal but with much more noise. All other values buried the signal within the noise. Thus, the final eigenimage was created by summing the images of the first two singular values and is shown in Figure 4.8b. The PmP phase is quite distinguishable in the eigenimage. The picks, shown as dots, coincide well with the signal. The final selection of PmP arrivals of Figure 4.3b were the result of picking interactively between the real data and the eigenimage until a good match occurred between the two. This was done with all sections.

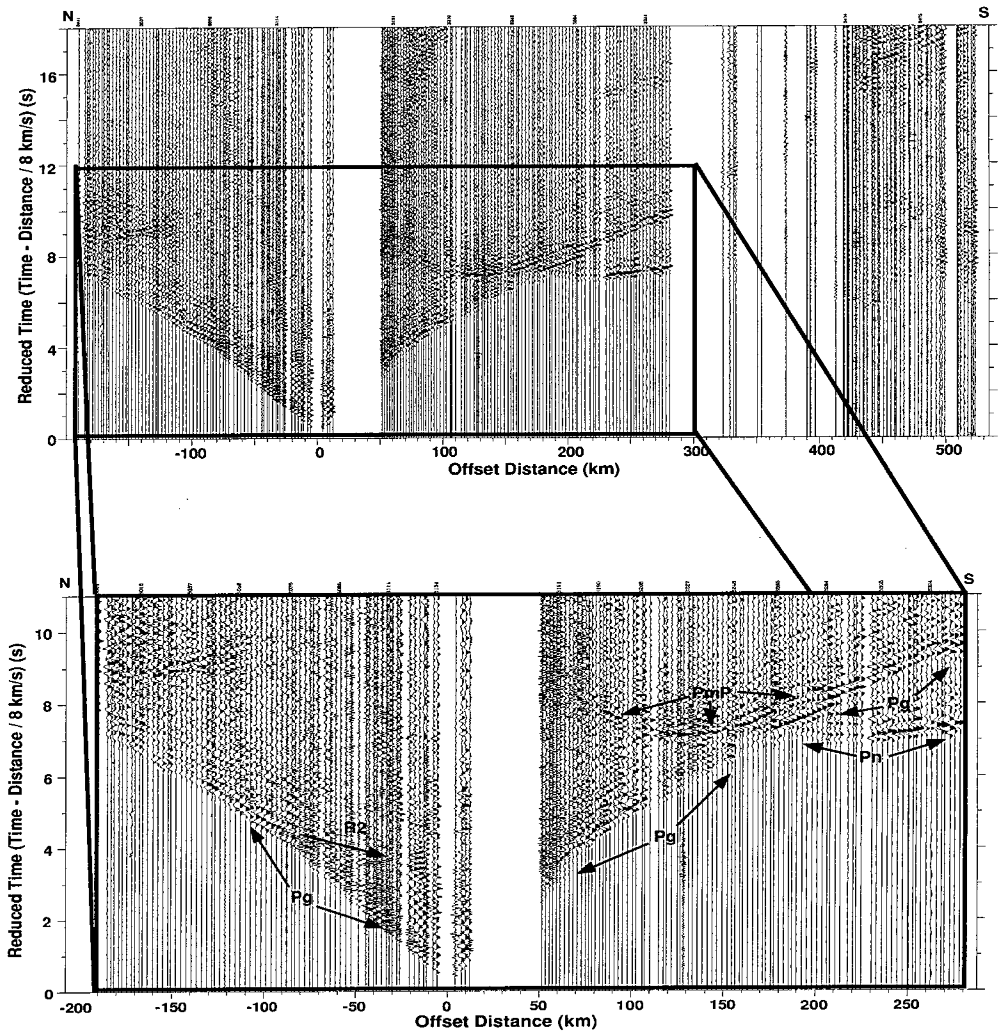

Figure 4.6: Section 305: Full seismic section. Pg, PmP and Pn phases are shown between the arrows. R2 is an intracrustal reflector.

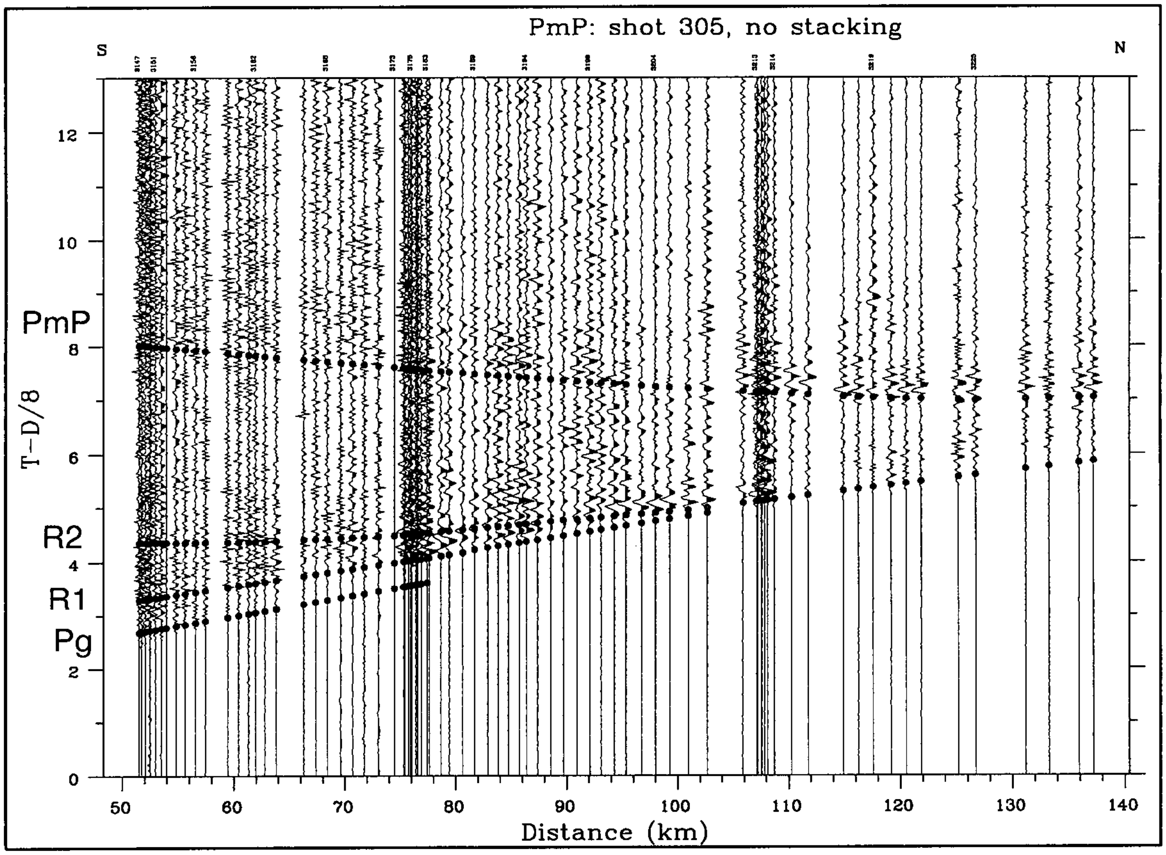

Figure 4.7: Section 305: Only the offsets that include PmP arrivals non-parallel to Pg are shown. Dots represent visually picked Pg, R1, R2 and PmP arrivals; R1, R2 are intracrustal reflections.

4.3.2 Test of Eigenimaging Method

To prove the eigenimage method actually images the coherent signal, the PmP arrivals were flattenend along a different possible set of travel times. The resulting singular values and eigenimage are shown in Figure 4.3c and d. When comparing both eigenimages, Figure 4.3b is clearer than Figure 4.3d, thus indicating the final selection of PmP arrivals was along the most horizontally coherent signals.

When performing eigenimaging as above, the entire section is dominated by the largest singular value. However, this is not appropriate because certain sections of the data have different horizontal coherency between the desired signal; thus using the same singular value for the entire section creates a false sense of coherency. To illustrate this point, the offset range from 50-140 km of shot 305 was divided into three 30 km sections. Each section was eigenimaged separately, using the same PmP arrivals as in Figure 4.3b. The singular values are shown in Figure 4.9 and the eigenimaging results in Figure 4.10. The coherency varies throughout the section and does not give the same results as eigenimaging the entire profile. This indicates that some of the coherency in Figure 4.3 is a false impression of what the horizontal coherency actually is. Thus, it is important to determine the singular values throughout the section as opposed to assigning only one general value.

4.3.3 Stacking

The aim of using the eigenimage analysis method is to obtain better and more reliable picks for the PmP phase. As seen above, there may be cases where the image is false. To overcome this, the following procedure was developed to provide the most reliable eigenimage. First, a subsection containing a specific number of traces was selected and eigenimaged. Second, the subsection was shifted by a predetermined number of traces and eigenimaged again. This continued until all traces of the section were eigenimaged. The overlapping images were then summed to produce the final image which encompasses all the singular values. To determine how many traces should be in a subsection and by how many to increment to produce the most accurate final eigenimage, groups of 8 incremented by 2, 16 by 4, 20 by 5 and 40 by 10 were used. The small group with small increments did not

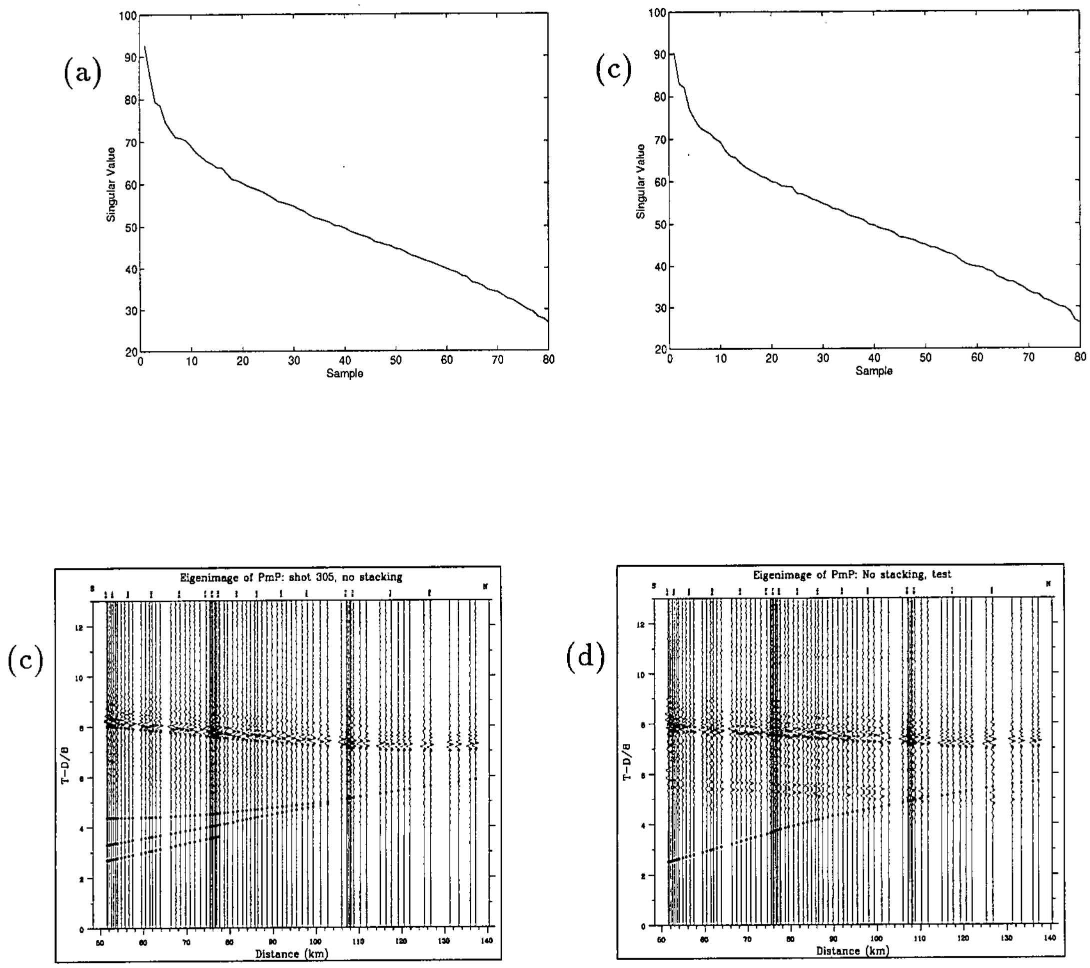

Figure 4.8: Eigenimage Shot 305: a) singular values for 'b'; b) eigenimage based on final picks; c) singular values for 'd'; d) eigenimage based on test picks.

produce eigenimages that were much better than the original data, most likely because there were not enough traces to determine coherency. The very large groups gave similar results as in section 4.3.2 due to domination of the larger singular values; thus, they are not sufficiently reliable. The best results were from groups of 20 incremented by 5. In this case, there are enough traces to determine vertical coherency but not enough to be influenced by other singular values.

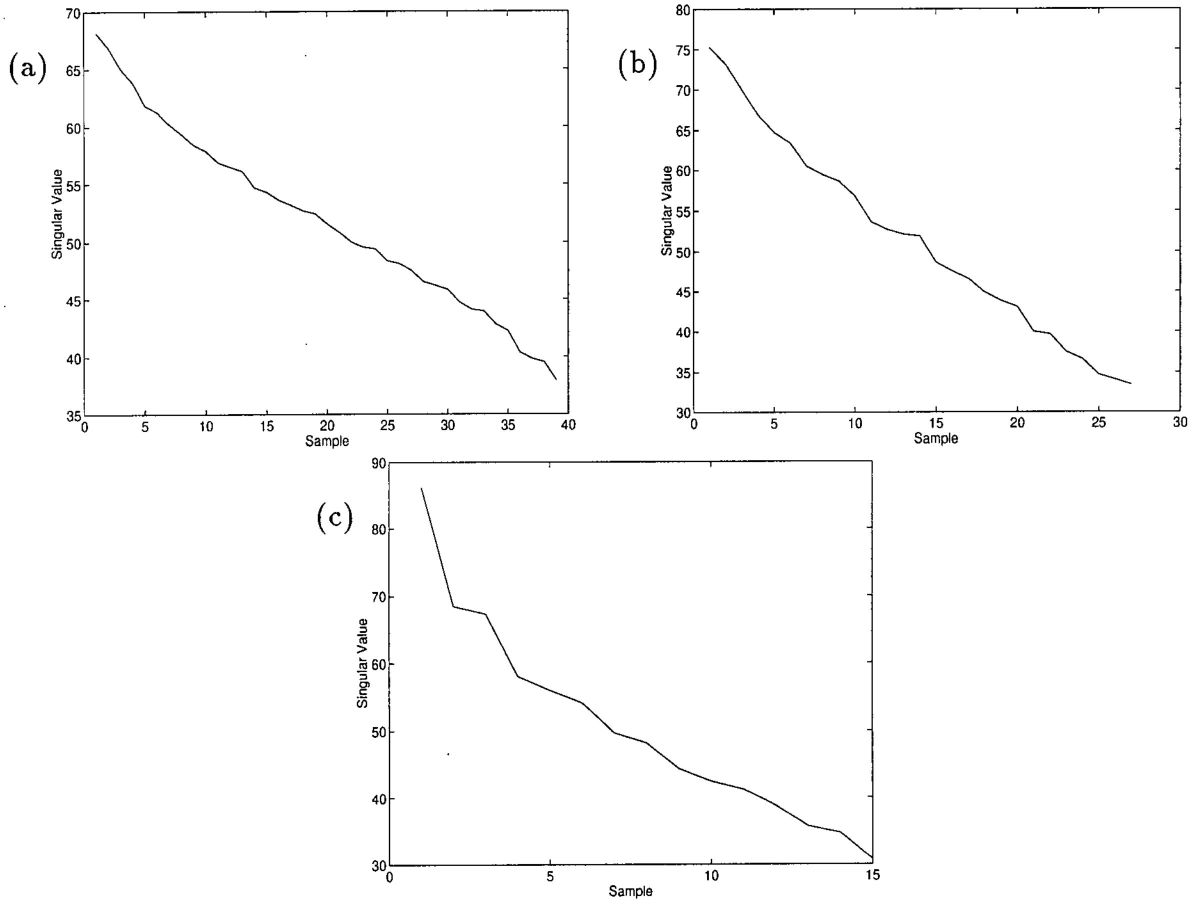

Figure 4.9: Singular values for Shot 305 for test 2: a) top: 50-80 km; b) 80-110 km; c) 110-140 km.

4.4 Eigenimage of All Profiles

Profiles of shots 301 to 311 (312 and 313 did not have sufficient PmP arrivals) of the THORE experiment have been eigenimaged for the PmP phase and are shown in Figures 4.11, 4.12 and 4.13. The procedures used were the same as described in section 4.3.3. These final images are the result of interactively updating PmP arrival picks within the eigenimages and the real data until a good match was found. These final picks can be used

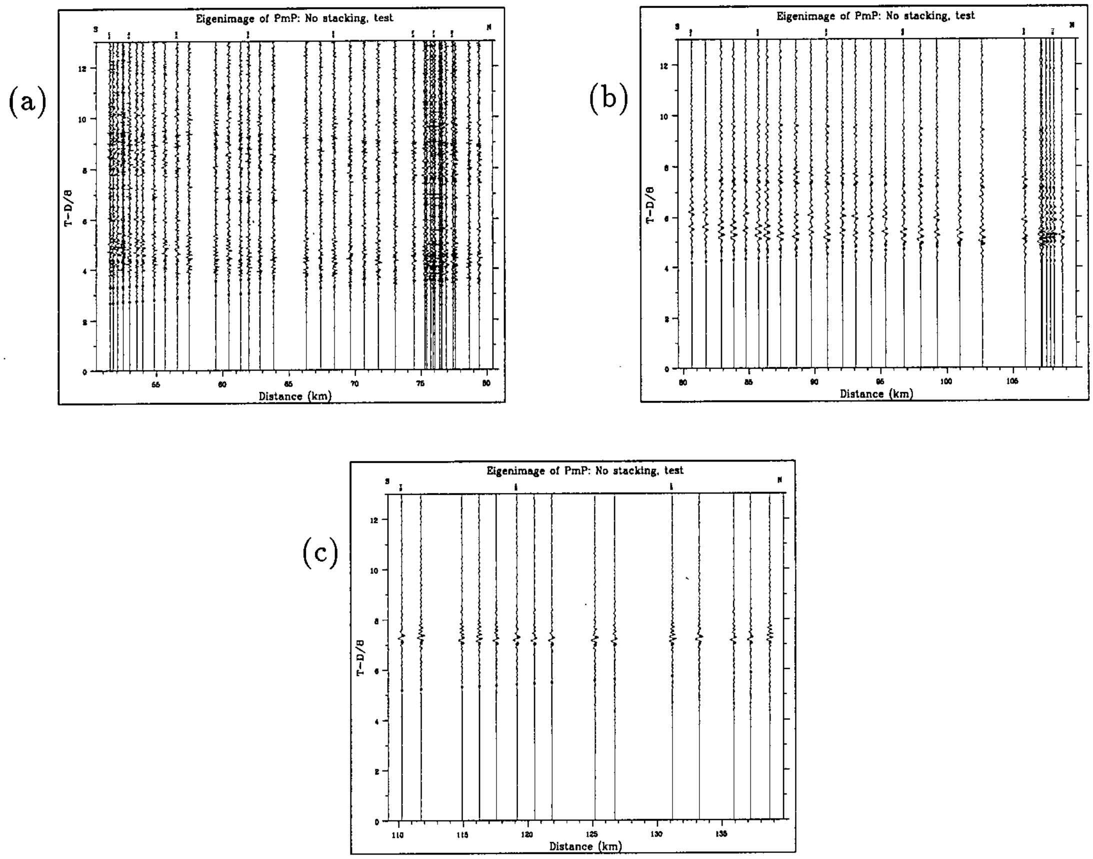

Figure 4.10: Eigenimage Shot 305 for test 2: a) 50-80 km; b) 80-110 km; c) 110-140 km.

to model the crustal velocity structure of line R3.

The PmP phases show up well for most cases. However, images of shots 301 and 302 are questionable, since the PmP phase is not strong resulting in a relatively poor retrieval of the signal. Note that the picks of most sections do not necessarily follow the highest amplitude, which is expected since the first of the PmP arrivals need to be picked, not necessarily the strongest ones.

4.5 Discussion of Eigenimage Method

. This new technique has proven useful in accurately picking difficult phases such as those produced by the reflections from the Moho (PmP). However, this method is not without faults. First, it is assumed that the traces are equidistant on the horizontal axis which is not the case for the real data. This may influence where the eigenimage calculates the vertical coherency of the signal. However, by stacking the images as in section 4.3.3, the inaccuracies caused by this problem are reduced. Second, this method must be implemented in conjunction with the phase picking of the real data. The images are only as accurate as the picks of a particular phase and thus it is important to use both real and eigenimages to update the picks.

Many modifications were done to the final crustal velocity model of this thesis as a direct result of this method. It is believed this procedure reduces picking error significantly for phases which are difficult to trace, and thus enhances the accuracy of the model interpreted from the data.

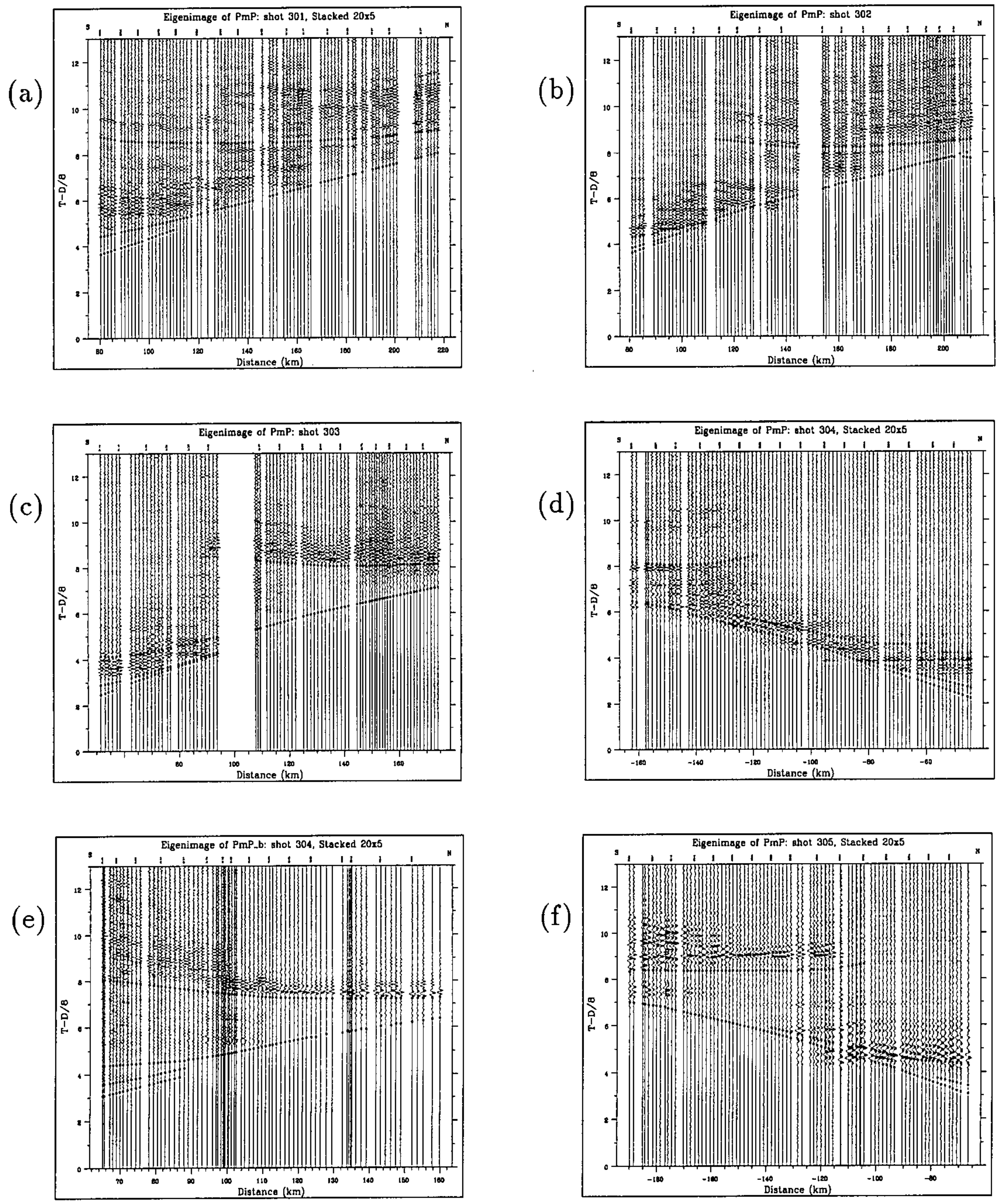

Figure 4.11: Stacked eigenimage: a) shot 301; b) shot 302; c) shot 303; d) shot 304a; e) shot 404b; f) shot 305a. Where split spreads are involved, data recorded in opposite directions were analysed separately; e.g., shot 304a and 304b.

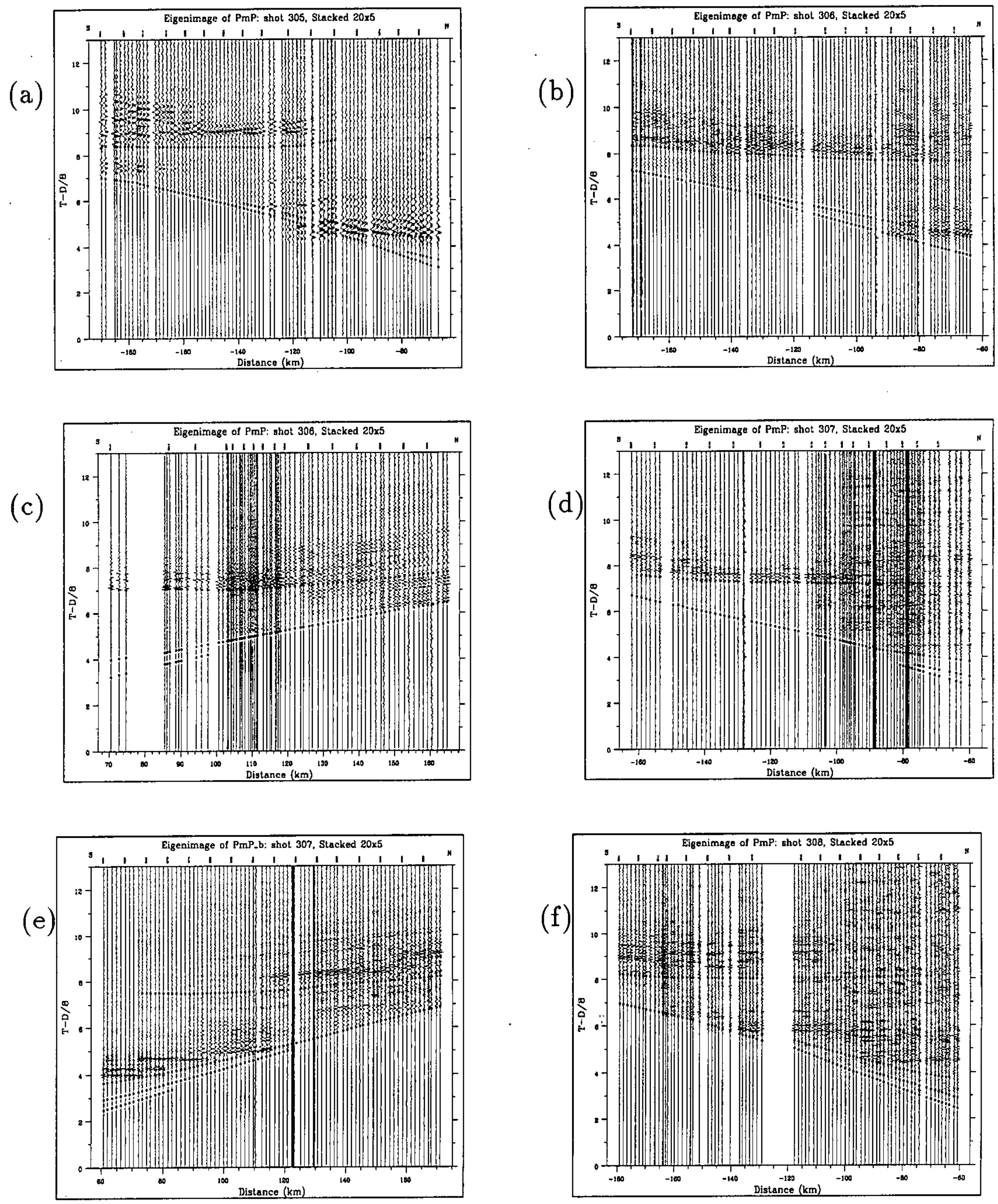

Figure 4.12: Stacked eigenimage: a) shot 305b; b) shot 306; c) shot 306b; d) shot 307a; e) shot 307b; f) shot 308.

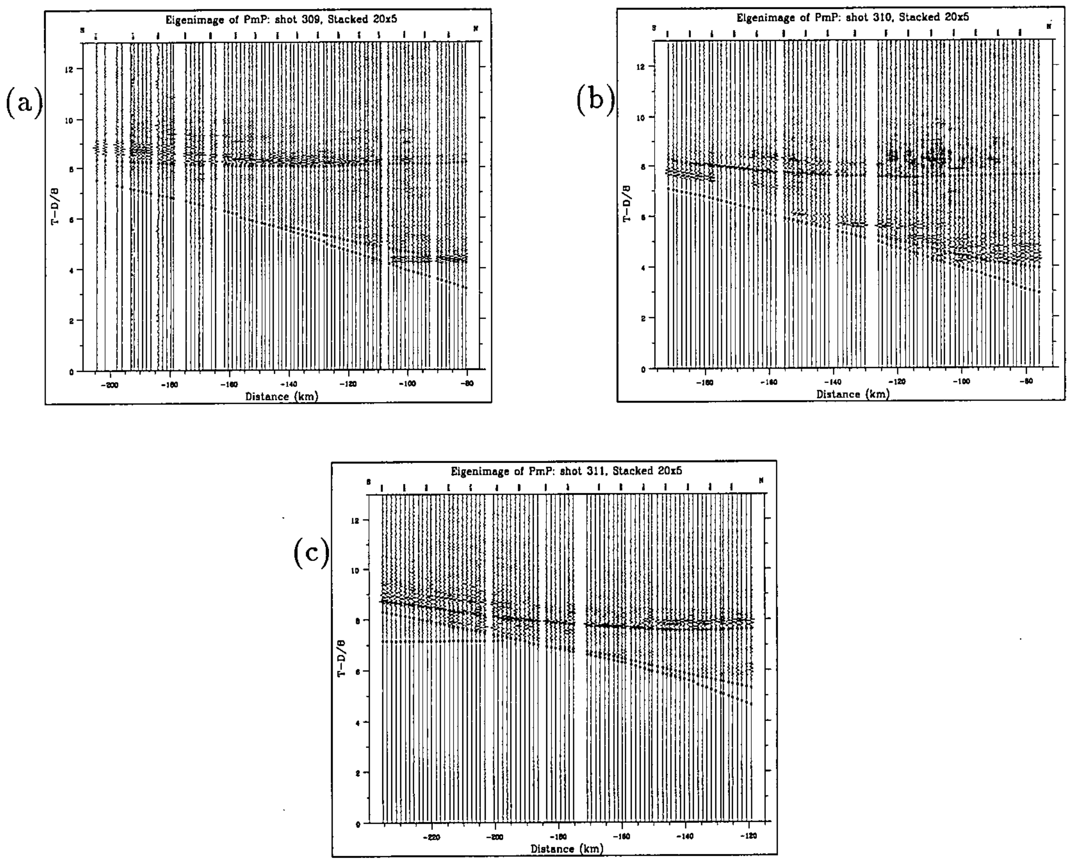

Figure 4.13: Stacked Eigenimage: a) shot 309; b) shot 310; c) shot 311.

5 Crustal Velocity Models

This chapter provides the details of model construction. It describes the phase picking and errors, the algorithms used for modelling, as well as the final model and its constraints.

5.1 Data Interpretation and Picking

True relative amplitude and trace normalised sections for all thirteen shots of line R3 are shown in Figures 5.4 - 5.29 (following the main text of this chapter). The insets of the trace normalised plots are used to demonstrate various features of the sections discussed in the following text or to enhance certain arrivals. The time is reduced by the distance divided by 8 km/s and the distances refer to the offset distances, i.e., the distance between shots and receivers.

There are five distinct phases amongst the thirteen sections: Pg, PmP, Pn, R1 and R2. The Pg and Pn arrivals represent phases of refracted waves through the crust and upper mantle respectively. The R1, R2 and PmP arrivals describe reflected waves off the upper- and mid-crustal boundaries (R1 and R2) and those reflecting off the Moho (PmP). These phases are labelled within the traced normalised sections of Figures 5.4 - 5.29. The phases were picked on paper and interactively on trace-normalised sections using the routine 'plotsec_pick'. The exact location of the arrivals were determined by visualising the trace-by-trace correlation of the phases using various scales of plots and amplitudes. The PmP phase was picked using the eigenimaging technique described in Chapter 4 and greatly reduced picking uncertainty. Picking errors were calculated using a subroutine within 'plotsec_pick' which estimates the signal-to-noise ratio and error of each pick. Tables **2** and **3** indicate where the various phases occur with respect to offset distance and the average picking error for each case.

Shot #	Pg(1)	Pg(2)	R1
301	/0-110 /(35)	/250-350 /(175)	/35-70 (175)
302	55-0/0-95 (75)/(35)	/210-360 /(175)	20-0/30-115 (200)/(175)
303	110-0/0-95 (50)/(35)	/195-355 /(175)	65-35/35-95 (200)/(175)
304	160-5/0-85 (50)/(75)	/160-290 /(175)	85-20/25-90 (175)/(200)
305	190-5/5-80 (50)/(35)	/170-280 /(175)	80-40/50-100 (175)/(150)
306	50-0/0-100 (50)/(100)	200-150/155-225 (150)/(150)	25-15/ (150)/
307	85-25/20-85 (100)/(25)	295-180/ (175)/(150)	95-25/45-120 (175)/(150)
308	200-20/20-250 (150)/(175)	/ /	90-20/ (175)/
309	210-30/20-195 (150)/(150)	250-210/ (175)/	65-30/20-55 (200)/(175)
310	220-0/0-170 (150)/(75)	300-220/ (175)/	/ /
311	200-0/0-125 (150)/(50)	395-200/ (150)/	/50-110 /(150)
312	190-0/0-70 (100)/(50)	345-190/ (175)/	/ /
313	245-0/ (100)/	345-245/ (175)/	60-0/ (150)/

Table 2: Offset distances where Pg(1), Pg(2) and R1 phases are found. Values to the left or right of the slash are south and north of the shot point respectively. Pg(1) and Pg(2) refract through upper-middle and lower crust respectively. Values in brackets are estimated average picking errors in milliseconds

Shot #	R2	Pn	PmP
301	/60-240 /(150)	/230-470 /(150)	/60-240 /(175)
302	/70-205 /(150)	/210-415 /(150)	/115-230 /(175)
303	110-60/40-200 (175/(175)	/185-365 /(150)	/110-200 /(175)
304	125-60/65-180 (200)/(150)	/180-310 /(100)	160-120/65-225 (200)/(175)
305	140-35/50-170 (175)/(175)	/170-270 /(100)	190-105/10-220 (175)/(175)
306	25-15/ (200)/(100)	/ /	195-65/170-270 (175)/(175)
307	180-25/50-170 (175)/(150)	295-180/ (150)/	205-90/70-170 (175)/(175)
308	145-65/ (175)/	300-200/ (200)/	180-70/105-225 (200)/(175)
309	140-60/65-170 (175)/(150)	300-210/ (200)/	230-70/115-195 (175)/(175)
310	125-75/25-135 (175)/(150)	300-220/ (150)/	240-75/75-170 (175)/(175)
311	180-120/ (150)/	395-200/ (175)/	250-120/ (175)/
312	135-40/ (175)/	345-190/ (150)/	275-175/ (200)/
313	110-50/ (175)/	375-245/ (175)/	205-0/ (175)/

Table 3: Offset distances where R2, Pn and PmP phases are found. Values to the left or right of the slash are south and north of the shot point respectively. Values in brackets are estimated average picking errors in milliseconds.

5.1.1 Observations of Pg (1), R1 and R2 Phases

For shots 301-305, the amplitude of the Pg (1) phase (rays through the upper and mid-crust) is consistent up to 50 km offset. South of the shot points, the Pg arrivals are amplified by the energy of the R1 (50-100 km) and R2 (>100 km offset) reflections, possibly by constructive interference. The R1 and R2 amplitudes are relatively small compared to those in the other sections and this is caused by the smaller velocity contrast between the upper, mid- and lower crust ($\approx$ 0.1 km/sec). To the north of the shot points, the R2 energy is sufficient to 'mask' the Pg arrivals beyond 100 km offset, since the velocity contrast between the mid- and lower crust is relatively large.

The Pg (1) amplitudes are similar within 50 km offset of shot points 306-313 indicating small lateral velocity gradient. Beyond 50 km, the Pg energy is masked by the stronger R1 and R2 reflections. The R1 energy decreases within the northern sections indicating that the velocity contrast between the upper and mid-crust diminishes. However, the R2 reflections are stronger because the difference between the velocities of the mid- and lower crust is larger.

The average pick errors for the Pg (1) phase increases north of shot 307 and can be attributed to the increase in noise in the data to the north, which may be due to the change in instrument type (REFTEK) and/or a change in surface geology. They are small compared to other phases because they are primarily picked as first arrivals. The errors for the R1 and R2 phases are relatively constant throughout the sections.

5.1.2 Observations of Pg(2), PmP and Pn phases

The Pg(2) arrivals, representing the refracted waves through the lower crust, are relatively strong up to 350 km offset indicating a large velocity gradient especially to the south of Shot 307. The picking error was significant since it was difficult to distinguish between signal and noise in some cases.

The Pn phase is apparent in all sections except for shot 306, due to insufficient offset distances, and shots 308 and 309, where there is no clear observation of the phase. It is strong for energy travelling to the north from shots in the south, but appears weaker for energy travelling south from shots in the north. For shots 301 and 302, the traveltimes decrease at $\approx$ 300 km offset to $\approx$ 6.2 seconds. Shots 308-311 also show a decrease of traveltime to $\approx$ 6.2 seconds between 200-350 km offset. This offers a strong indication of a high velocity zone in the area. There is no significant change in Pn traveltime for shots 303, 304, 305 and 307 due to a more constant velocity in the area the Pn rays are passing through.

The arrivals (PmP) from the reflected waves off the crust-upper mantle boundary, i.e. Moho, are strong on most sections. This is a result of the large velocity contrast at the Moho. The arrivals are particularly strong and clear in sections 303, 304 and 305 and occur in the same vicinity on the R3 line as the large change in Pn velocities mentioned above.

The average errors of picking for these phases are relatively constant for the entire R3 line.

5.2 Modelling Algorithms and Techniques

In order to construct a velocity model, the method of seismic traveltime inversion for simultaneous determination of 2-D velocity and interface structure by Zelt and Smith (1992) was used. A very general description of the algorithm and its parameters will be discussed briefly.

The method of traveltime inversion stems from the forward modelling routine of Zelt and Ellis (1988). The advantages of inversion over forward modelling include less trial-and-error modelling, estimates of model parameter resolution uncertainty and non-uniqueness and data fits according to a specific norm. This results in a more rapid and accurate interpretation.

The Zelt and Smith (1992) seismic traveltime inversion program is iterative and based on a parameterization which defines the velocity and boundary nodes to be modified during the inversion. The nodes are situated at the user's discretion at the top and bottom of each layer. The P-wave velocity field within each layer between the nodes is determined through linear interpolation. The boundary nodes are connected horizontally (also using linear interpolation) to define the extent and depth of each layer. For the modelling in this thesis, the boundary and velocity nodes were located at the shot point locations because this assignment gave the best trade-off between traveltime fit and parameter resolution for models in which the rays were traced to all receivers.

The inversion utilises a damped least-squares technique to determine new values for the velocity and boundary nodes which would provide a better fit between observed and calculated travel times. Weighted trade-off values of 0.1 and 0.001 were used for the velocity and boundary nodes, respectively, for the inversion. These values were chosen through trial and error as a change in velocity affected the data fit more than a change in boundary depth. The relative values of the weighted trade-off determine the size of velocity and boundary adjustments during inversion.

Another important feature of the Zelt and Smith (1992) inversion program is the way in which it quantifies the 'goodness' of the inversion. It does this through the calculation of RMS traveltime residuals for each input pick made and a normalised χ^2 value for each inverted model. The RMS traveltime residuals are the difference between the RMS traveltimes (the 'best-fit' traveltime calculated during the damped least-square inversion) and the observed traveltime picked by the seismologist. The smaller the RMS value, the better the fit. However, this only provides a measure of the error in a single calculated source-receiver traveltime. To provide an estimate of the misfit of the inversion as a whole, the χ^2 technique is used. The χ^2 value, which is an estimate of the misfit between the observed and calculated arrival times, is the sum of the squares of all the differences between the calculated and observed traveltimes divided by the standard deviation of the calculated traveltime. If χ^2 is smaller than the number of arrivals picked, then the calculated data fit the observed data well. If it is greater, the fit is not acceptable.

5.3 Starting Model

No refraction studies existed in this particular area and the reflection data have not been fully interpreted. Estimates were thus required for velocities and layer boundaries. The results of refraction line D of Morel-à-l'Huissier et al. (1987) (see Section **1.3.1**) provide initial values of velocities and depth for the southern section of R3. Using standard reflection enhancement techniques (see Section **6.1.1**), Nemeth et al. (1996) were able to define the Moho topography which is used as the initial starting model for the inversion.

To obtain a more acceptable starting model, two model end members were constructed. One kept the depth boundaries constant, while varying the velocities; the other held the velocity constant and varied the boundaries. Ray-tracing through both models was performed by layer stripping until an agreeable fit between the calculated and observed arrivals was obtained.

Layer-stripping consists of varying the velocities and depth boundaries of a particular layer by keeping the layers above fixed. Once the layer provides a reasonable fit, it is kept fixed and the layer below is adjusted. This continues until all layers are modelled.

Since there were not many estimates of the velocity and boundaries for the starting model, forward modelling was used until the fits were good enough to provide a more stable inversion. The fits were considered acceptable when most calculated arrivals were within the error range of the observed points. Several inversions were done to 'fine-tune' the end-members; however, the fits were not acceptable for a final model.

Once acceptable models were obtained (Fig. 5.1) for both end-members, the 'varying' boundaries and velocities were combined to create the starting model.

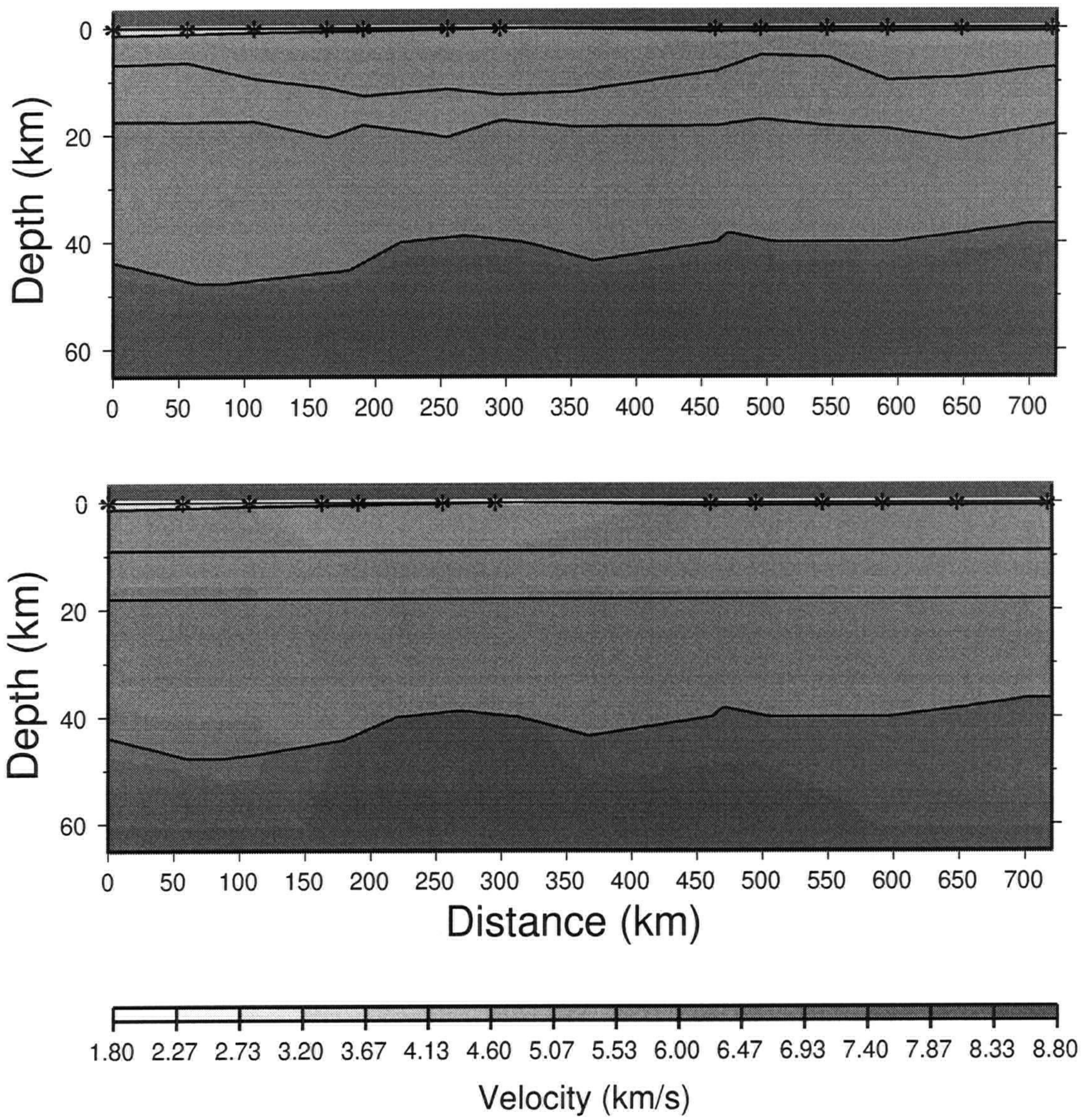

Figure 5.1: End member velocity models. The top diagram represents the constant velocity varying boundary. The bottom, constant boundary with varying velocity. Stars indicate shot point locations.

5.4 Final Model

The final model was created by inverting each layer of the starting model to obtain good agreement between the observed and calculated phase arrivals as well as acceptable χ^2 and RMS values. First, inversion was done by layer stripping for each shot location individually until calculated travel-times were within the error of the observed times and χ^2 and RMS values were relatively small. Second, the model was inverted, by layer stripping, using several shots consecutively. Finally, layer stripping was used with all the shots consecutively and the final results form the final model shown in Figure 5.2. There is good ray coverage for the entire R3 line as shown in Figure 5.3. The observed and calculated data fit well as depicted in Figures 5.30 - 5.42 (pages 82 - 94). Note that in these figures, distances are model distances with zero to the south (as used in Figure 5.2). Tables **4** and **5** contain the χ^2 and RMS values for each phase of every shot point.

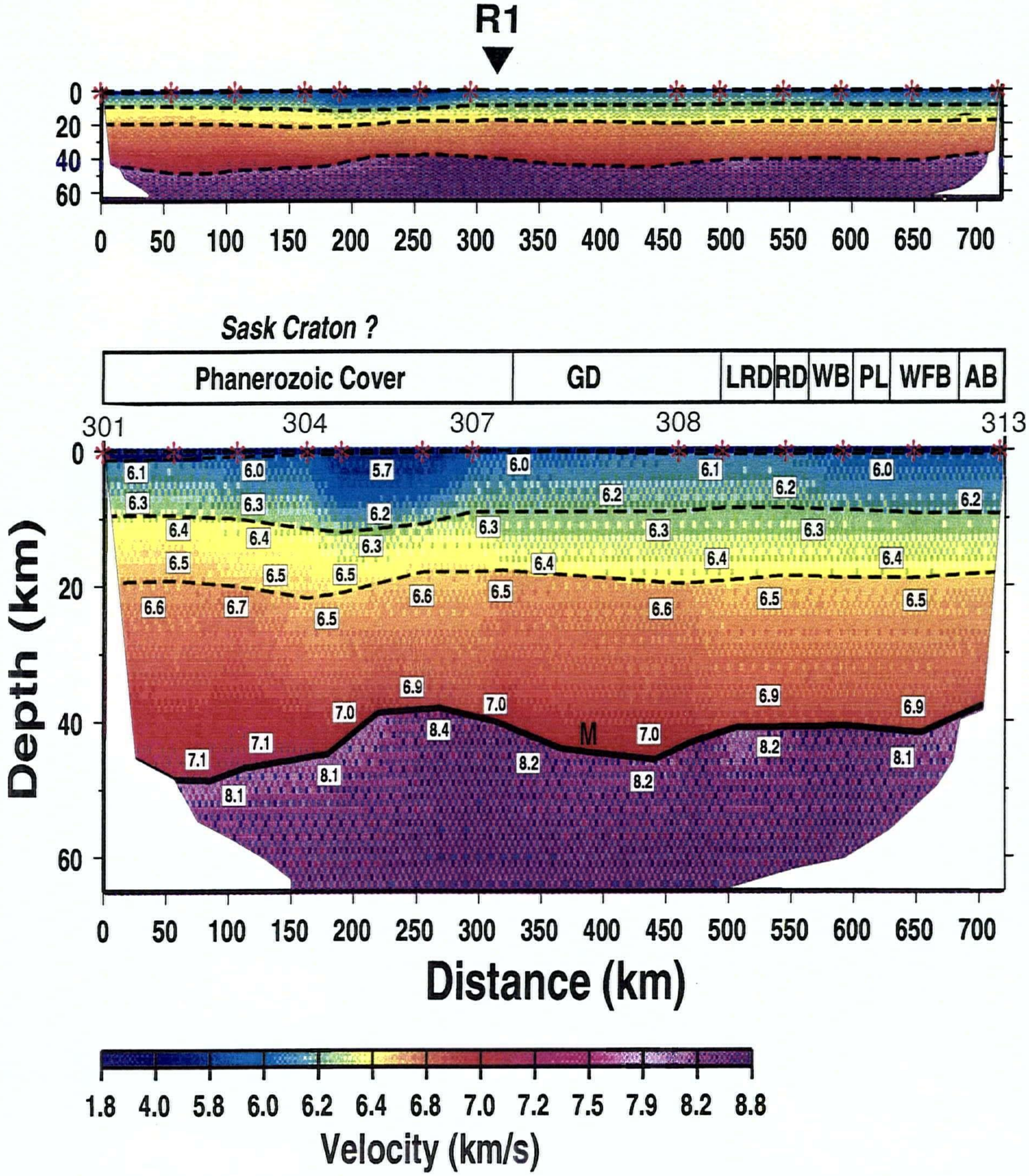

Figure 5.2: Final velocity model. The top diagram represents the 1:1 model and the bottom is vertically exaggerated by a factor of 4. The velocities, shown in white boxes, are in km/s. The solid line delineates the Moho (M). Stars indicate shot point locations. GD, Glennie Domain; LRD, LaRonge Domain; RD, Rottenstone Domain; WB, Wathaman Batholith; PL, Peter Lake Domain; WFB, Wollaston Fold Belt and AB, Athabasca Basin

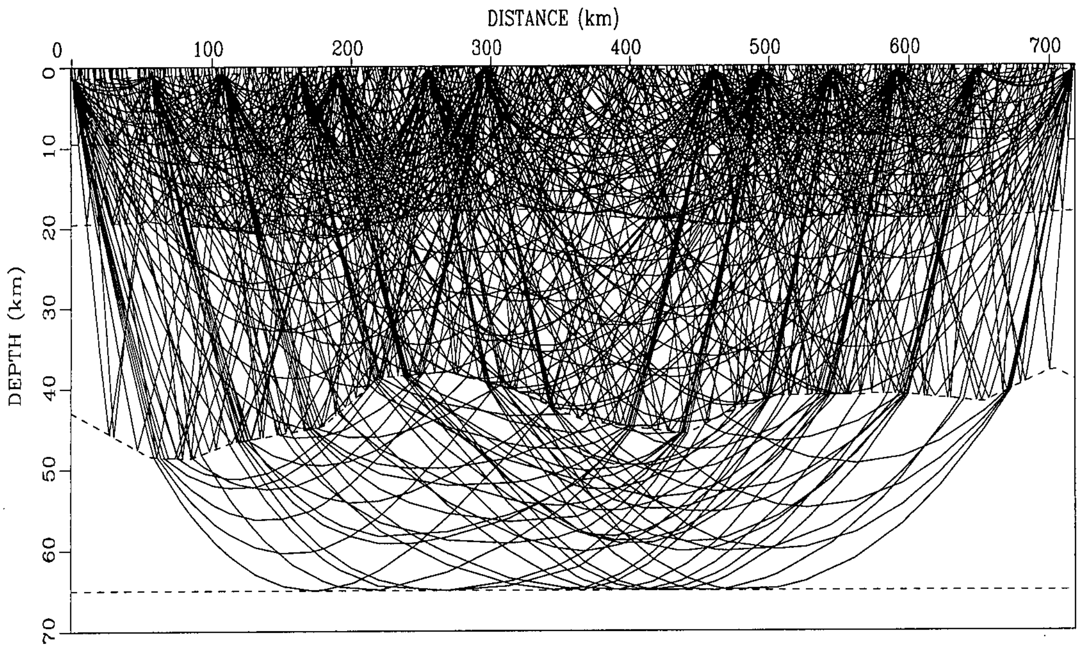

Figure 5.3: Ray coverage of final velocity model using all shot points. Only 5 rays for each phase are illustrated to avoid clutter on the figure.

Shot #	# rays	RMS	χ^2
301	450	0.119	0.792
302	518	0.112	0.918
303	594	0.120	1.615
304	689	0.148	2.161
305	736	0.132	1.449
306	553	0.17	2.405
307	755	0.178	1.612
308	529	0.176	2.322
309	577	0.108	1.142
310	569	0.128	0.843
311	535	0.105	2.379
312	399	0.153	2.157
313	365	0.117	0.553
all	7269	0.140	1.619

Table 4: The χ^2 and RMS values for each shot point.

Phase	# rays	RMS	χ^2
Pg	2605	0.135	2.735
R1	634	0.135	0.972
R2	1348	0.156	1.286
PmP	1618	0.140	0.621
Pn	1088	0.134	1.360

Table 5: The χ^2 and RMS values for each phase.

5.4.1 True Amplitudes

To assure the final model gives as much as possible an adequate representation of the 'real' Earth, a comparison between the true amplitudes from the observed data and the synthetic amplitudes generated using the final model was done. The following describes how the amplitudes for each were obtained and compared.

The true amplitude data are shown in Figures 5.4 - 5.29. The routine 'plotsec_amppk' determines the amplitude of each phase by calculating the average amplitude over a 0.25 s each pick. These values were plotted versus offset distance from both north and south recording directions as shown in Figures 5.30c - 5.42c. Only a general trend of the amplitudes is needed for comparison. Thus the data were smoothed by calculating the mid-point between two values and iterating the result forty times. This method deleted some of the data at the nearer offsets, but for comparison purposes this is acceptable.

5.4.2 Synthetic Amplitudes

The synthetic seismograms were obtained using the algorithm by Zelt and Ellis (1988) which has the same parameterization as the Zelt and Smith (1992) algorithm. Thus, the same boundary and velocity nodes of the final model were used to generate the synthetic plots shown in Figures 5.30b - 5.42b . It calculates the amplitudes using zero-order asymtotic ray theory (Červený et al., 1977; see Zelt and Ellis, 1988, for details).

The amplitudes of the synthetic seismograms were calculated using a quality factor (Q) of 800, which represents 2π/fraction of energy lost per cycle and is assumed to account for attenuation and reduction of energy caused by characteristics of the transmitting medium. This Q value is the average attenuation factor for the area of study based on a scattering model to explain the coda waves of local and regional earthquakes (Singh and Herrmann, 1983).

5.4.3 Comparison between True and Synthetic Amplitudes

The aim of this comparison is not to compare absolute values of the synthetic and relative true amplitudes, but to determine if the general trends in amplitudes for each phase are comparable. Previous crustal velocity modelling usually only made visual or qualitative comparisons between the synthetic and true amplitude sections; e.g., comparing figures such as Fig. 5.4 and 5.30b for shot 301, and similarly for other shots. Comparing the amplitudes as described in this thesis provides a more qualitative comparison since each individual phase is studied for each section and actual amplitude trends are clearly seen.

Generally, the amplitude trends for each phase coincide well for the synthetic and relative true amplitude phases (Fig. 5.30 - 5.42 b and c). The major discrepancies occur with the Pg(1) phase for shots 301-307 and 309, where there is a relatively large amplitude in the synthetic section over a limited range of offsets, and small amplitudes at similar offsets for the true amplitude phases. However, the trends are similar when the Pg, R2 and/or R1 amplitudes of the observed data are superimposed. This is because it is sometimes difficult to differentiate between the phases when picking on the real data, whereas all the phases appear independently on the synthetic sections. All other phases (Pn, PmP, R1 and R2) coincide well with each other.

The comparisons are not perfect, but they are very good considering the complexity of selecting the correct phases on the observed data as well as the amplitude computation errors in the synthetic seismograms as a result of using an imperfect theory to describe the Earth.

5.4.4 Details of Final Model

The final model is shown in Figure 5.2. The most southern section has a cover of up to 1400 m of Phanerozoic sediments (average $\approx$ 3.4 km/s) and thins northward until basement is observed at the surface near 315 km model distance. A 600 m weathered layer was included on the northern half of line R3 to accommodate the lower basement velocities (4.0-4.5 km/s) at the very near offsets of the six most northern shots. This is attributed to weathering and fracturing of the rocks near the surface. The thickness and velocity of this layer was found through forward modelling.

The upper crust has an average depth of 9.5 km, but dips to a maximum of 12 km between 150-300 km. The lowest velocities of 5.65-6.25 km/s occur in this region. The velocities to the south of this feature range from 6.1-6.3 km/s and 6.1-6.25 km/s to the north.

The mid-crust has velocities from 6.35-6.55 km/s to the south which decrease to the north to 6.25-6.4 km/s. Average depth is 19 km, but it also has a synclinal structure which follows that of the upper layer. In this case the maximum depth is 22 km. However, the mid-crustal layer retains a relatively consistent thickness.

The lower crust has relatively high velocities of 6.6-7.1 km/s in the southern section of line R3, but as with the layers above, the velocity decreases northwards (6.5-6.9 km/s). The Moho topography varies from a minimum of $\approx$ 38 km to a maximum of $\approx$ 48 km depth which is significant. The thickest crust lies from $\approx$ 50-175 km at the southern end of the line but thins rapidly to 38 km at 250 km. It reaches $\approx$ 45 km depth at 400 km and then thins to 40 km in the most northern section of the line. The Moho topography is very well constrained by the PmP reflections from the crust-mantle boundary. Upper mantle velocities range from 8.1 km/s at the southern end of the line to 8.2 km/s to the north. However, a high velocity zone ($\approx$ 8.4 km/s) lies between 200-350 km where the crust is at its thinnest. The Moho topography and upper mantle velocities will be discussed further in the next chapter.

5.4.5 Resolution of Final Model

To determine the spatial resolution and absolute parameter uncertainty of the model, two tests were done on velocity and boundary nodes of the final model. Both tests are described in detail in Zelt and Smith (1992).

An estimate of spatial resolution can be found by the following method. First, a single parameter (node) is selected and perturbed within its uncertainty. Then, rays are traced through the model with the perturbed node. The travel-times for this case are saved and then the parameter is reset to its original value. The rays are run through the original model but with the travel-times saved above as the observed data. The selected parameter is held fixed while the surrounding nodes are inverted. The spatial resolution about the selected parameter will be indicated by the amount that the values of the adjacent parameters differ from the corresponding values of the final model. In this case, the depth and velocity nodes were varied from 2-4 km and 0.2-0.4 km/s to obtain slightly different ray paths from the original. The spatial resolution estimates are shown in Table **6**.

To obtain an estimate of a parameter's absolute uncertainty, a value is perturbed and held fixed while the surrounding nodes are inverted. Then, the perturbation is increased until the rays are not traced to all observations or the F test comparing the χ^2 values of the two final models shows the values are significantly different. Results are shown in Table **6**.

Table 6 provides uncertainty values based upon objective tests using the traveltime inversion routines of Zelt and Smith (1992). What is not included in the results of such calculations is the contribution that forward modeling, with synthetic seismogram comparison of observed amplitude variations, makes to the refinement of the velocity model. This is an added on constraint, but by its nature cannot be quantified. Hence the numbers shown in Table 6 are considered maximum ones; in reality both the lateral resolution and absolute uncertainty should be less than the table indicates.

Nodes	$\approx$ lateral res. (km)	$\approx$ absolute uncertainty
Velocities at top of upper crust	30-60	0.15 km/s
Depth nodes at top of upper crust	60	2 km
Velocities at top of middle crust	50	0.2-0.15 km/s
Depth nodes at top of middle crust	60	3 km
Velocities at top of lower crust	50-70	0.2-0.15 km/s
Depth nodes at top of lower crust	60	3.5 km
Velocities at upper mantle	70	0.3 km/s

Table 6: Estimated lateral resolution of the final velocity model about the given nodes, and absolute uncertainty of velocity and depth nodes based on traveltime analysis.

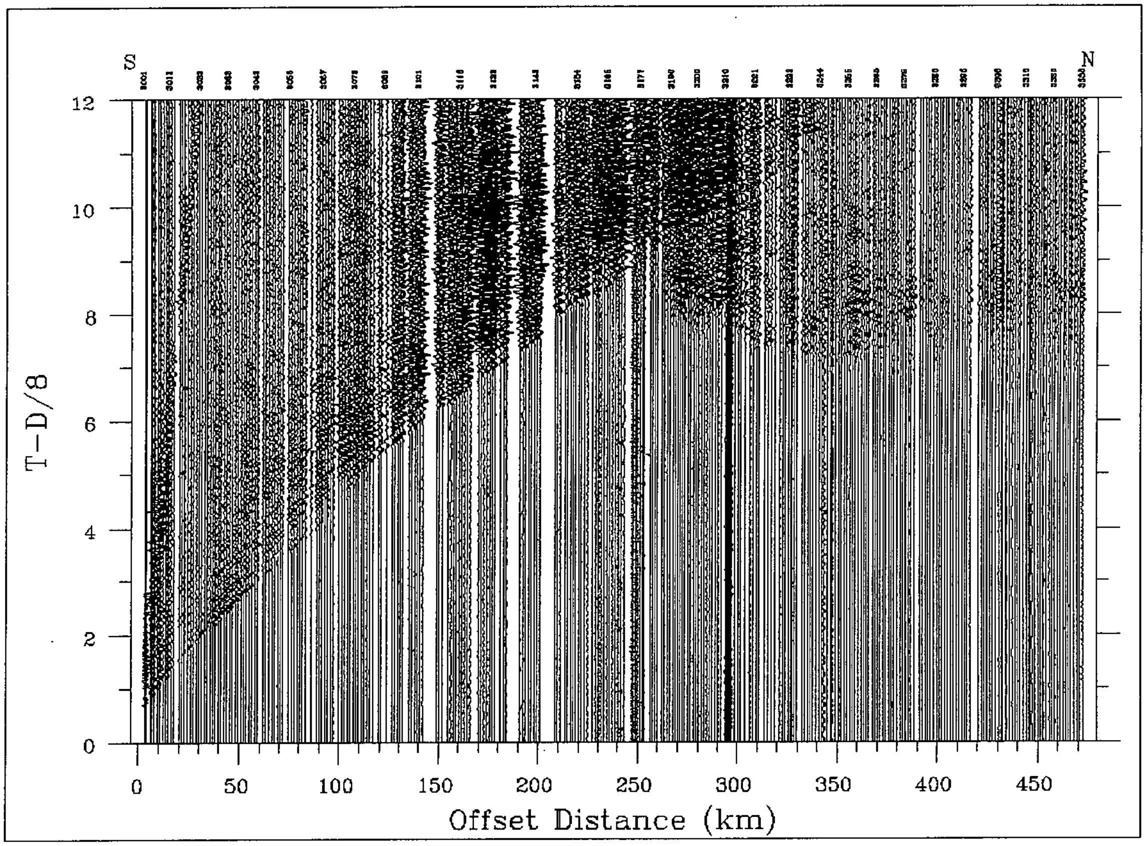

Figure 5.4: Observed true amplitude section for shot 301. The reducing velocity is 8 km/s and the distance is the offset distance from the shot point.

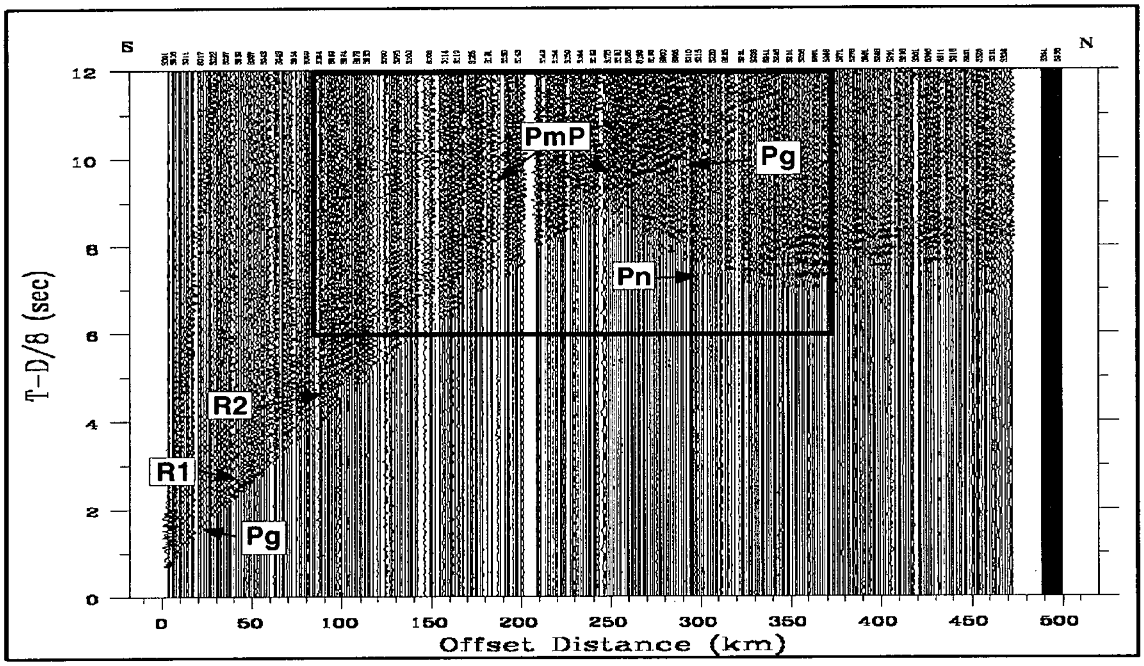

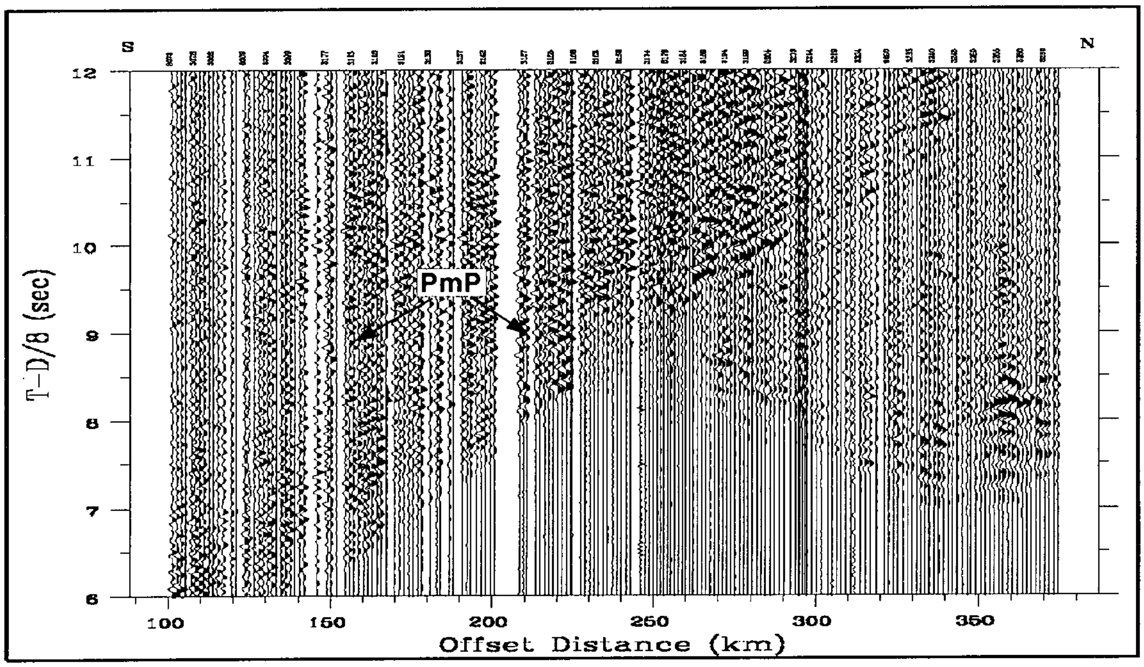

Figure 5.5: Observed trace normalised section for shot 301. a) The entire section. The box defines the inset position. b) Inset enhancing the PmP, Pg and Pn phases. The reducing velocity is 8 km/s and the distance is the offset distance from the shot point.

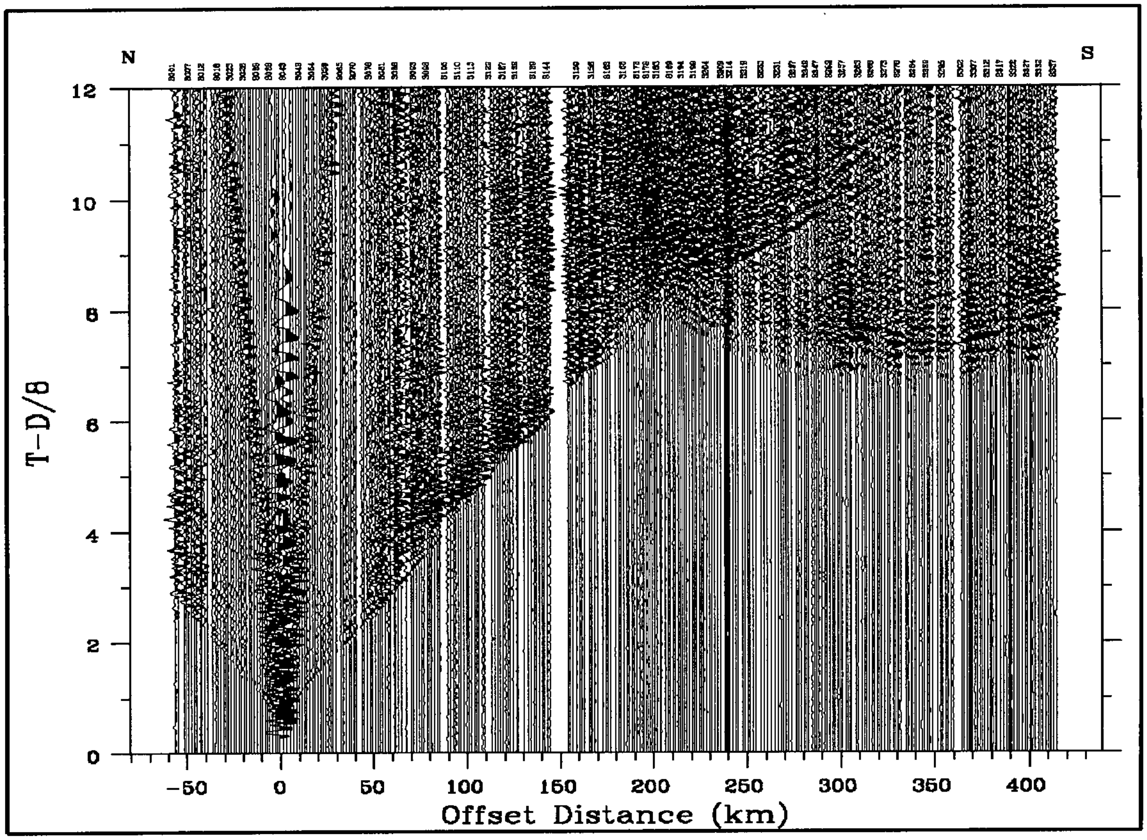

Figure 5.6: Observed true amplitude section for shot 302. The reducing velocity is 8 km/s and the distance is the offset distance from the shot point.

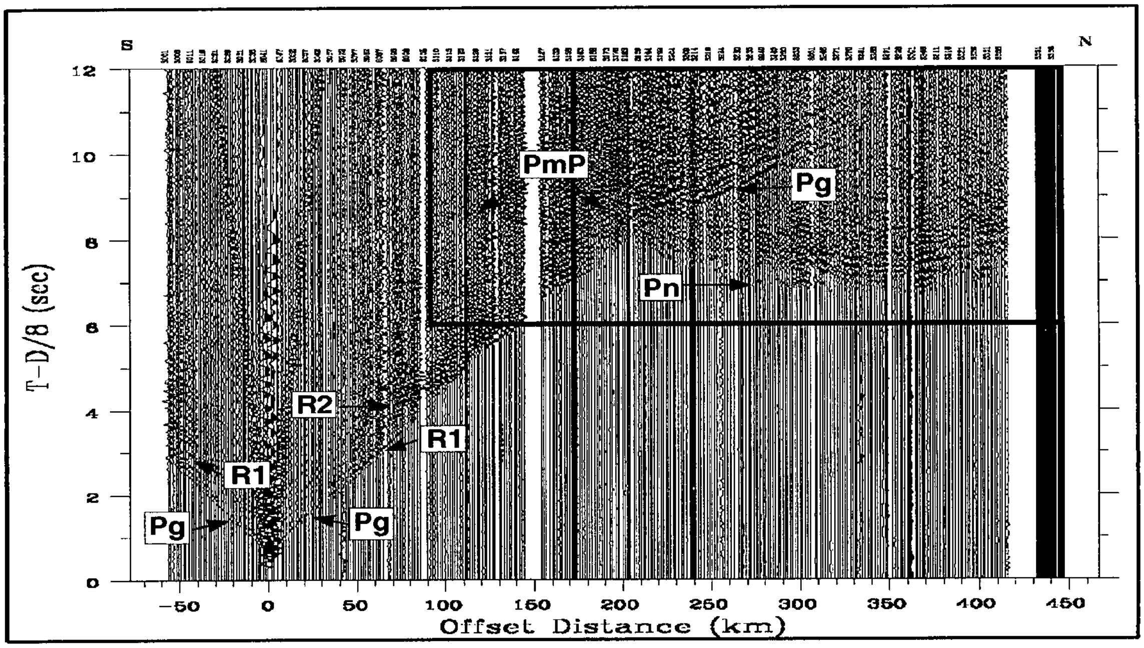

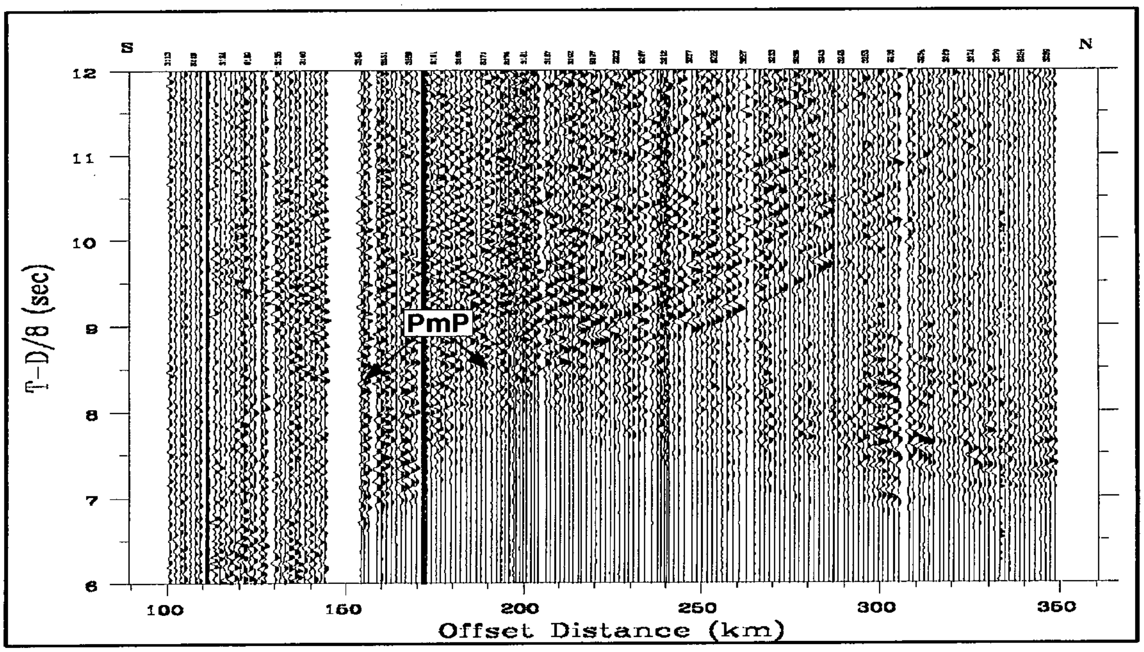

Figure 5.7: Observed trace normalised section for shot 302. a) The entire section. The box defines the inset position. b) Inset enhancing the PmP, Pg and Pn phases. The reducing velocity is 8 km/s and the distance is the offset distance from the shot point.

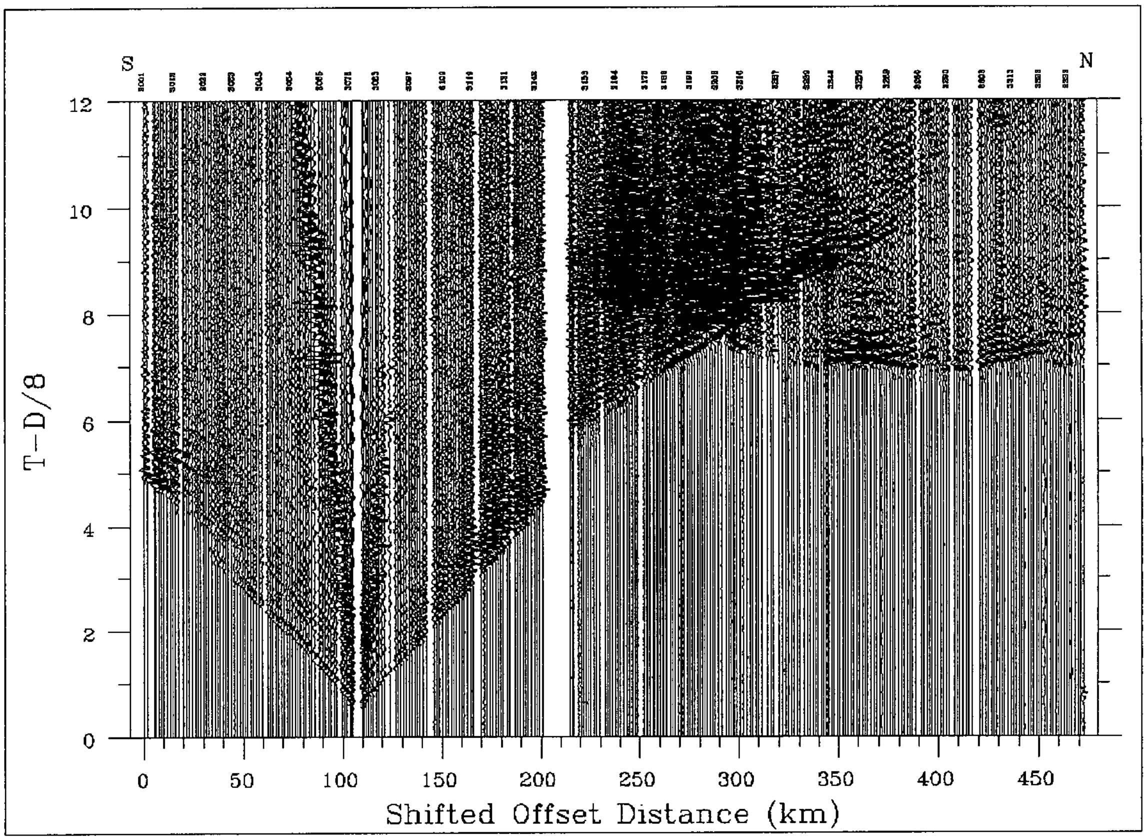

Figure 5.8: Observed true amplitude section for shot 303. The reducing velocity is 8 km/s and the distance is the offset distance from the shot point.

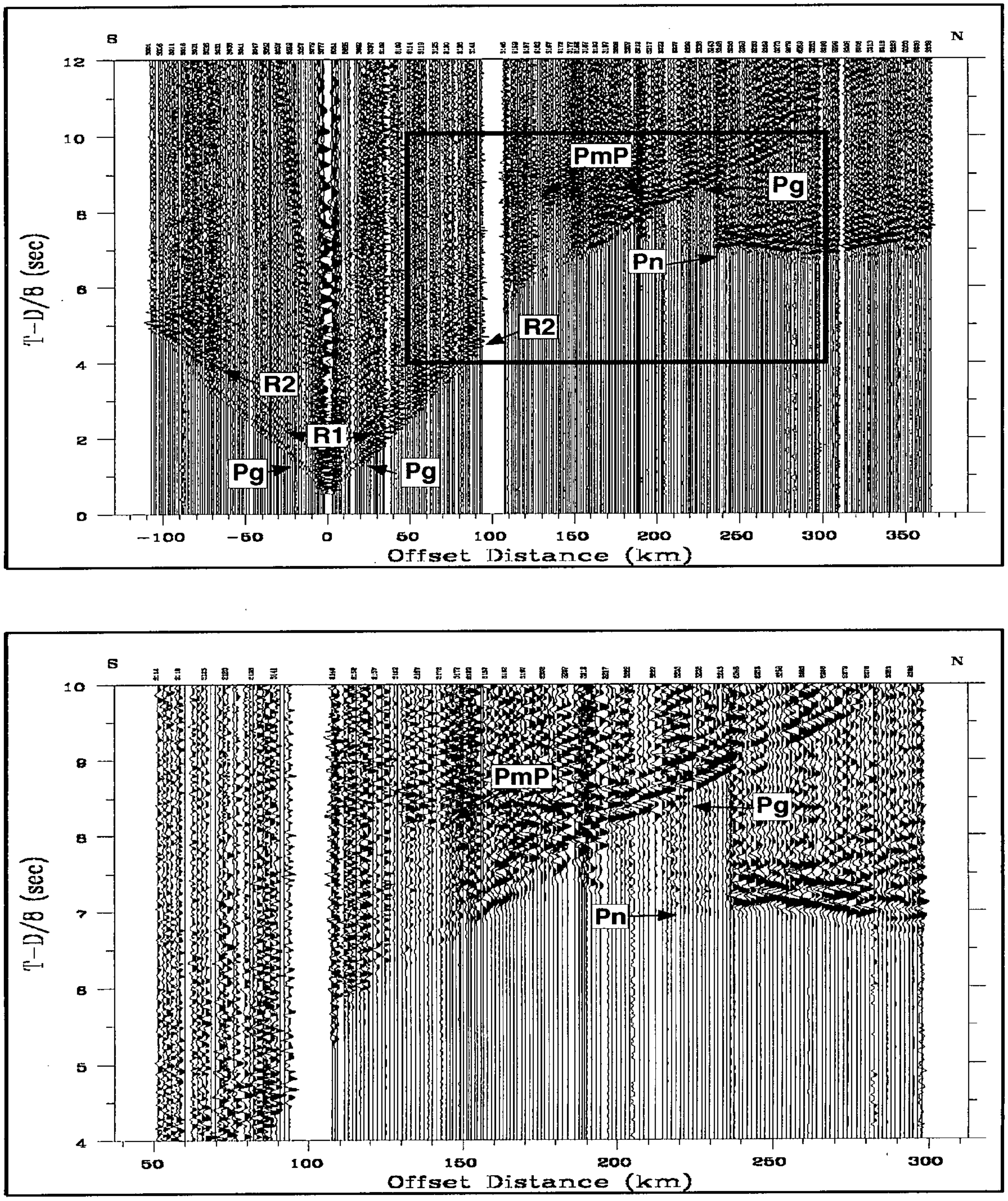

Figure 5.9: Observed trace normalised section for shot 303. a) The entire section. The box defines the inset position. b) Inset enhancing the PmP, Pg and Pn phases. The reducing velocity is 8 km/s and the distance is the offset distance from the shot point.

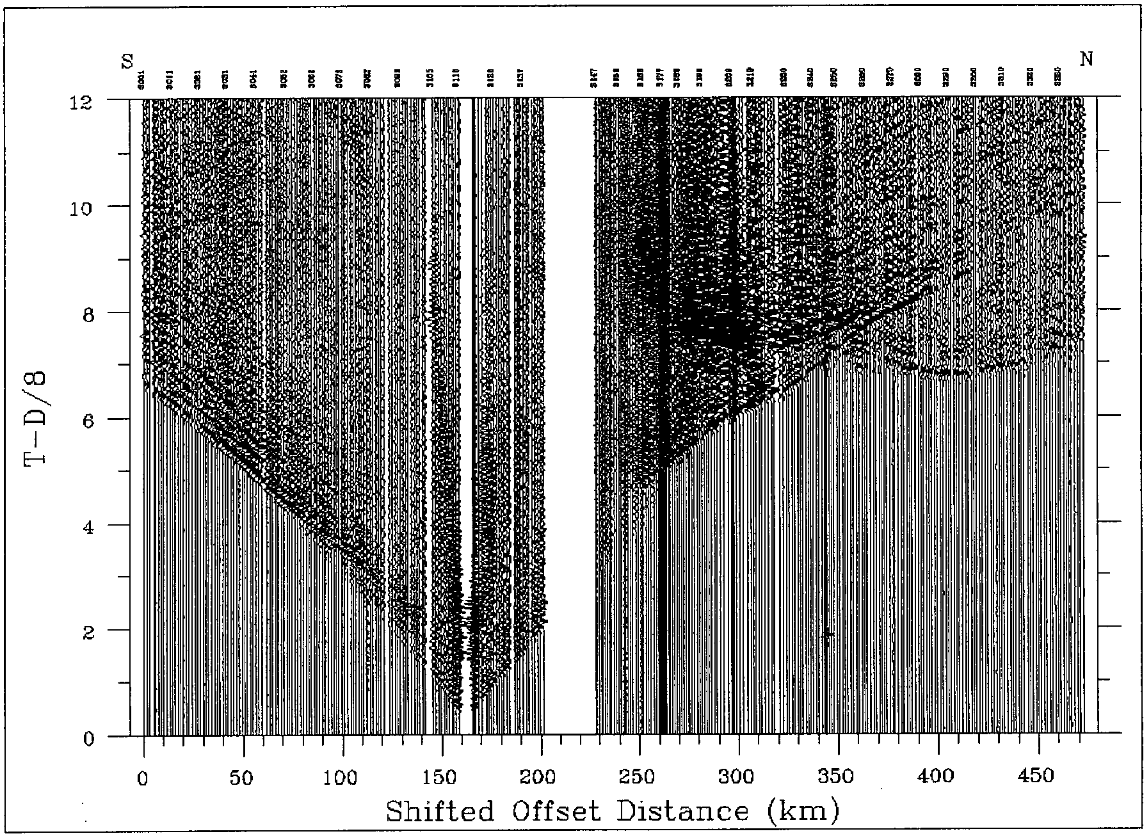

Figure 5.10: Observed true amplitude section for shot 304. The reducing velocity is 8 km/s and the distance is the offset distance from the shot point.

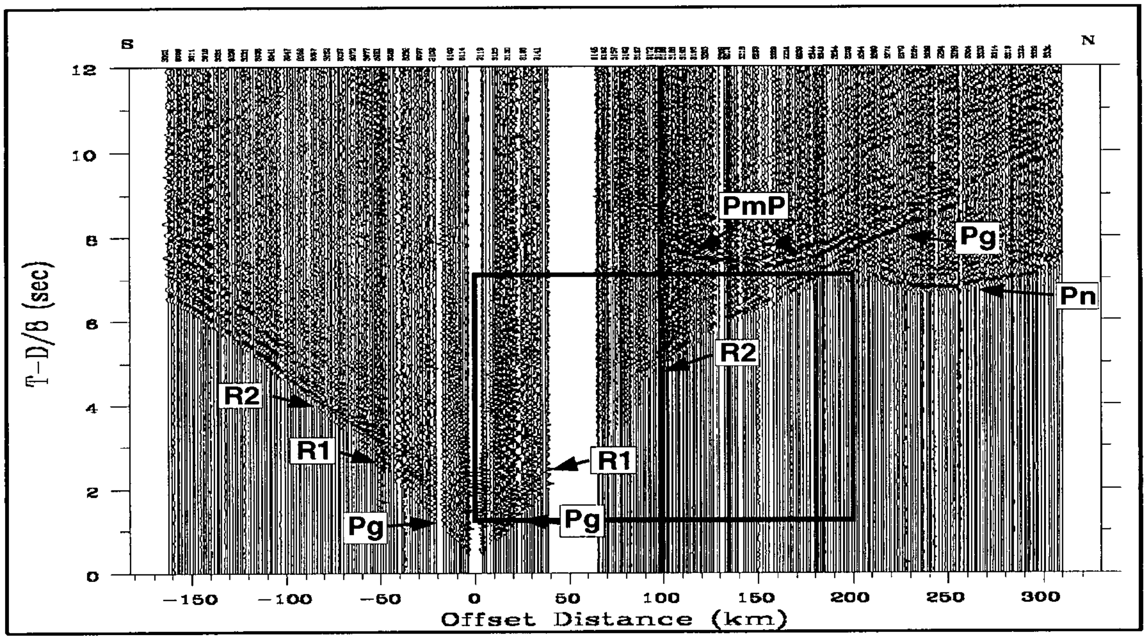

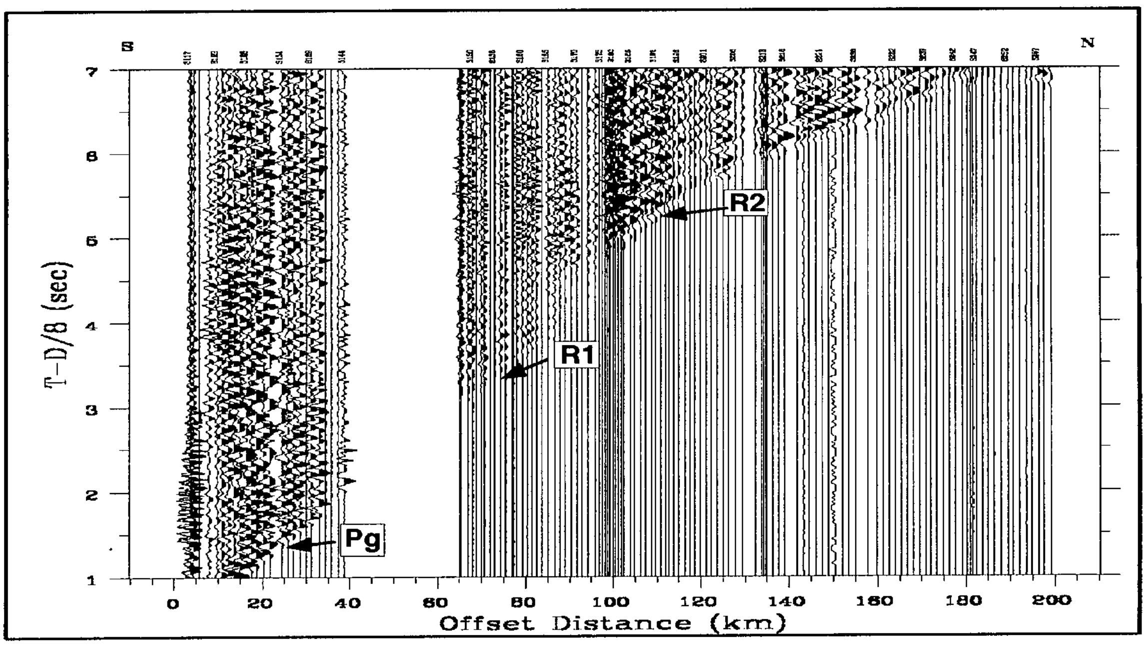

Figure 5.11: Observed trace normalised section for shot 304. a) The entire section. The box defines the inset position. b) Inset enhancing the Pg, R1 and R2 phases. The reducing velocity is 8 km/s and the distance is the offset distance from the shot point.

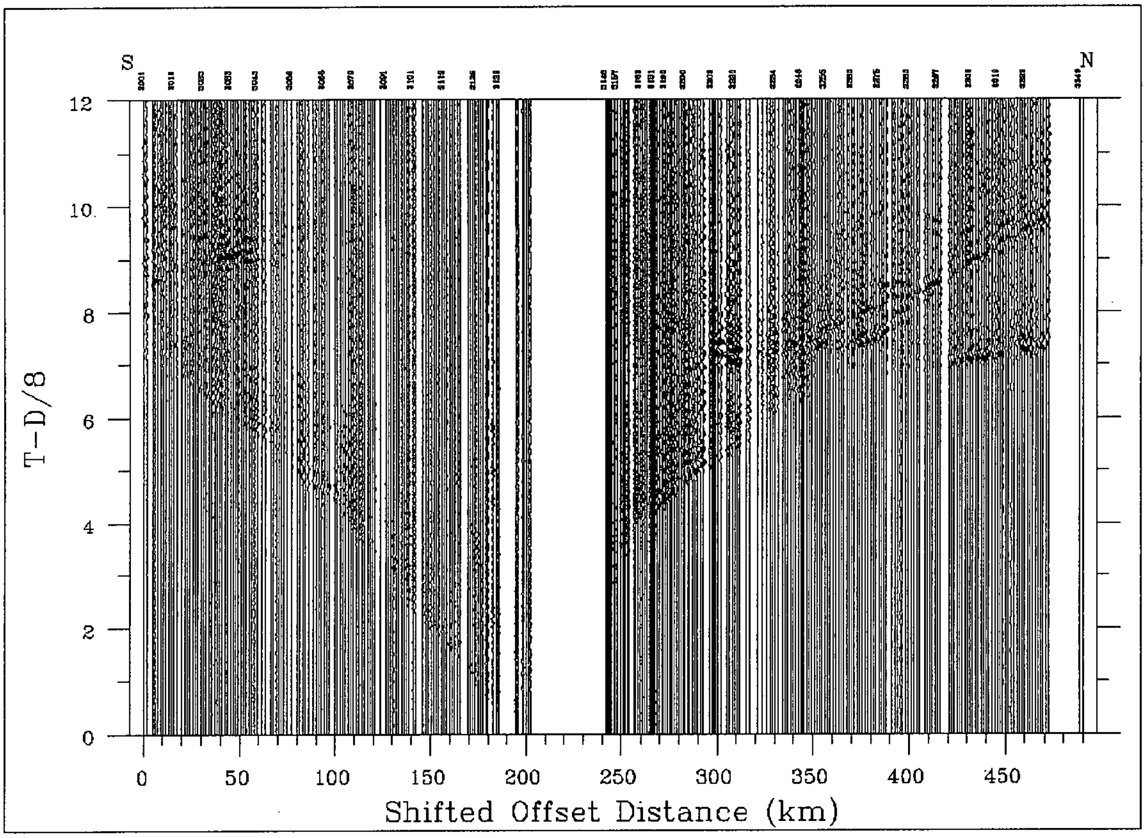

Figure 5.12: Observed true amplitude section for shot 305. The reducing velocity is 8 km/s and the distance is the offset distance from the shot point.

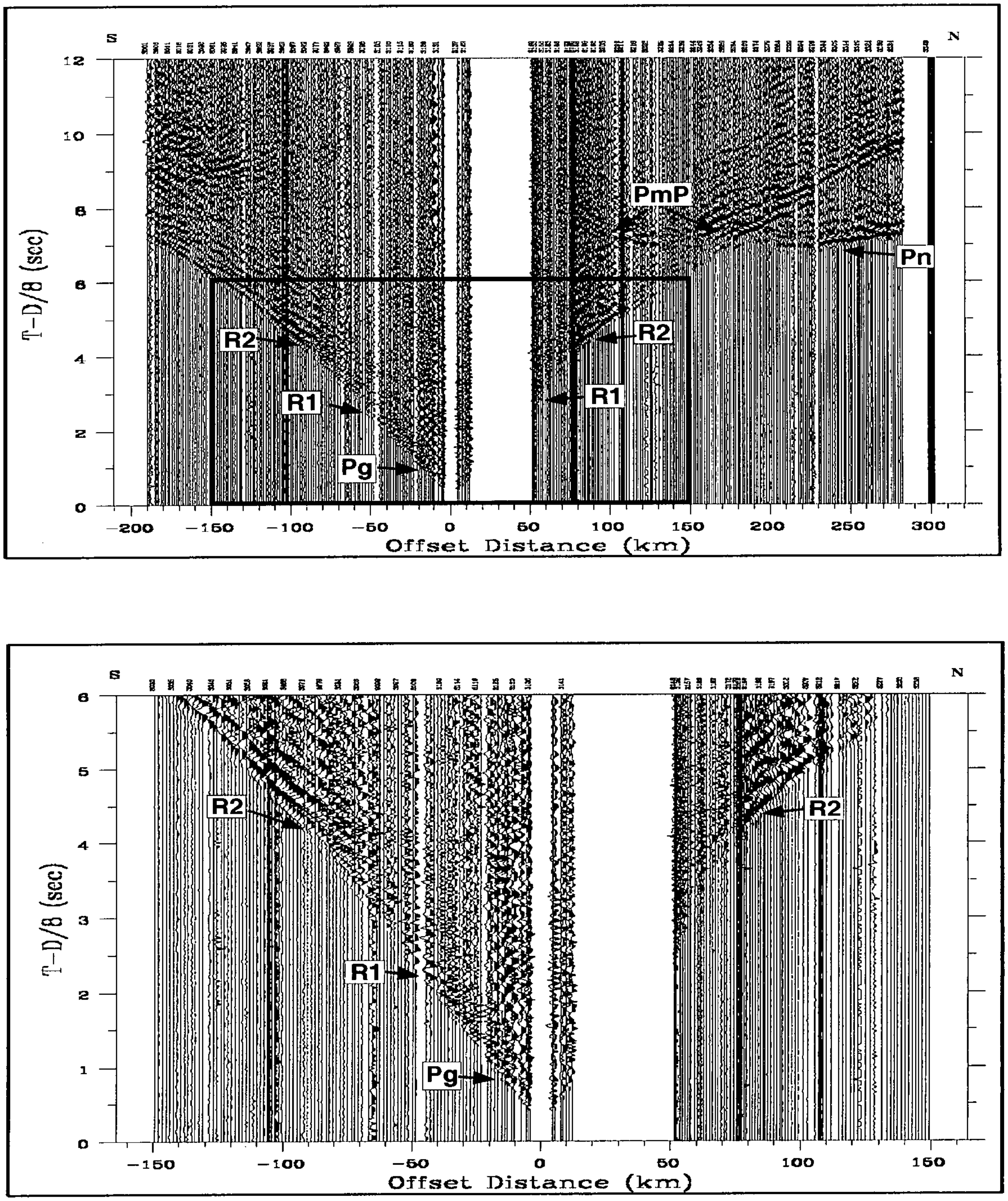

Figure 5.13: Observed trace normalised section for shot 305. a) The entire section. The box defines the inset position. b) Inset enhancing the Pg, R1 and R2 phases. The reducing velocity is 8 km/s and the distance is the offset distance from the shot point.

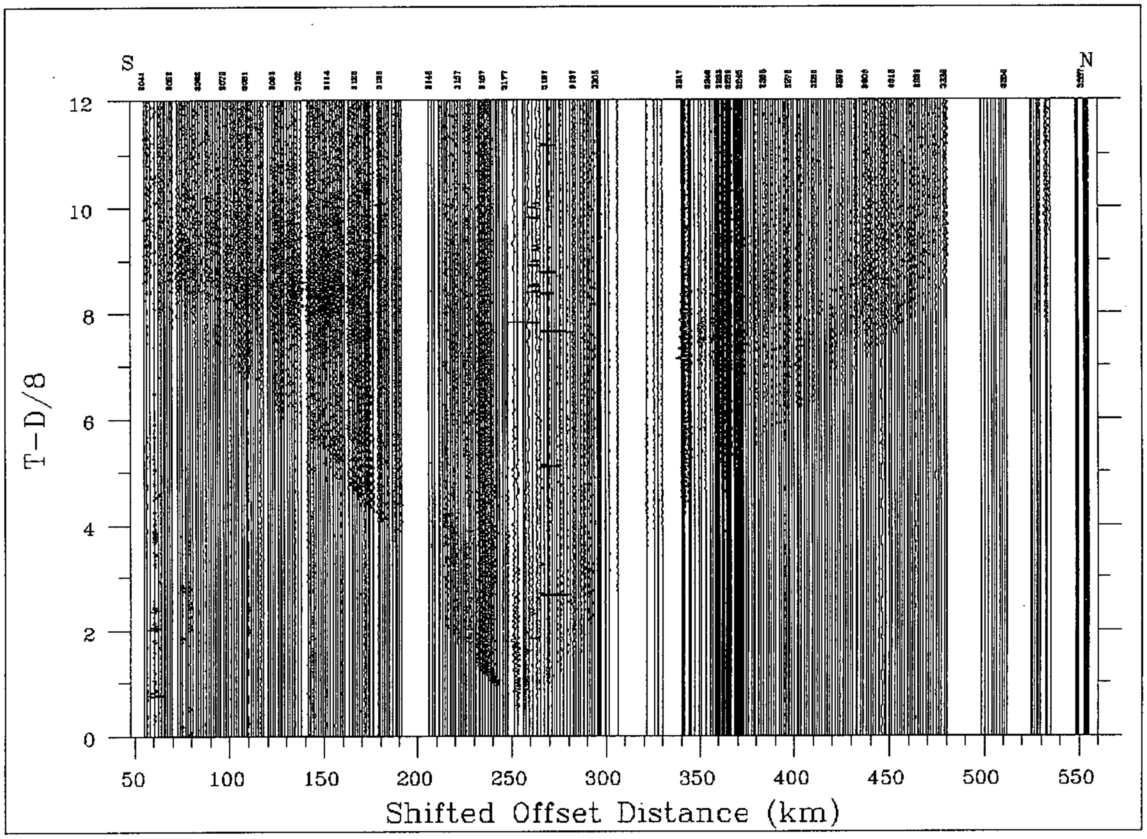

Figure 5.14: Observed true amplitude section for shot 306. The reducing velocity is 8 km/s and the distance is the offset distance from the shot point.

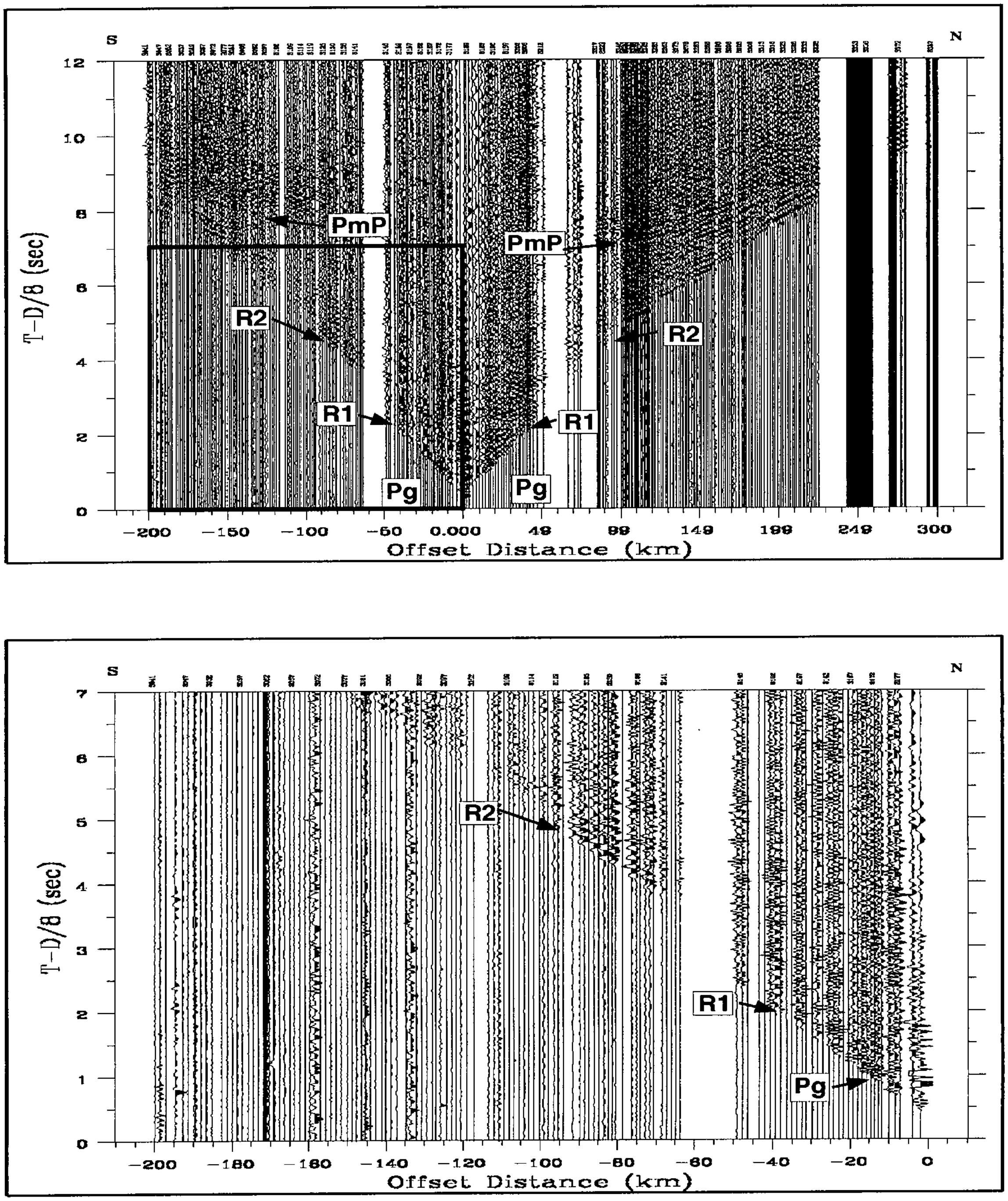

Figure 5.15: Observed trace normalised section for shot 306. a) The entire section. The box defines the inset position. b) Inset enhancing the Pg, R1 and R2 phases. The reducing velocity is 8 km/s and the distance is the offset distance from the shot point.

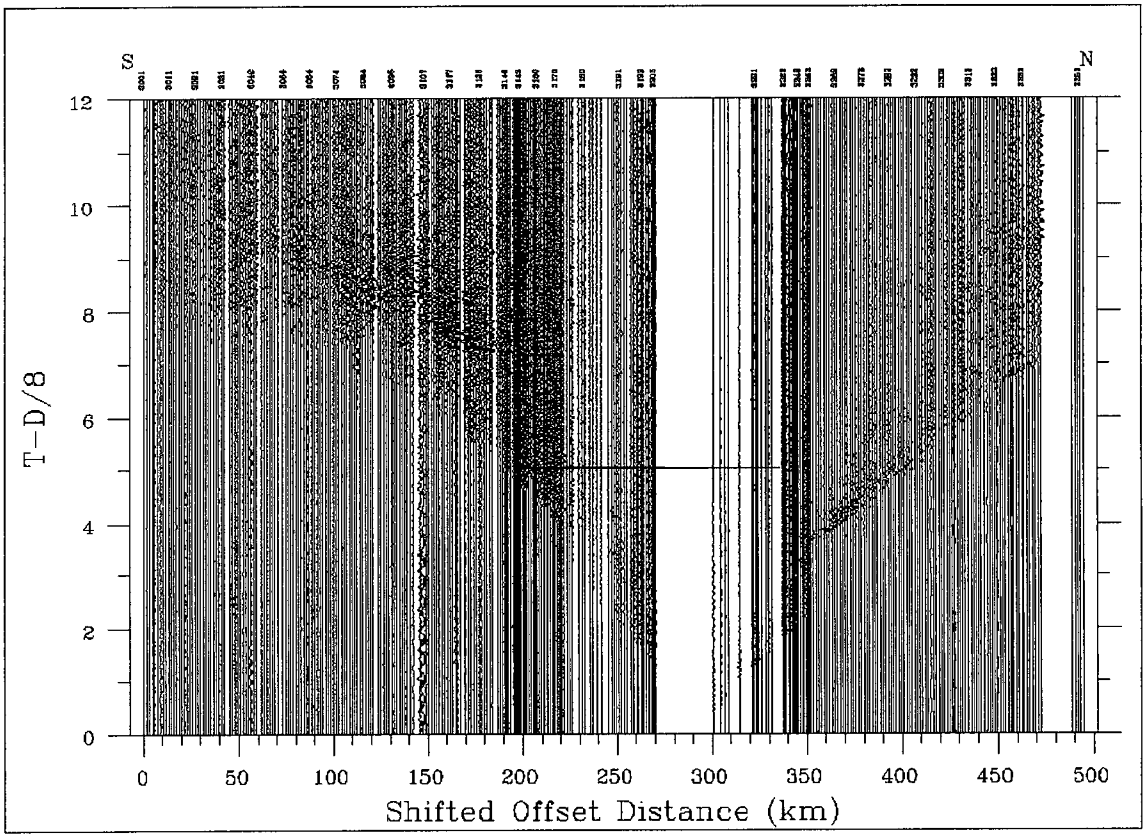

Figure 5.16: Observed true amplitude section for shot 307. The reducing velocity was 8 km/s and the distance is the offset distance from the shot point.

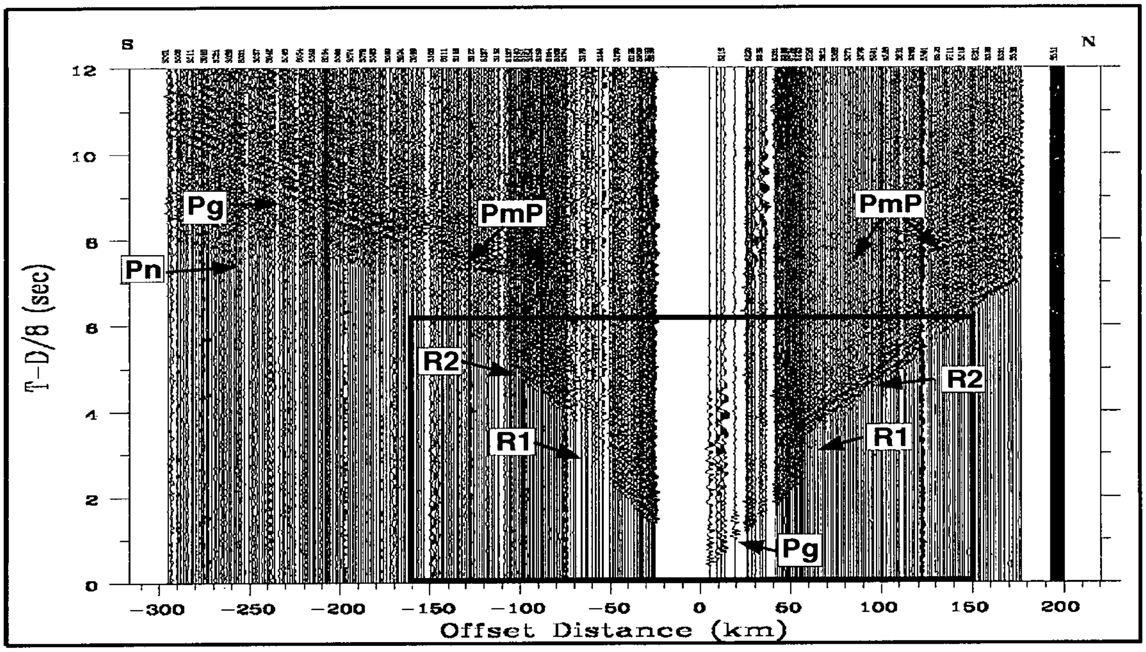

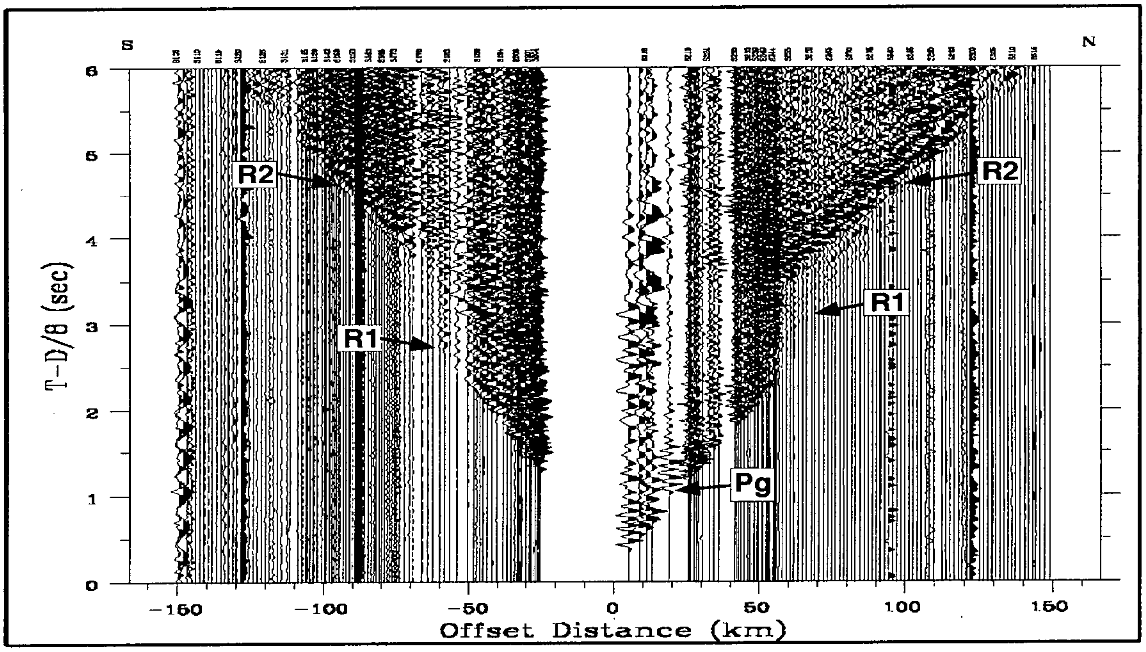

Figure 5.17: Observed trace normalised section for shot 307. a) The entire section. The box defines the inset position. b) Inset enhancing the Pg, R1 and R2 phases. The reducing velocity is 8 km/s and the distance is the offset distance from the shot point.

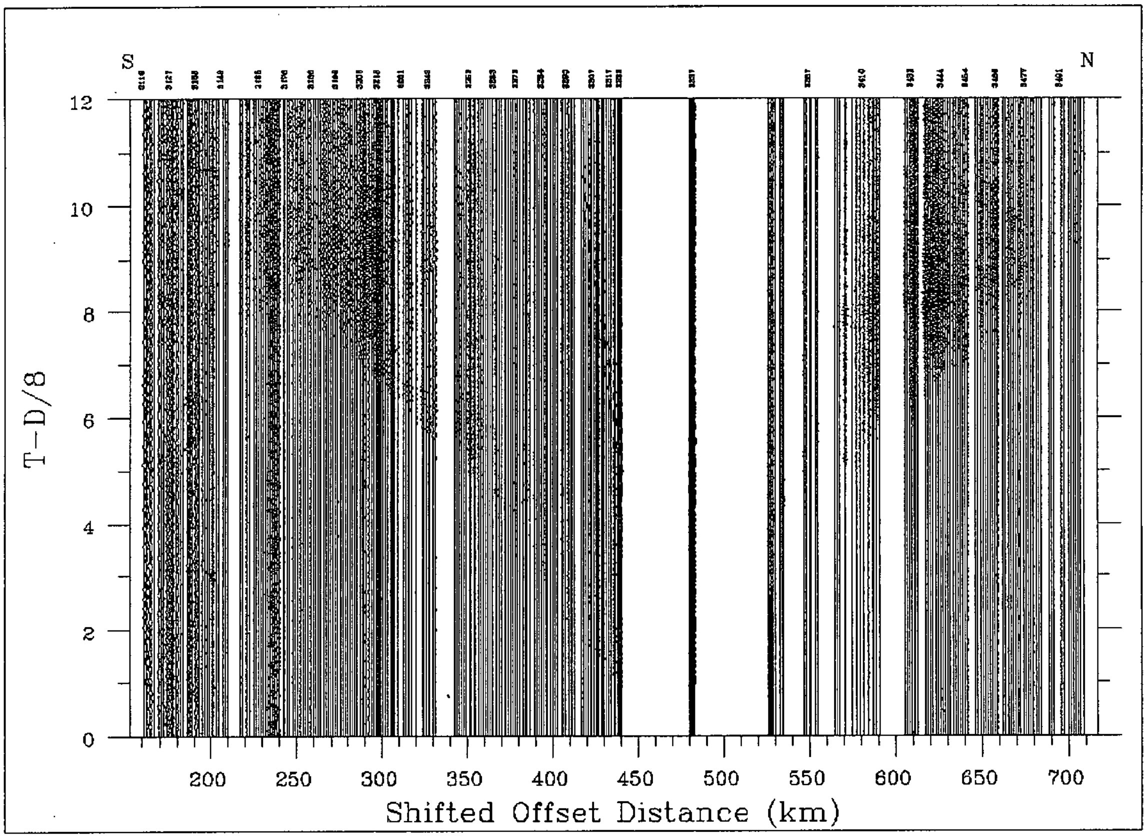

Figure 5.18: Observed true amplitude section for shot 308. The reducing velocity is 8 km/s and the distance is the offset distance from the shot point.

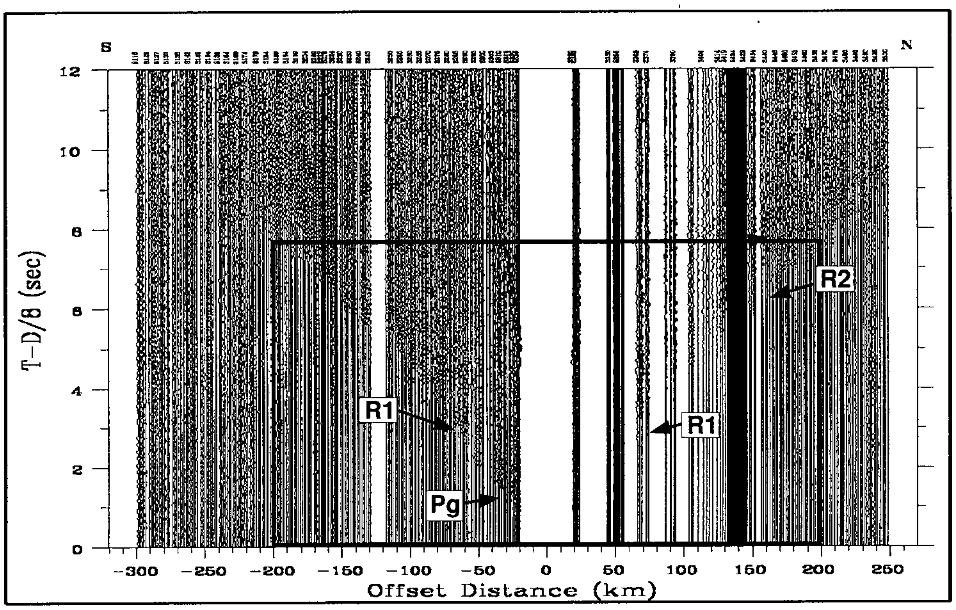

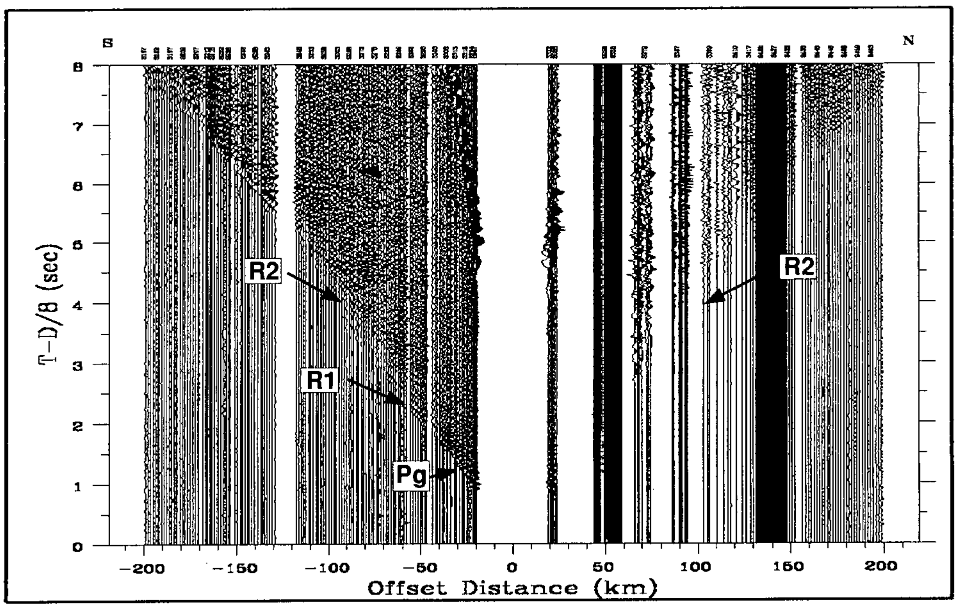

Figure 5.19: Observed trace normalised section for shot 308. a) The entire section. The box defines the inset position. b) Inset enhancing the Pg, R1 and R2 phases. The reducing velocity is 8 km/s and the distance is the offset distance from the shot point.

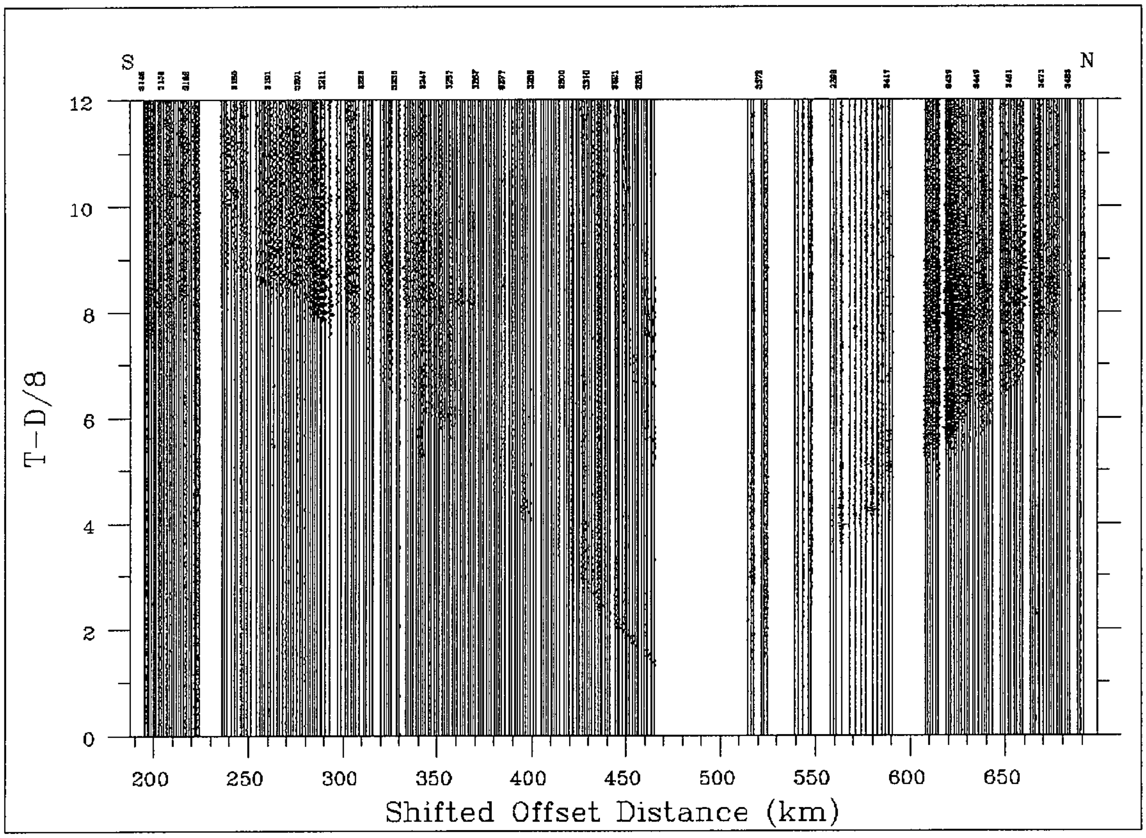

Figure 5.20: Observed true amplitude section for shot 309. The reducing velocity is 8 km/s and the distance is the offset distance from the shot point.

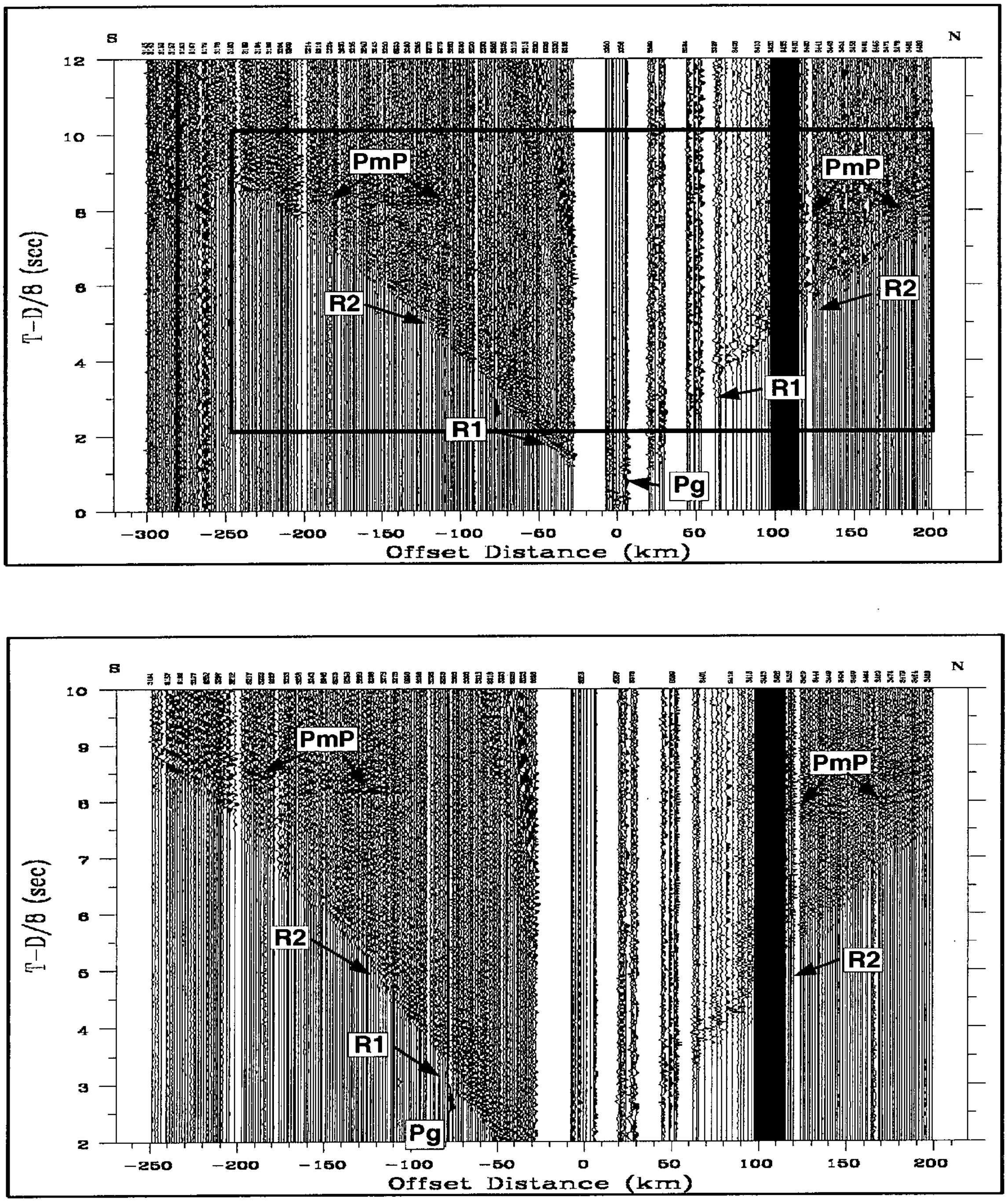

Figure 5.21: Observed trace normalised section for shot 309. a) The entire section. The box defines the inset position. b) Inset enhancing the R1, R2 and PmP phases. The reducing velocity is 8 km/s and the distance is the offset distance from the shot point.

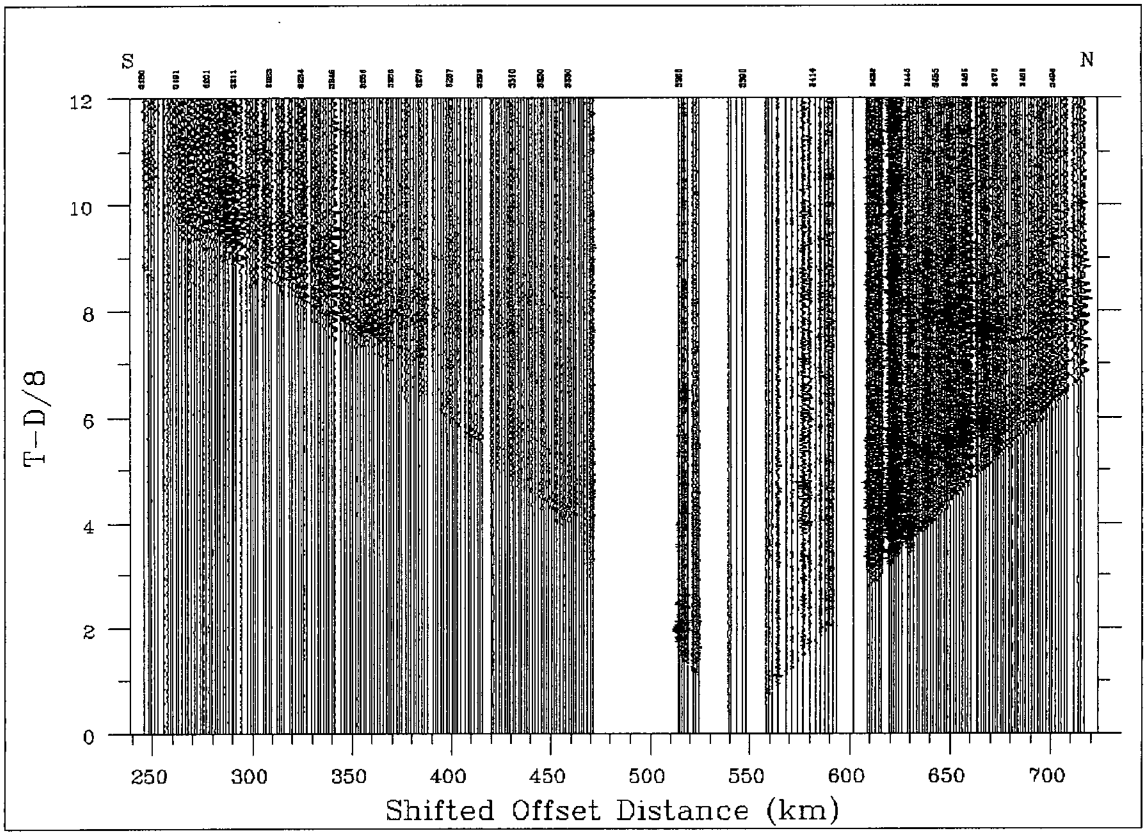

Figure 5.22: Observed true amplitude section for shot 310. The reducing velocity is 8 km/s and the distance is the offset distance from the shot point.

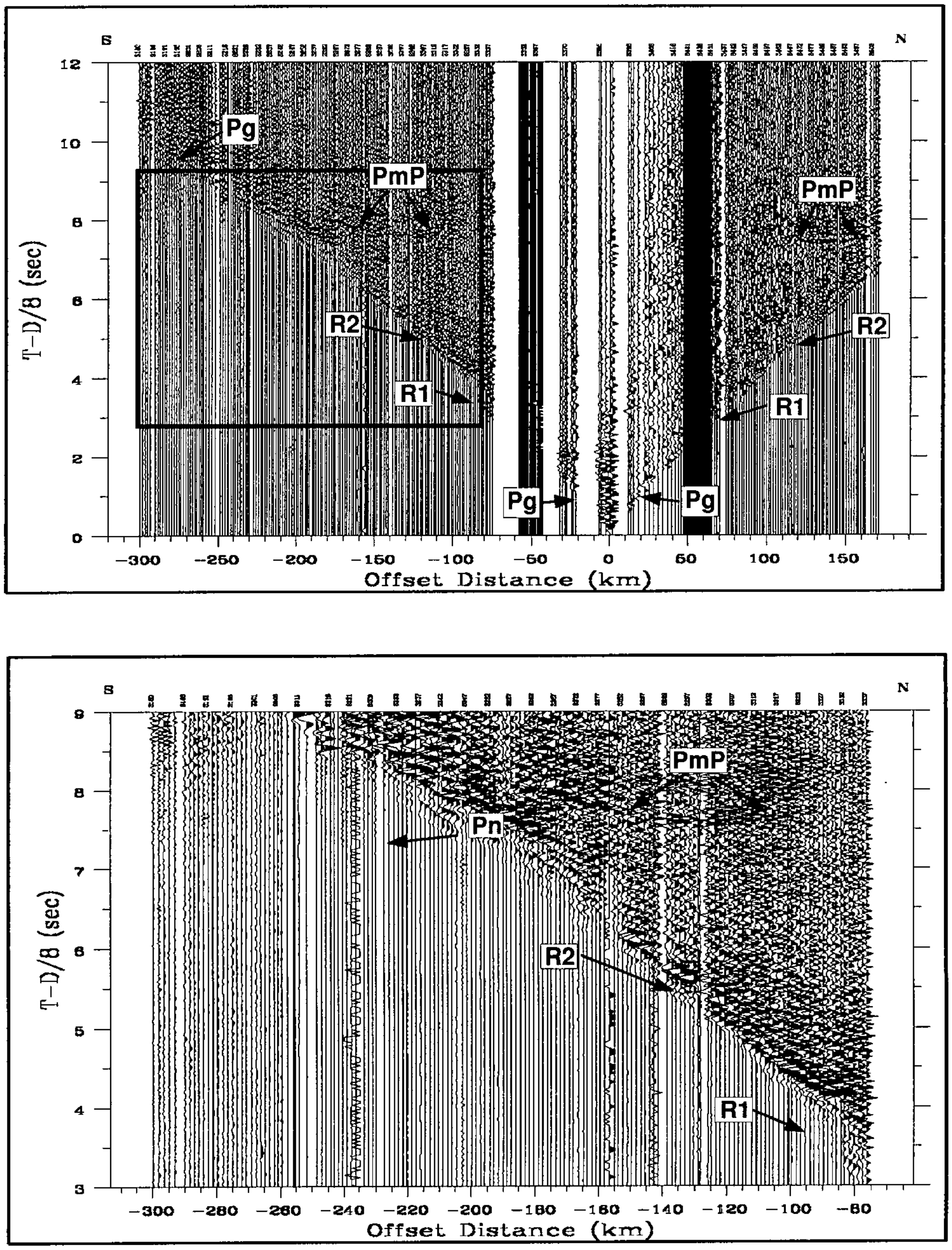

Figure 5.23: Observed trace normalised section for shot 310. a) The entire section. The box defines the inset position. b) Inset enhancing the R1, R2, PmP and Pn phases. The reducing velocity is 8 km/s and the distance is the offset distance from the shot point.

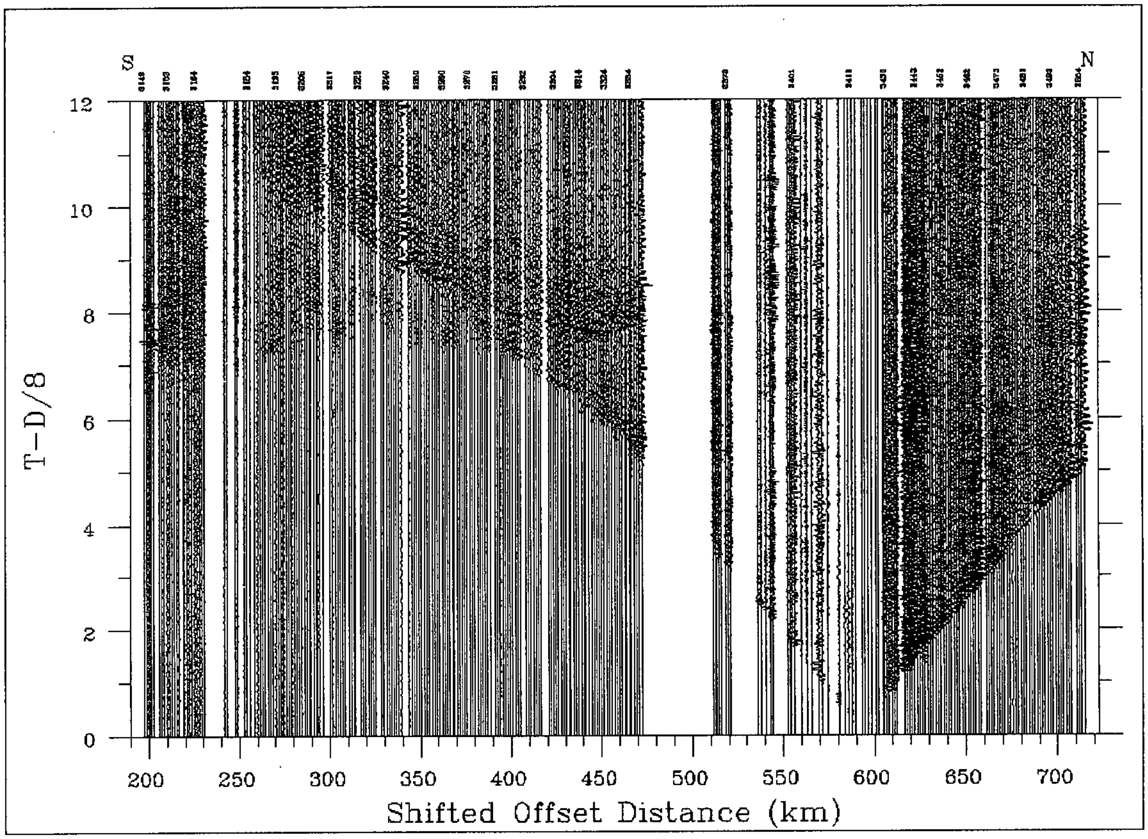

Figure 5.24: Observed true amplitude section for shot 311. The reducing velocity is 8 km/s and the distance is the offset distance from the shot point.

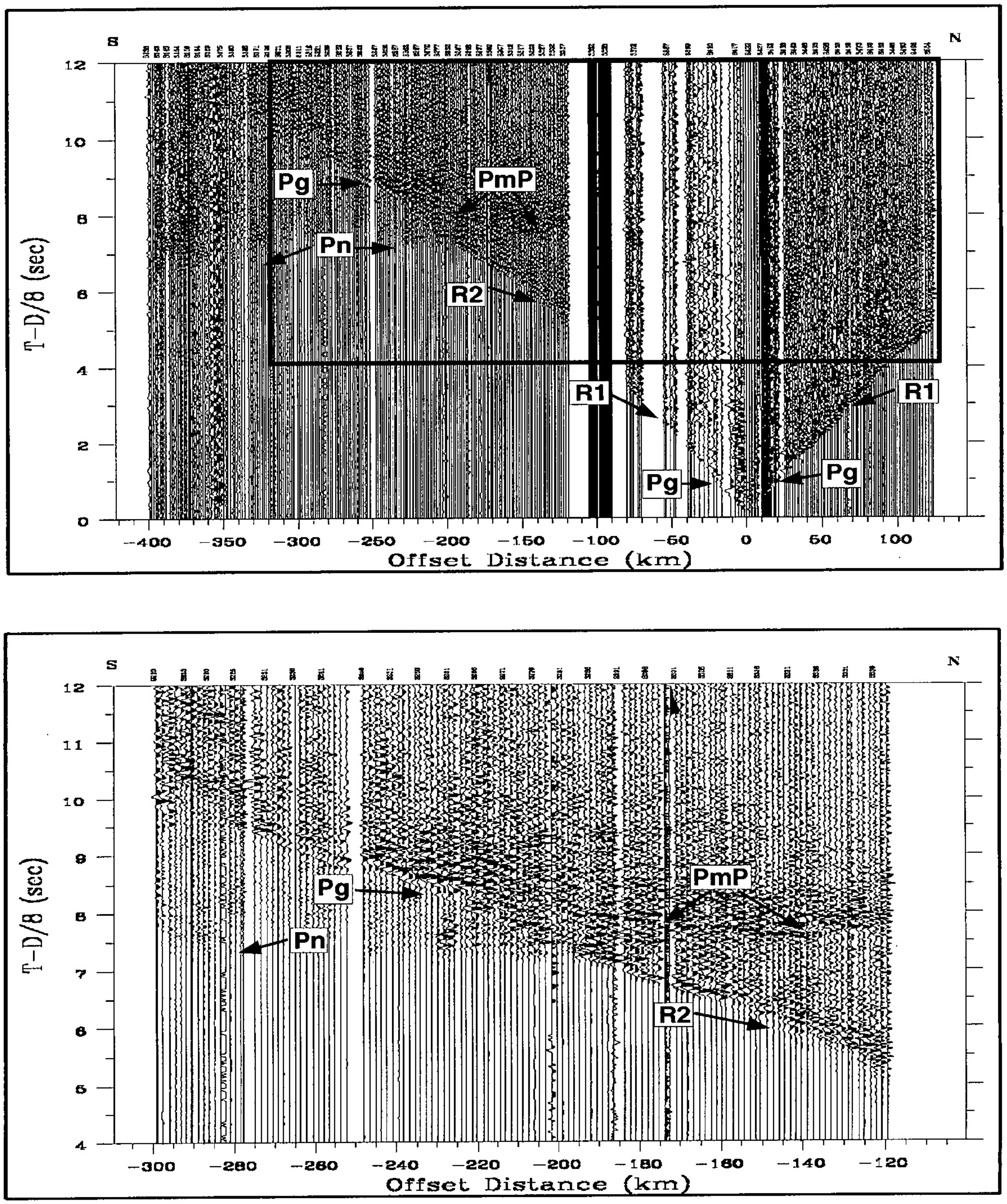

Figure 5.25: Observed trace normalised section for shot 311. a) The entire section. The box defines the inset position. b) Inset enhancing the Pg, Pn, PmP and R2 phases. The reducing velocity is 8 km/s and the distance is the offset distance from the shot point.

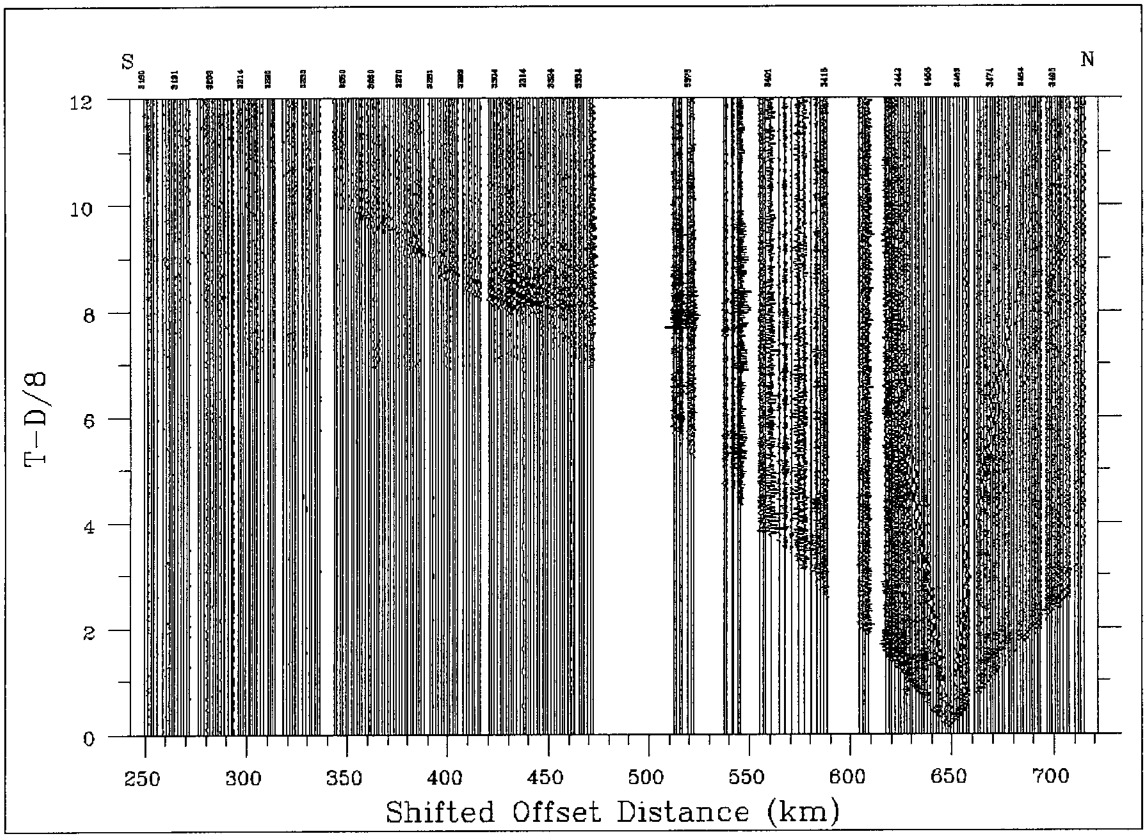

Figure 5.26: Observed true amplitude section for shot 312. The reducing velocity is 8 km/s and the distance is the offset distance from the shot point.

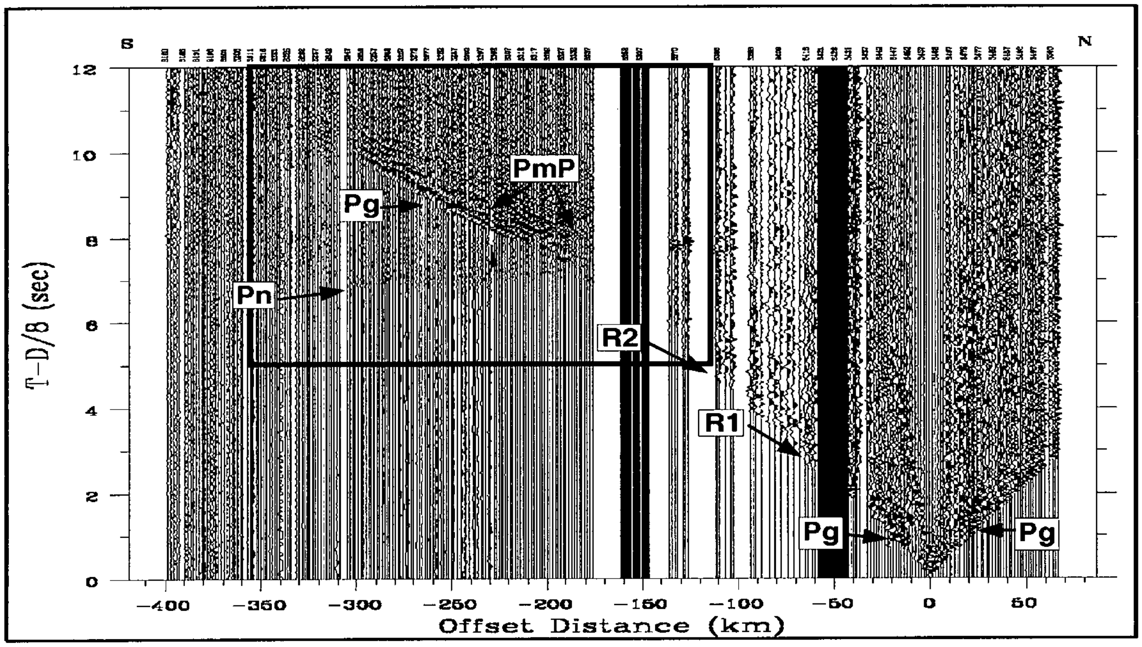

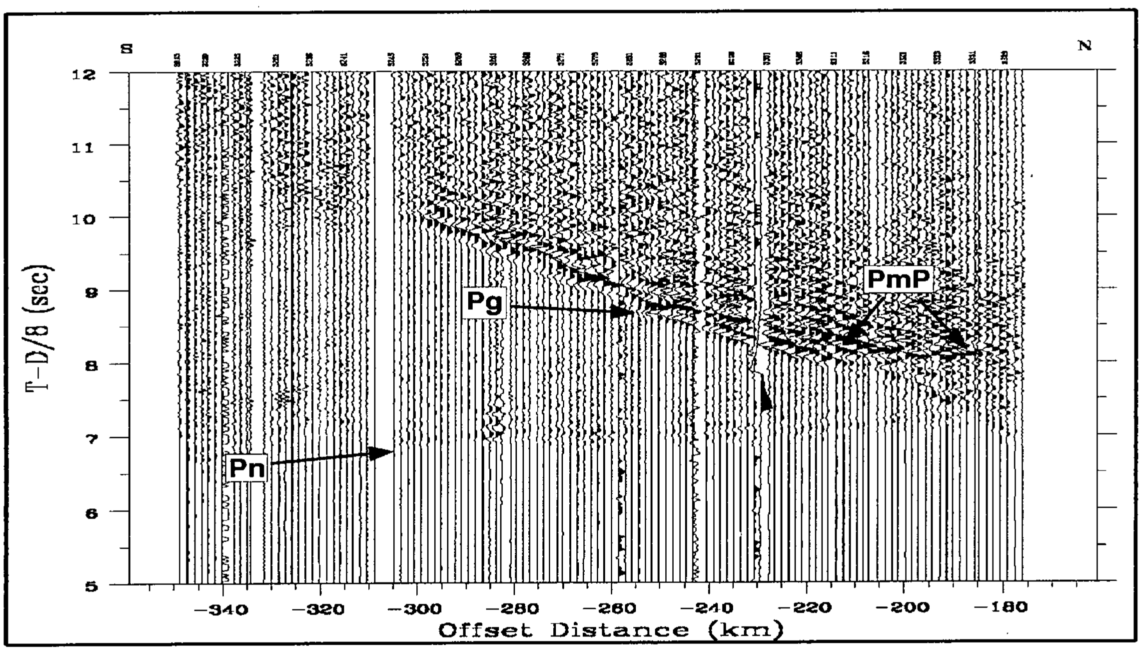

Figure 5.27: Observed trace normalised section for shot 312. a) The entire section. The box defines the inset position. b) Inset enhancing the Pg, Pn and PmP phases. The reducing velocity is 8 km/s and the distance is the offset distance from the shot point.

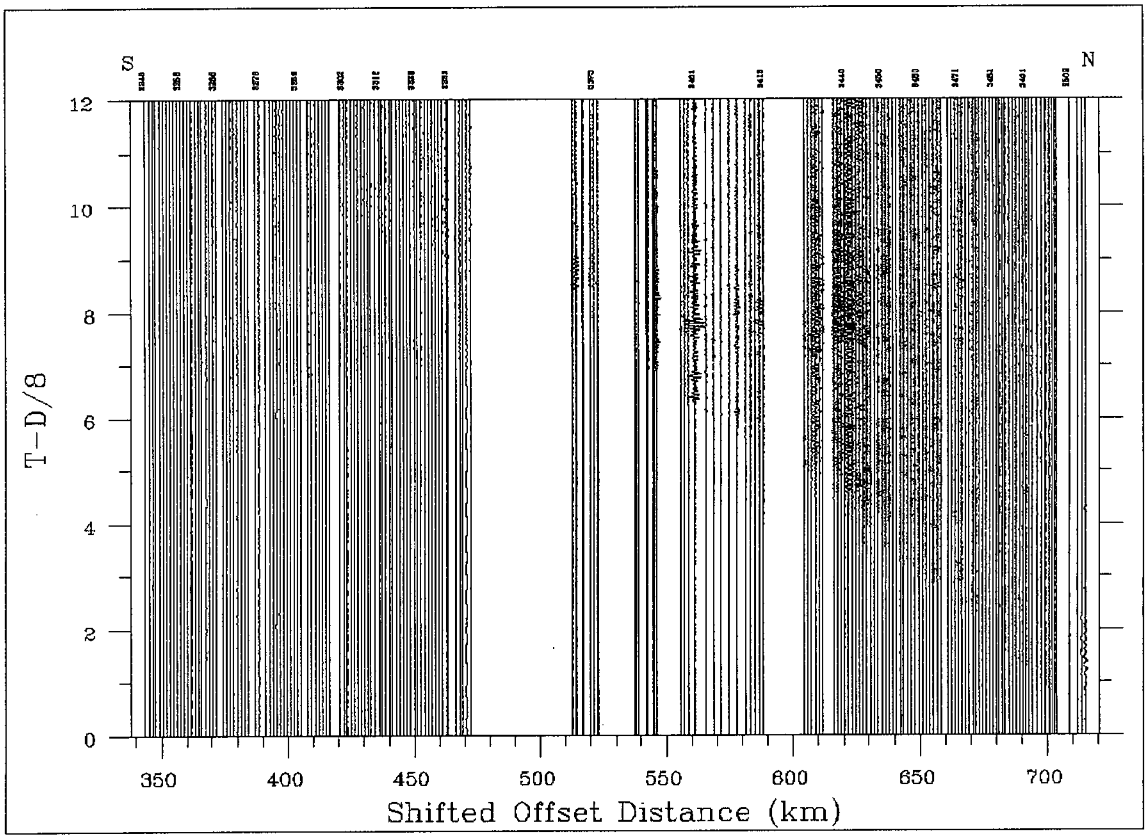

Figure 5.28: Observed true amplitude section for shot 313. The reducing velocity is 8 km/s and the distance is the offset distance from the shot point.

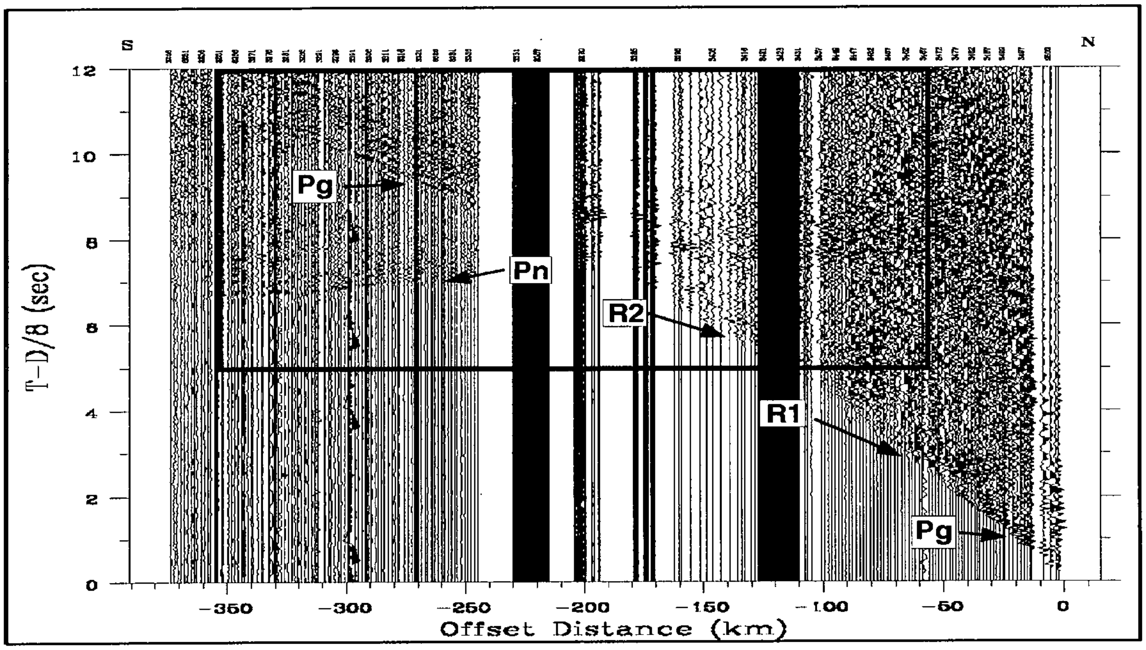

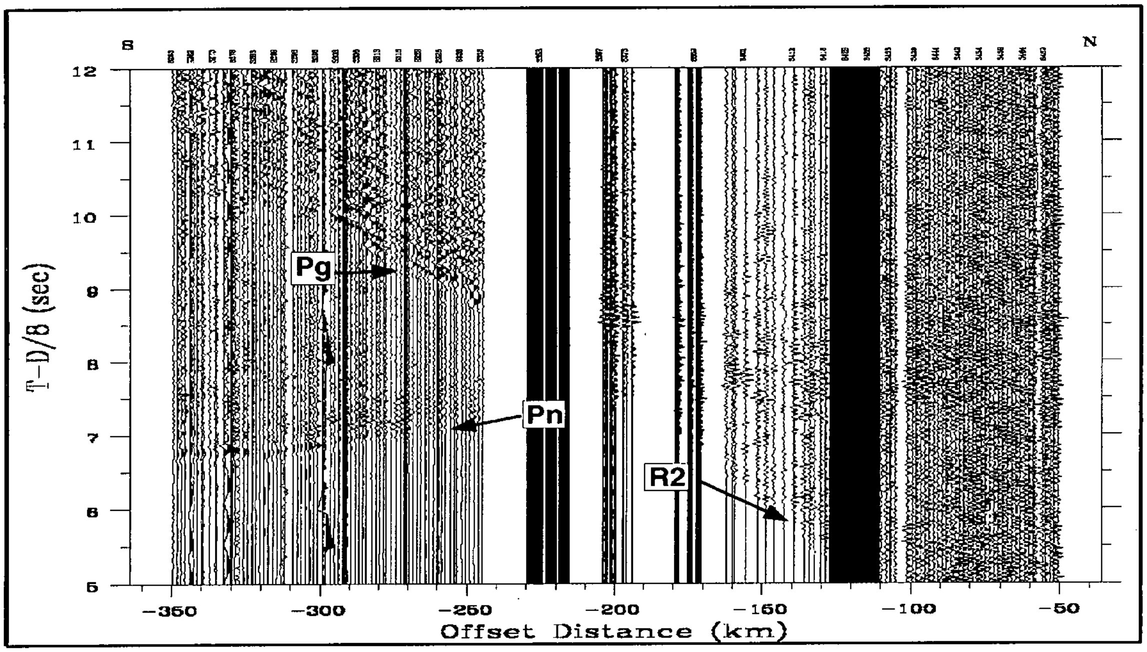

Figure 5.29: Observed trace normalised section for shot 313. a) The entire section. The box defines the inset position. b) Inset enhancing the Pg, Pn and R2 phases. The reducing velocity is 8 km/s and the distance is the offset distance from the shot point.

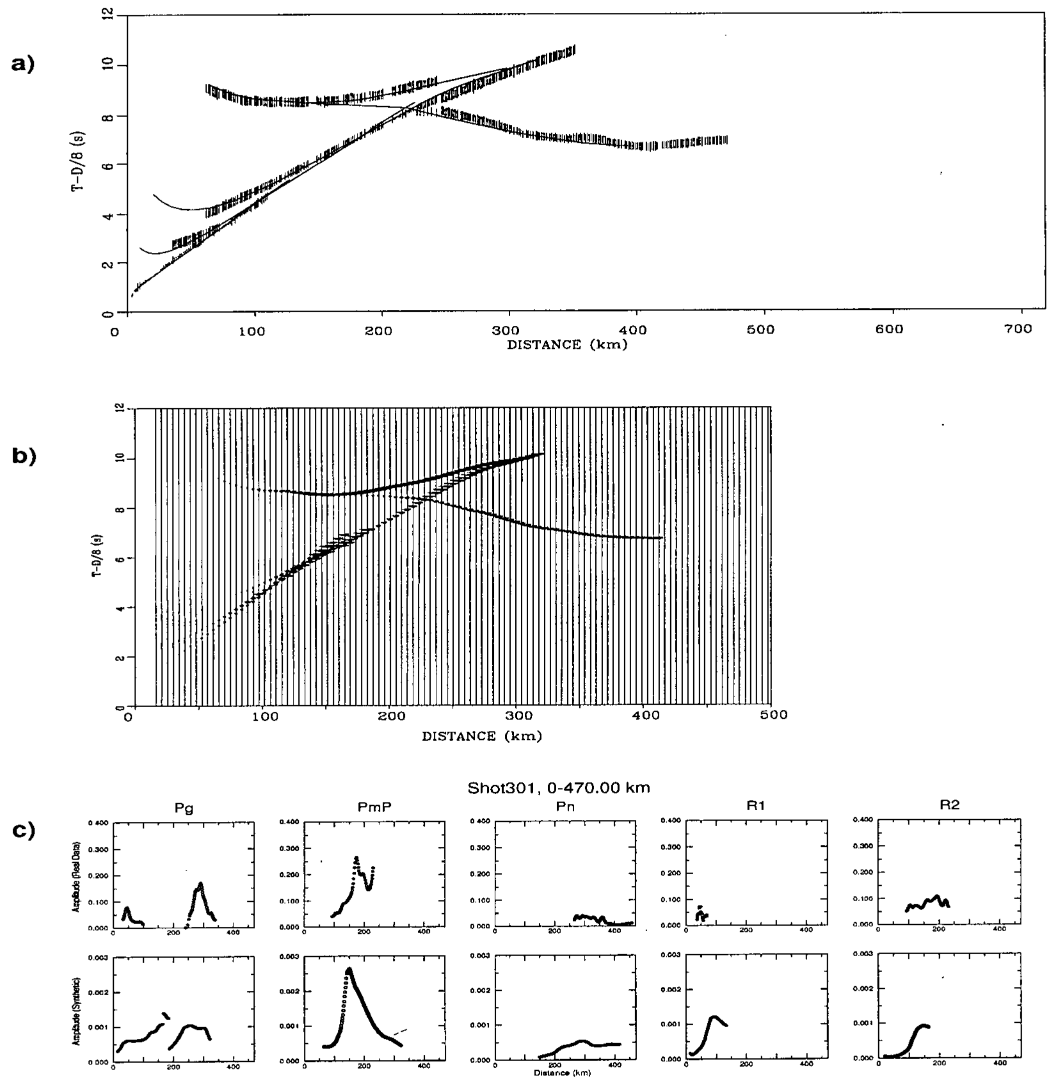

Figure 5.30: Shot 301. a) Fit between calculated and observed data. Vertical lines represent picking error of observed data. Calculated data are represented by a solid line. b) Synthetic seismogram sections. c) Comparison between true (above) and synthetic (below) amplitude trends.

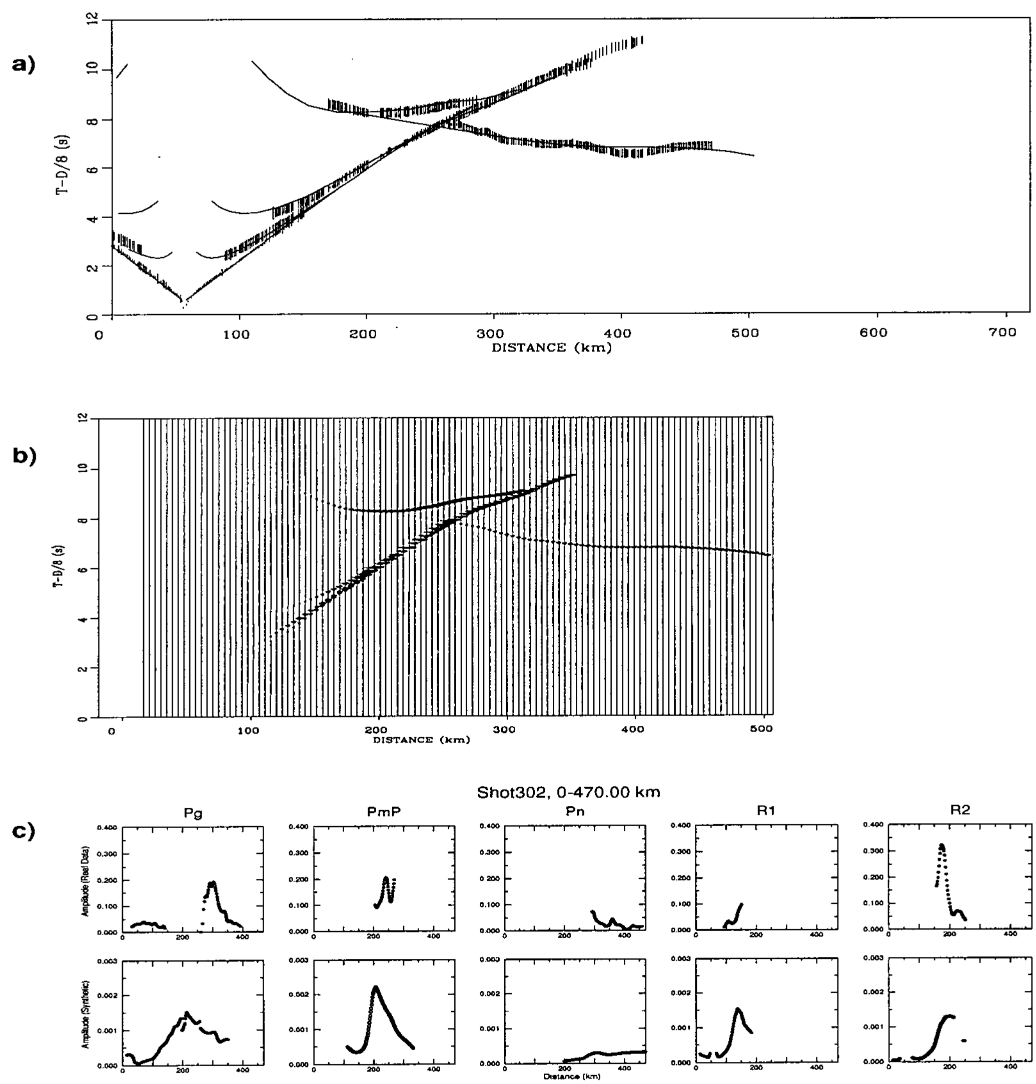

Figure 5.31: Shot 302. a) Fit between calculated and observed data. Vertical lines represent picking error of observed data. Calculated data are represented by a solid line. b) Synthetic seismogram sections. c) Comparison between true (above) and synthetic (below) amplitude trends.

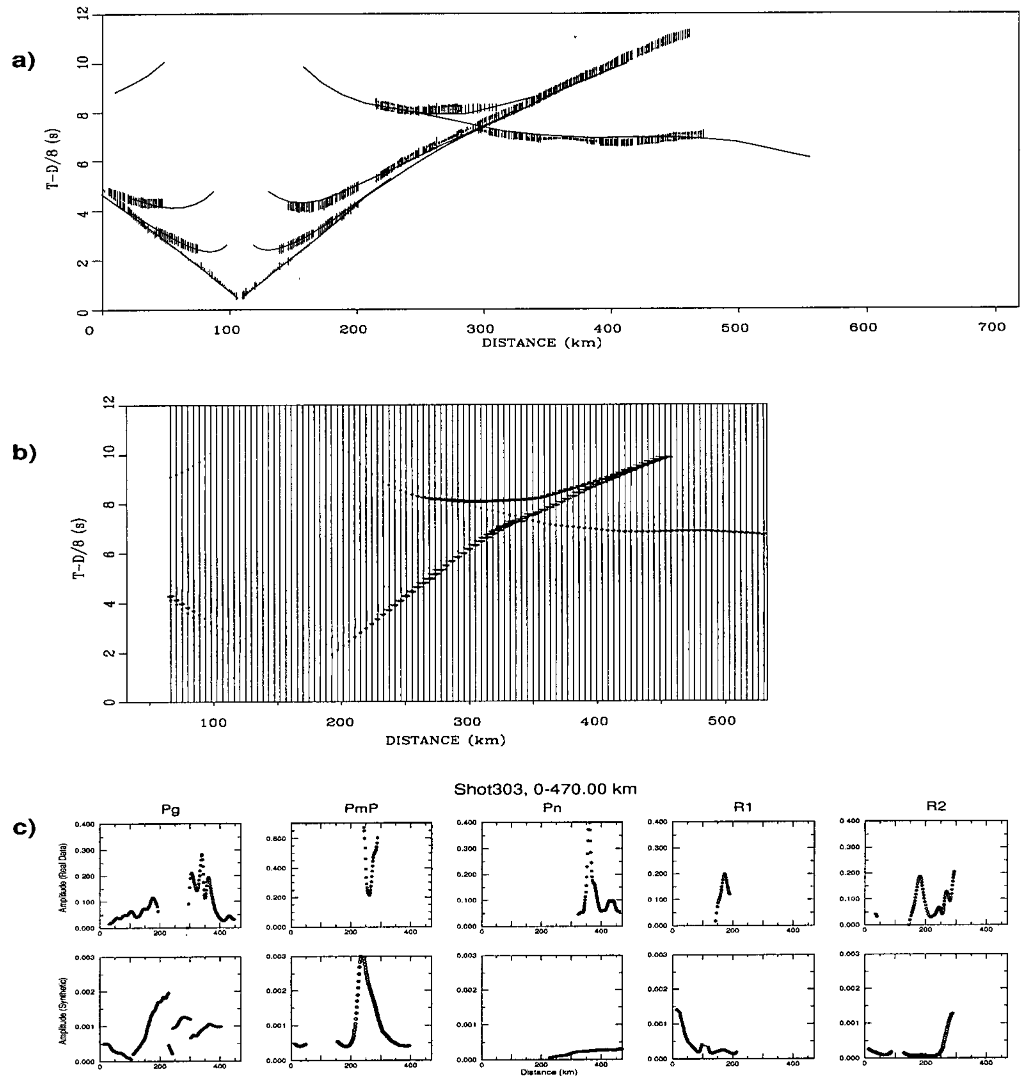

Figure 5.32: Shot 303. a) Fit between calculated and observed data. Vertical lines represent picking error of observed data. Calculated data are represented by a solid line. b) Synthetic seismogram sections. c) Comparison between true (above) and synthetic (below) amplitude trends.

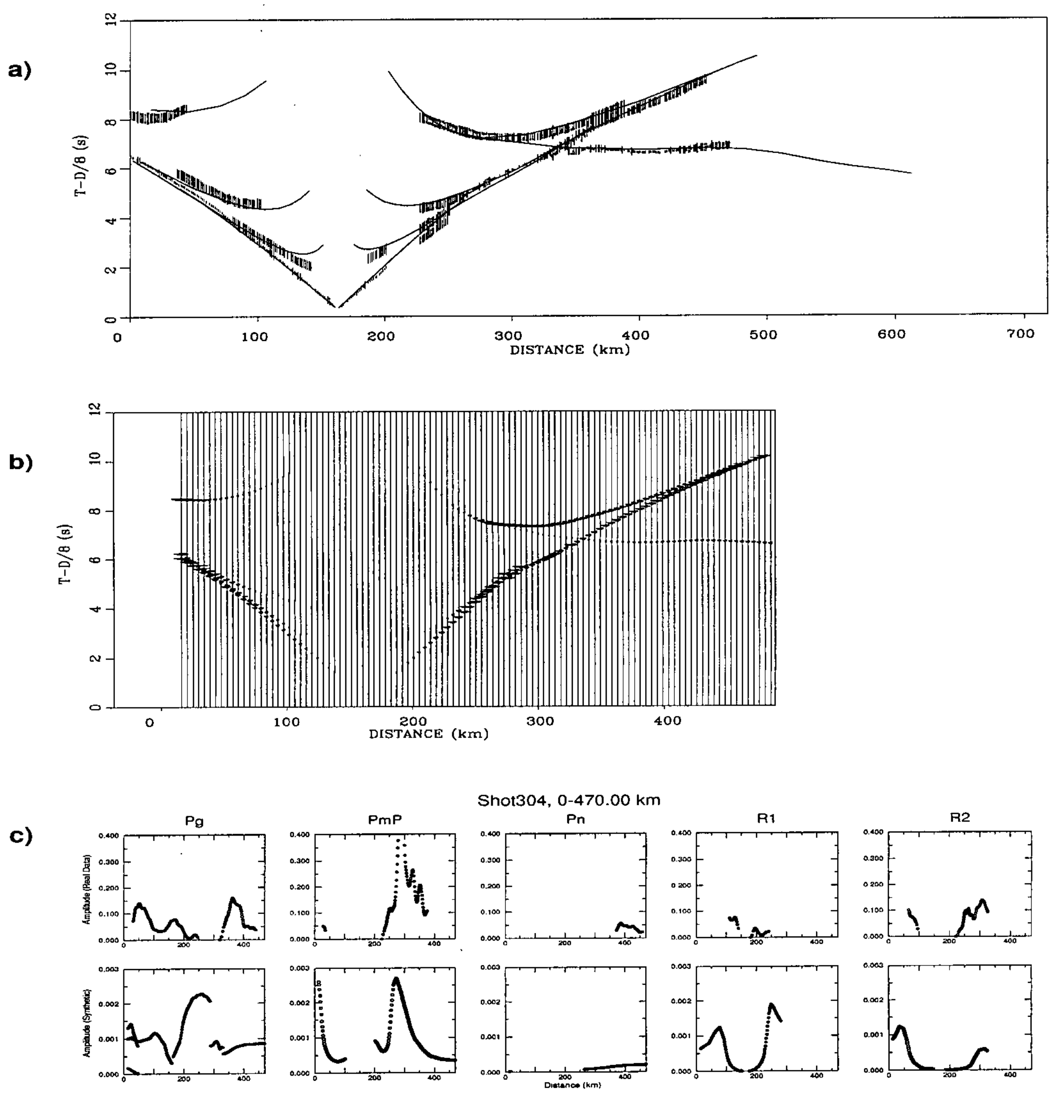

Figure 5.33: Shot 304. a) Fit between calculated and observed data. Vertical lines represent picking error of observed data. Calculated data are represented by a solid line. b) Synthetic seismogram sections. c) Comparison between true (above) and synthetic (below) amplitude trends.

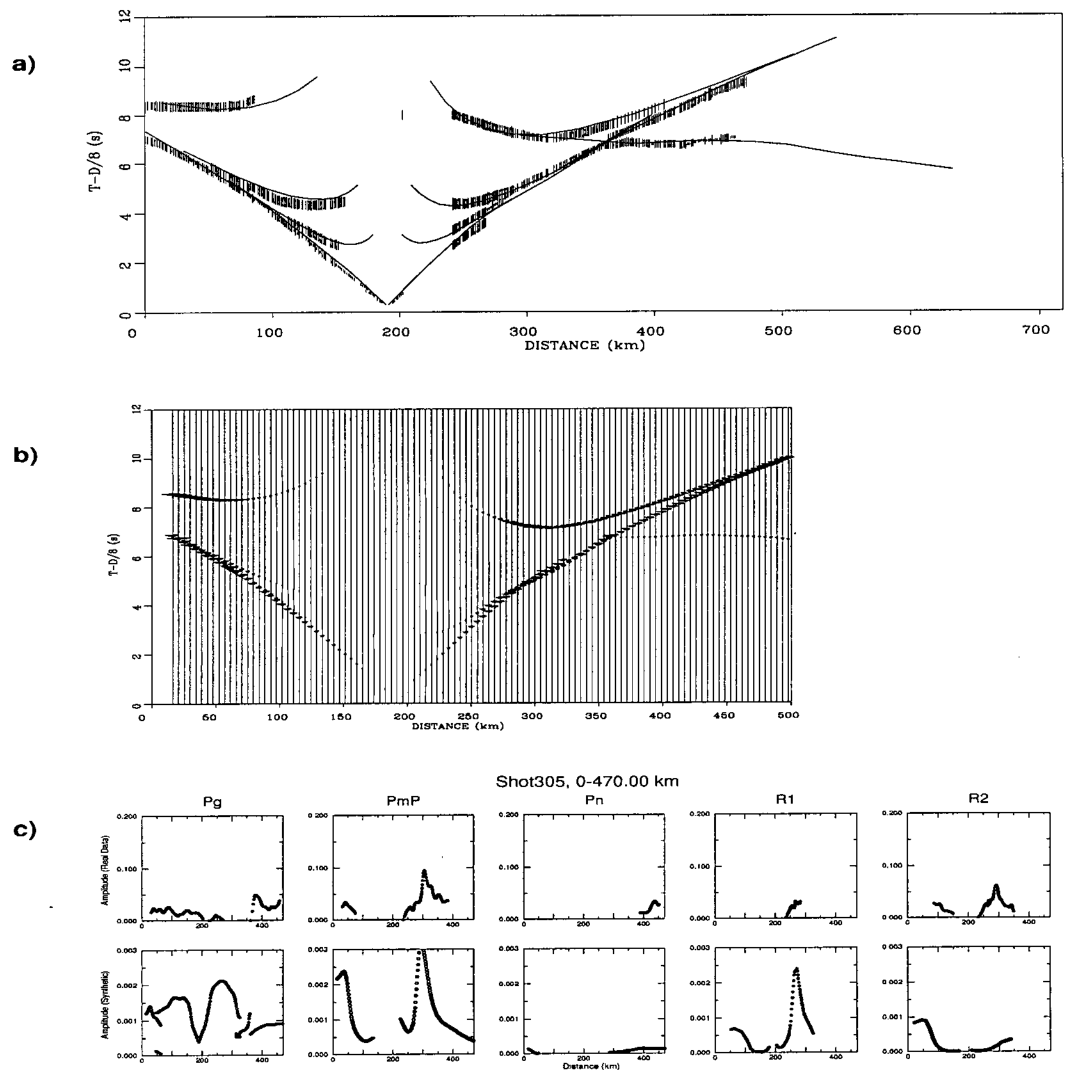

Figure 5.34: Shot 305. a) Fit between calculated and observed data. Vertical lines represent picking error of observed data. Calculated data are represented by a solid line. b) Synthetic seismogram sections. c) Comparison between true (above) and synthetic (below) amplitude trends.

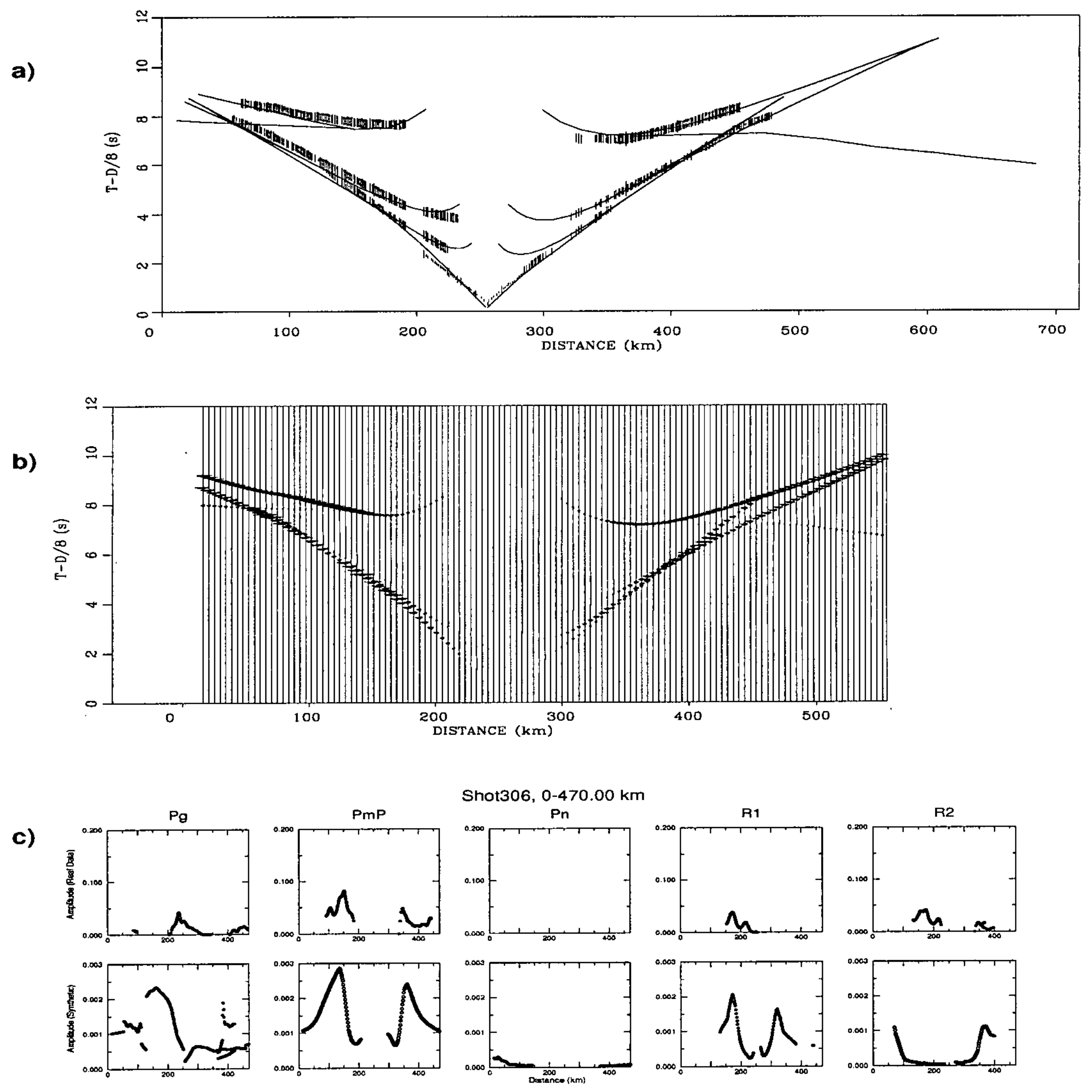

Figure 5.35: Shot 306. a) Fit between calculated and observed data. Vertical lines represent picking error of observed data. Calculated data are represented by a solid line. b) Synthetic seismogram sections. c) Comparison between true (above) and synthetic (below) amplitude trends.

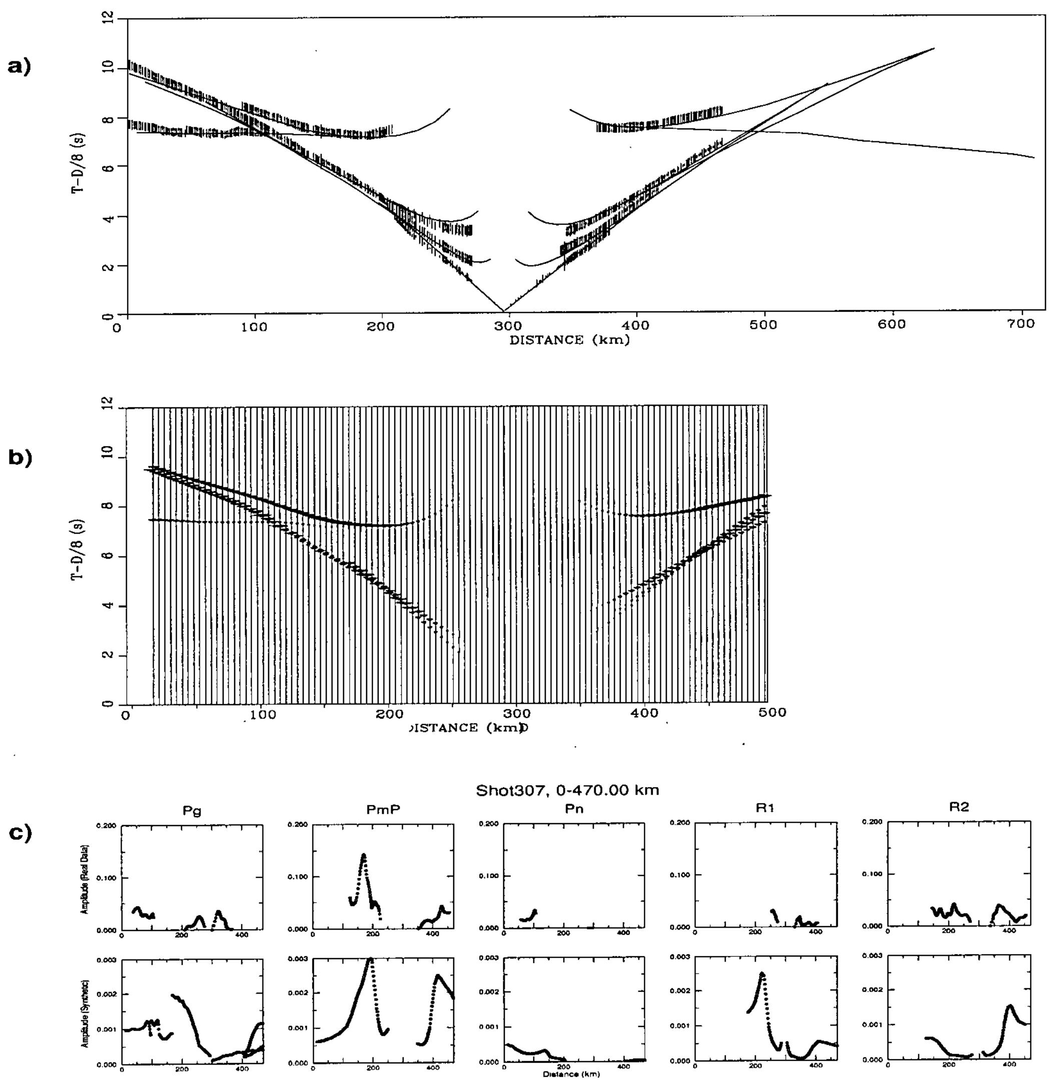

Figure 5.36: Shot 307. a) Fit between calculated and observed data. Vertical lines represent picking error of observed data. Calculated data are represented by a solid line. b) Synthetic seismogram sections. c) Comparison between true (above) and synthetic (below) amplitude trends.

a)

b)

c)

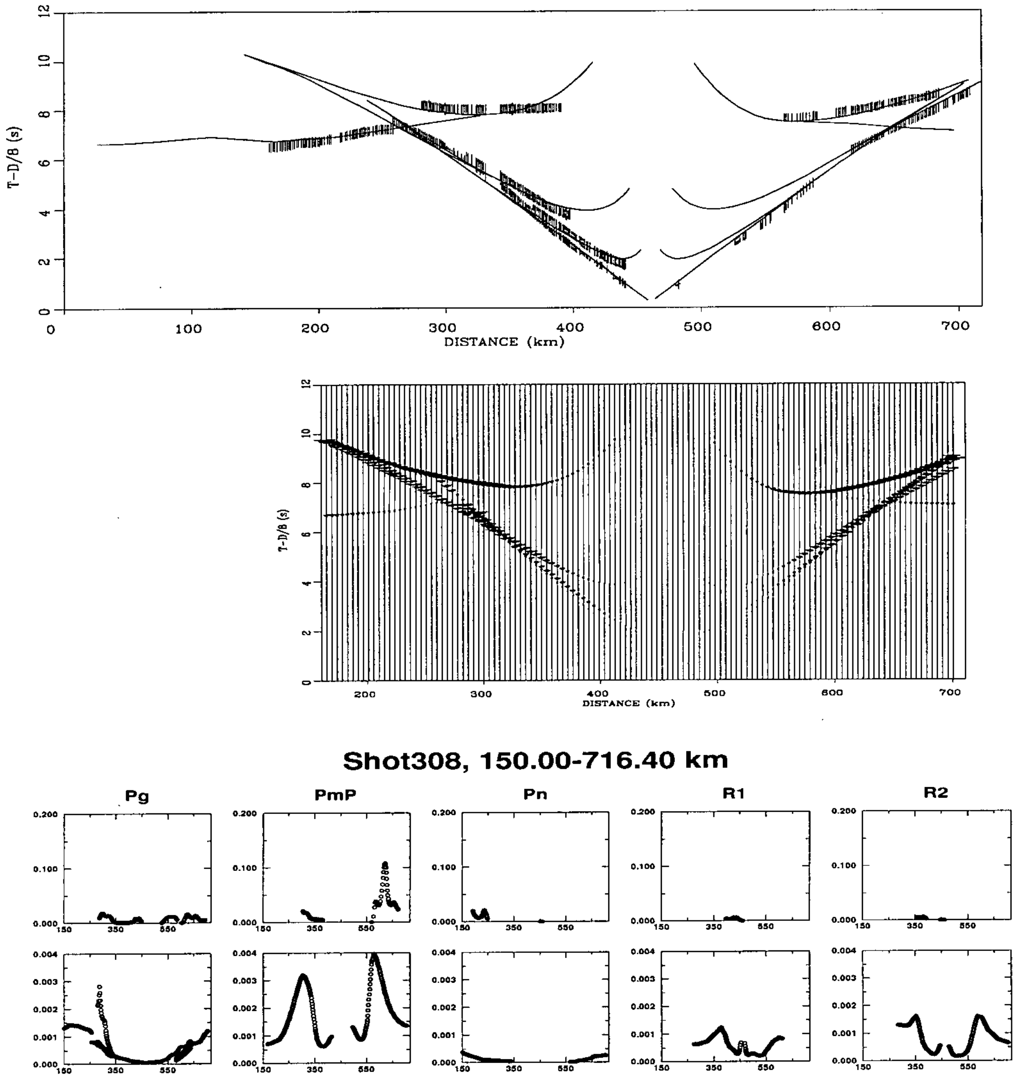

Figure 5.37: Shot 308. a) Fit between calculated and observed data. Vertical lines represent picking error of observed data. Calculated data are represented by a solid line. b) Synthetic seismogram sections. c) Comparison between true (above) and synthetic (below) amplitude trends.

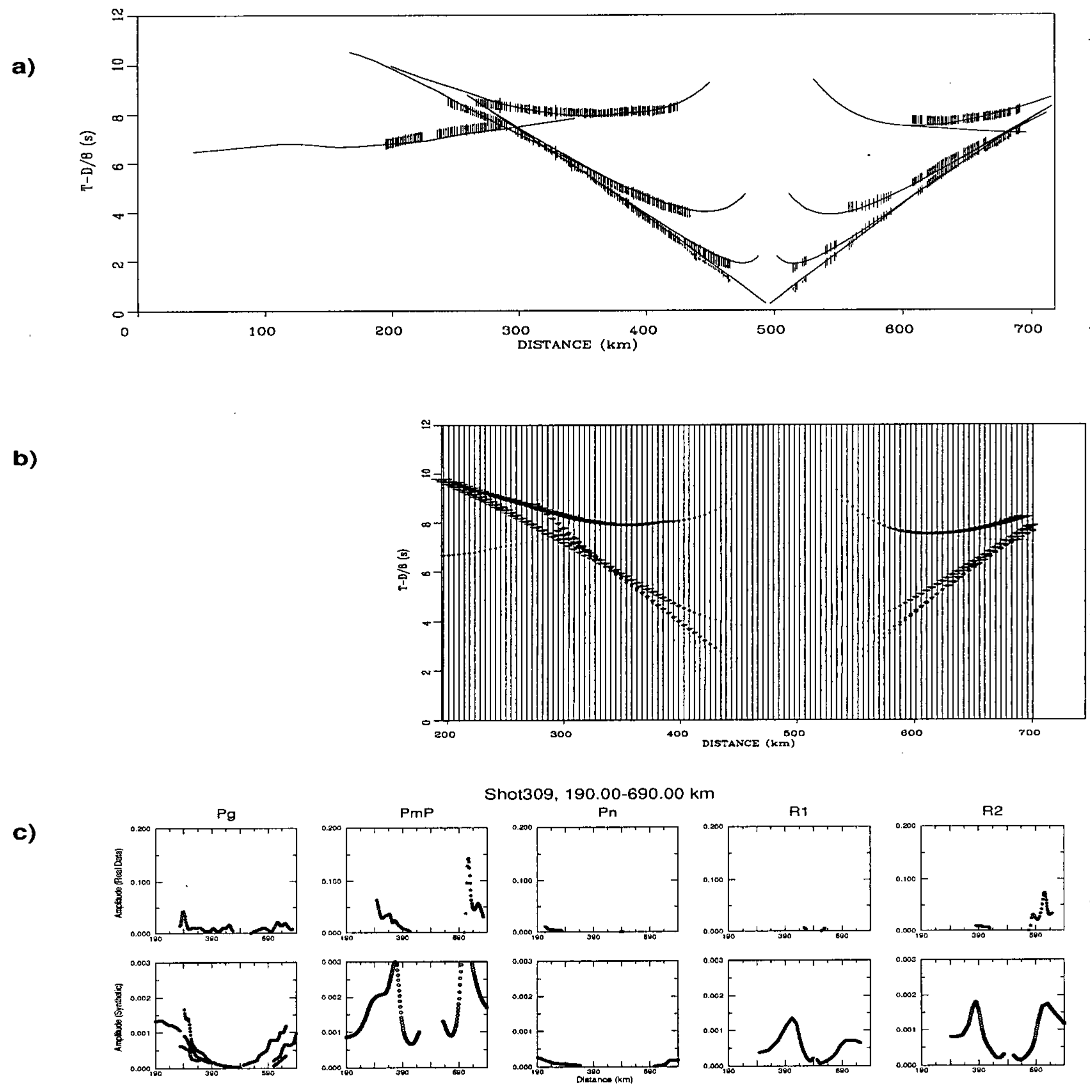

Figure 5.38: Shot 309. a) Fit between calculated and observed data. Vertical lines represent picking error of observed data. Calculated data are represented by a solid line. b) Synthetic seismogram sections. c) Comparison between true (above) and synthetic (below) amplitude trends.

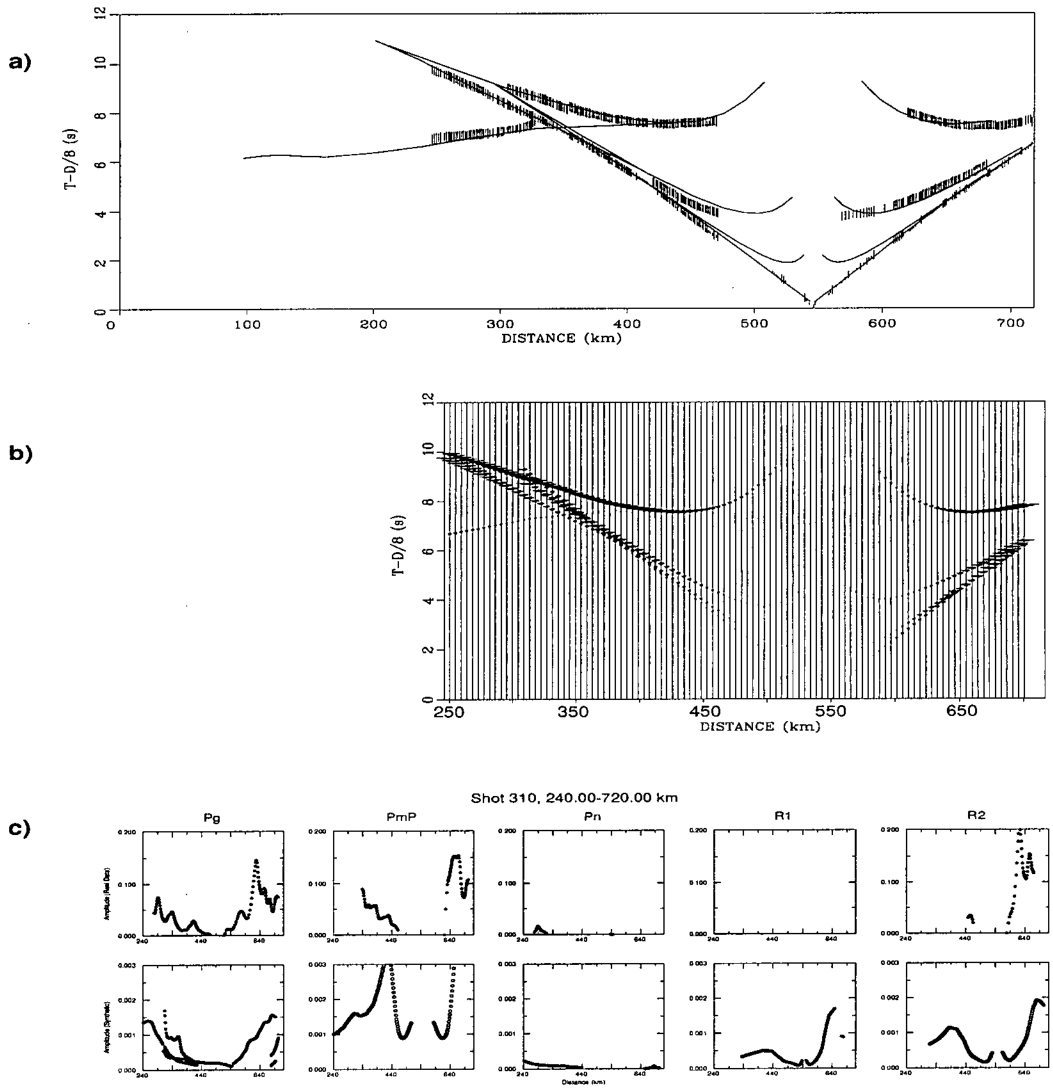

Figure 5.39: Shot 310. a) Fit between calculated and observed data. Vertical lines represent picking error of observed data. Calculated data are represented by a solid line. b) Synthetic seismogram sections. c) Comparison between true (above) and synthetic (below) amplitude trends.

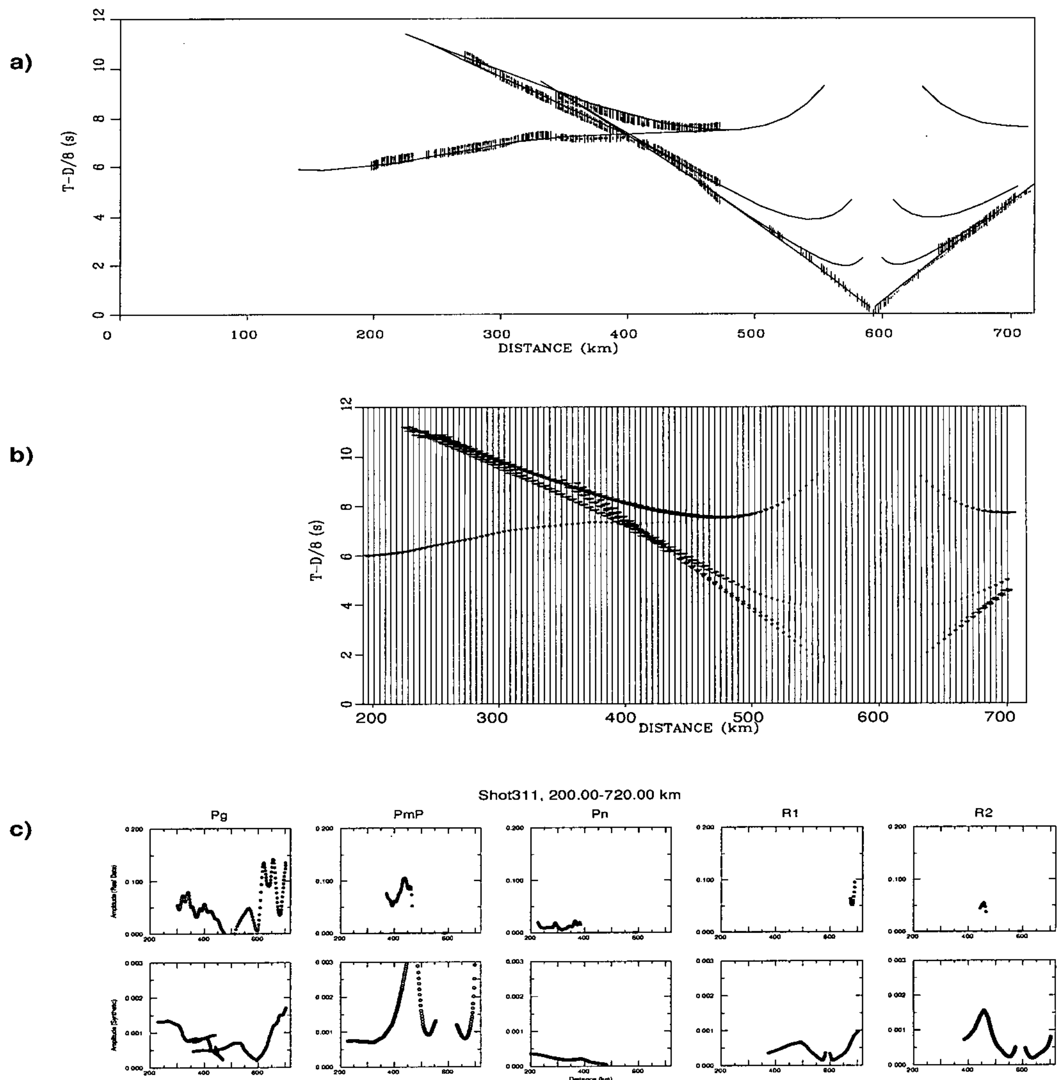

Figure 5.40: Shot 311. a) Fit between calculated and observed data. Vertical lines represent picking error of observed data. Calculated data are represented by a solid line. b) Synthetic seismogram sections. c) Comparison between true (above) and synthetic (below) amplitude trends.

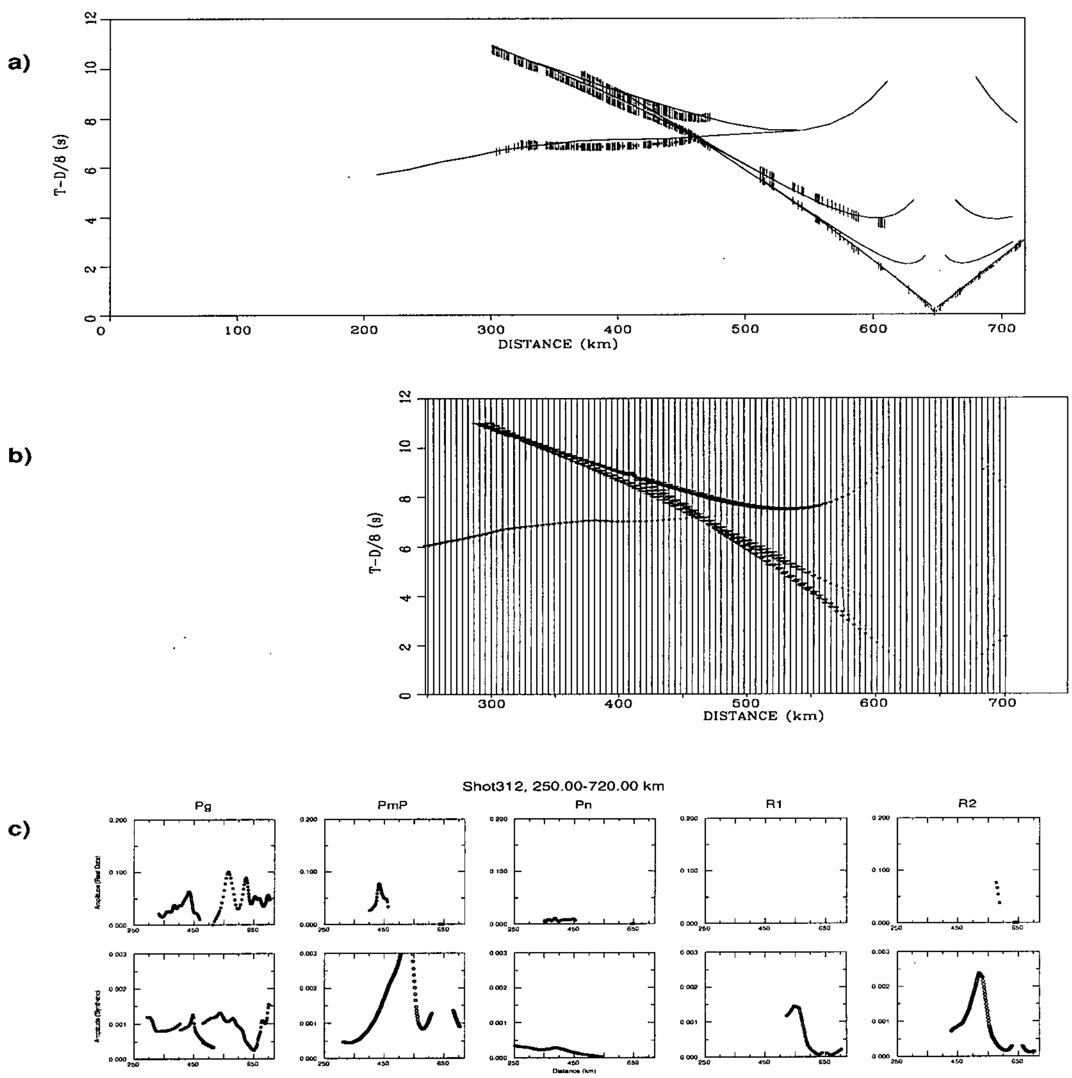

Figure 5.41: Shot 312. a) Fit between calculated and observed data. Vertical lines represent picking error of observed data. Calculated data are represented by a solid line. b) Synthetic seismogram sections. c) Comparison between true (above) and synthetic (below) amplitude trends.

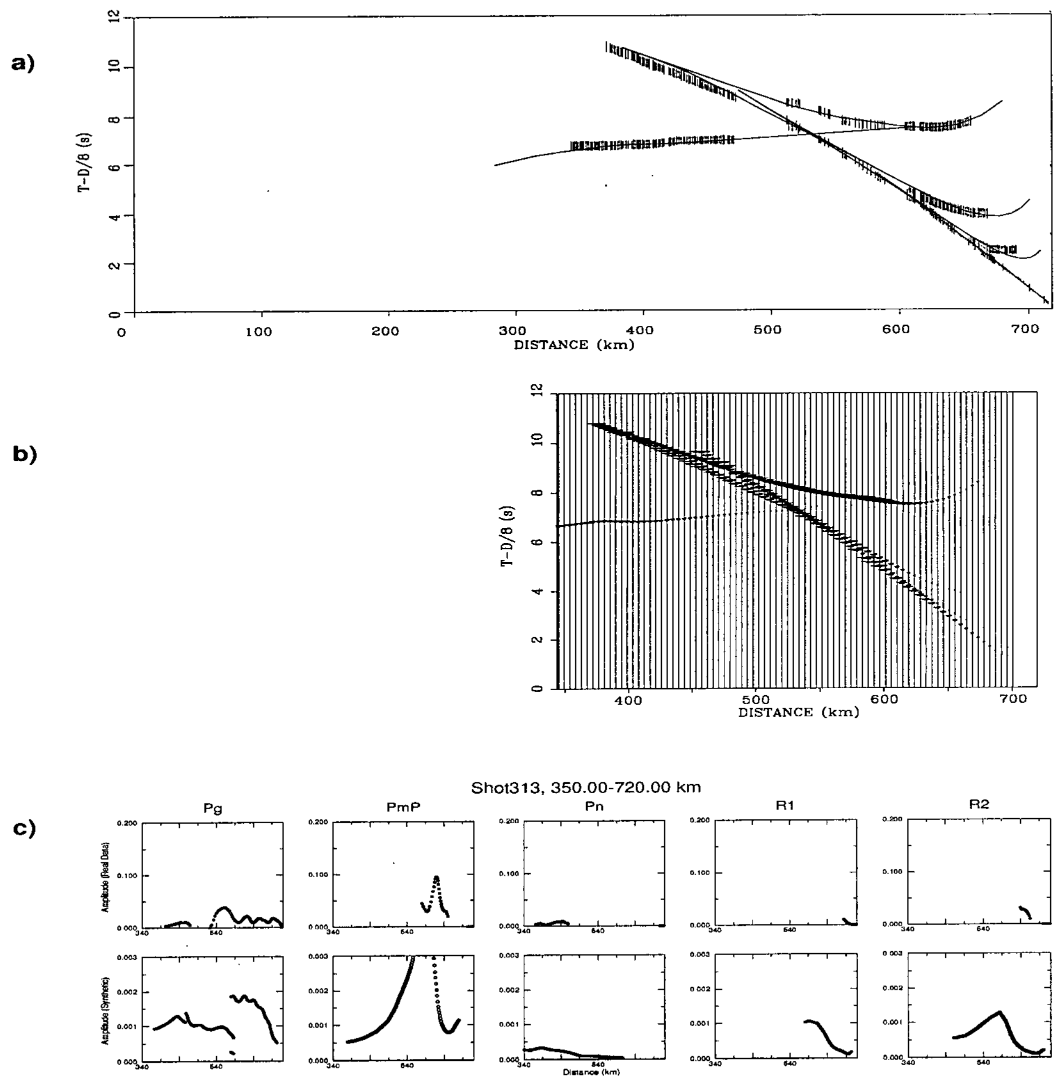

Figure 5.42: Shot 313. a) Fit between calculated and observed data. Vertical lines represent picking error of observed data. Calculated data are represented by a solid line. b) Synthetic seismogram sections. c) Comparison between true (above) and synthetic (below) amplitude trends.

6 Discussion and Conclusions

6.1 Comparison with other Geophysical Studies

The following compares the final model of this thesis to preliminary results of crustal thickness and mantle velocities for refraction line R3 as determined by another investigator, reflection data collected in this study area and previous refraction studies to the south.

6.1.1 Comparison with Preliminary Results of line R3

Using the wide-angle reflection arrivals of the THORE refraction data, Nemeth et al. (1996) define the deep architecture of the western THO with multi-fold reflection imaging of the upper mantle and the lowermost crust. It was possible to use standard reflection signal enhancement techniques with the PmP phase since the data had relatively high seismic fold and signal-to-noise ratio. They estimated, through trial and error, an average crustal velocity of 6.5 km/s to produce the results shown in Figure 6.1. Moho topography varies significantly with depths ranging from 40-52 km over approximately 100 km laterally. The crustal variations determined in this thesis are very similar, the differences being: a) the range in crustal thickness is slightly less (38-49 km), b) the anticlinal feature is more narrow by $\approx$ 75 km, and c) there is a sharp decrease in thickness near shot 312 ($\approx$ 650 km offset.) However, the area near shot 312 is not very well constrained in either study because it is very near the end of the line; thus not many rays are reflected. The importance of this comparison is that in both cases large crustal variations were determined using two different approaches. However, the crustal thickness in this thesis is believed to be better

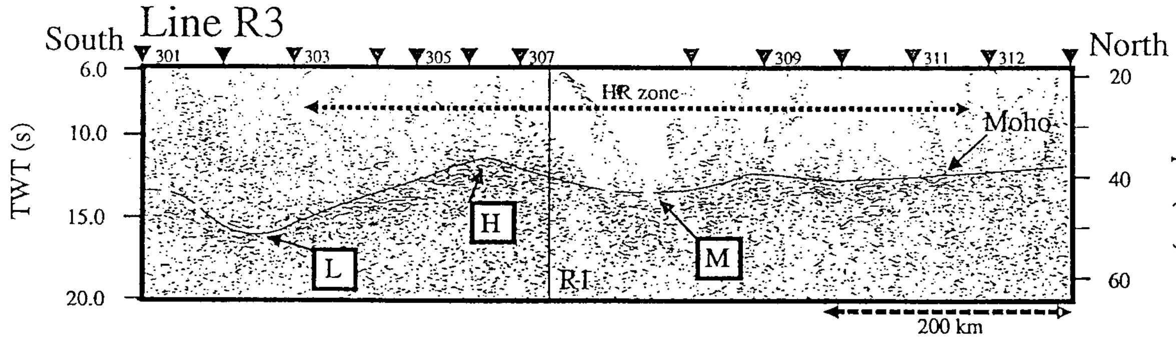

Figure 6.1: Automated line drawing plot of the stacked time sections line R3. The picked Moho is marked by a solid line. The vertical line indicates where R1 crosses. Solid black triangles mark approximate locations of the shot points. M=Moho, H=shallowest Moho, L=deepest Moho, HR=zone where Moho has strong reflective character (Nemeth et al., 1996)

constained since the velocities (average 6.5 km/s) of the overlying crustal layers (6.20, 6.35 and 6.7 km/s for the upper, mid and lower crust respectively) are more accurately determined through the inversion modelling technique which incorporates both vertical and horizontal velocity variations, whereas Nemeth et al. (1996) assume only one velocity (6.5 km/s) for the entire section.

Taking advantage of the unusually long profile lengths in THORE, a general velocity model of the sub-crustal lithosphere to depths of 160 km for line R3 was constructed by Hajnal et al. (1997) (Fig. 6.2). For their necessary ray tracing through the crust, a two-layer model with average velocities of 6.00 and 6.50 km/s was used. In the interpreted model, upper mantle velocities range from 8.1 to 8.3 km/s. A high velocity block with velocities of 8.35-8.45 km/s is situated between offsets of 260-350 km near the intersection of R1 and R3. In the final model of this thesis, this feature was also found, but extends from approximately 200-350 km and has a velocity of 8.42 km/s. Mantle velocities in this study range from 8.1-8.2 km/s. The resolution in both cases is the same; the slight differences between the models can be attributed to the assumption of an average velocity for the upper and lower crust as described in the previous paragraph and the inherent resolution available with the technique (e.g., Table 6, page 55.)

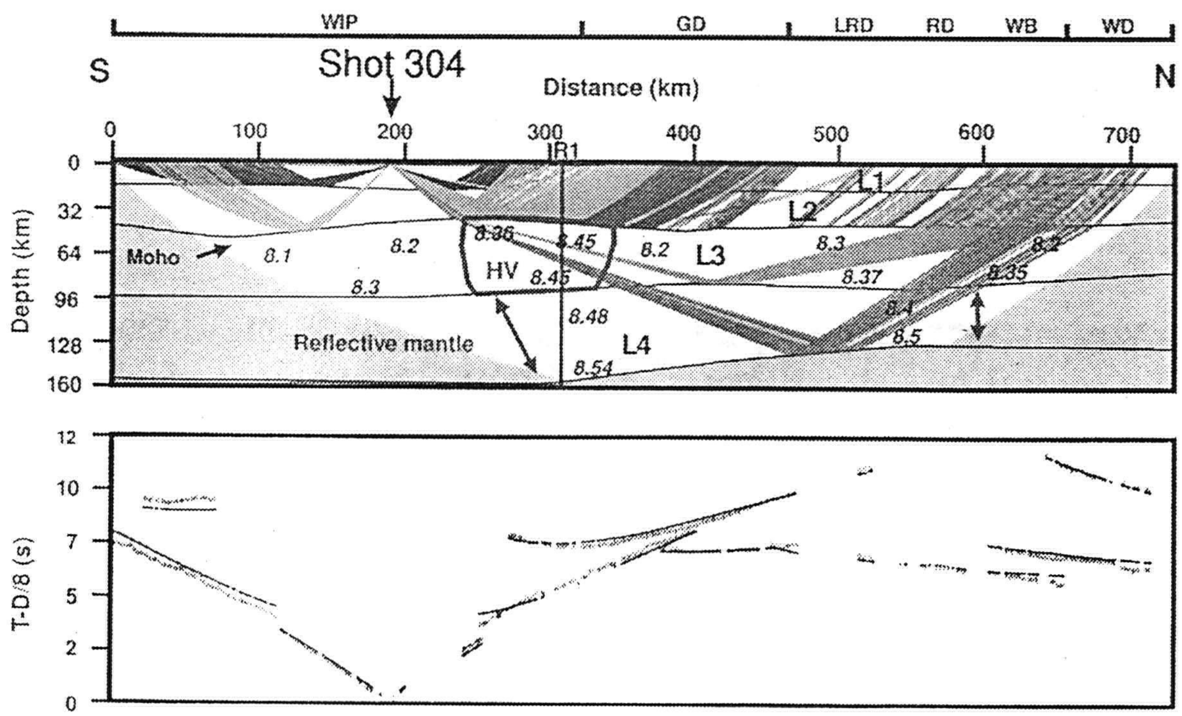

Figure 6.2: Interpreted velocity (km/s) model for line R3. Ray paths for shot 304 are illustrated. Crustal model: L1 (upper crust), average velocity (AV) 6.00 km/s; L2 (lower crust) , AV 6.50 km/s; L3 (uppermost mantle) AV 8.3 km/s; L4 (reflective mantle zone), AV 8.5 km/s (After Hajnal et al., 1997) .

6.1.2 Comparison with Reflection Data in the Area

In 1994, *LITHOPROBE* acquired 610 km of reflection data in the western THO to complement 1100 km of regional crustal reflection data acquired in 1991. The 1994 survey comprised one E-W line (line S1a, extending line 9 from the 1991 survey to the west) and three N-S trending lines (S2a, S2b and S2c; see Fig. 1.1) which are the main focus of this comparison. It is beyond the scope of this thesis to fully interpret the reflection data but it is useful to compare the reflections to the layer boundaries modelled using refraction data.

Line S2a, Figure 6.3, runs along the contact of the LaRonge and Glennie domains. There is a slight distinction between the upper and mid-crust at $\approx$4 seconds and between the mid- and lower crust at 8 seconds as well as a very prominent synclinal feature of $\approx$2 seconds depth at 275-375 km offset. The Moho is at 15 seconds, but it is not very clear. Superimposing the refraction data (after converting depth to time) over the reflection section at the corresponding offsets, a relatively good match is shown between the upper, mid- and lower crust. The Moho is deeper on the reflection section than on the refraction model by $\approx$1-2 seconds. This difference can be explained by the fact the reflection line is $\approx$ 100 km west of R3 and passes through a different part of the lithotectonic domains. As shown by the interpretation of Line 9 of the 1991 *LITHOPROBE* reflection survey (see Section **1.3.2**), the crustal structure and crustal thickness vary laterally across the orogen.

Line S2c (Fig. 6.3) images the crust beneath the Glennie domain covered by Phanerozoic sediments. Reflections off the mid- to lower-crust boundary are estimated to lie at around 24 km depth. The Moho reflection is at $\approx$14 seconds. The layer boundaries of the refraction model do not coincide with the reflections; the refraction Moho in this case is

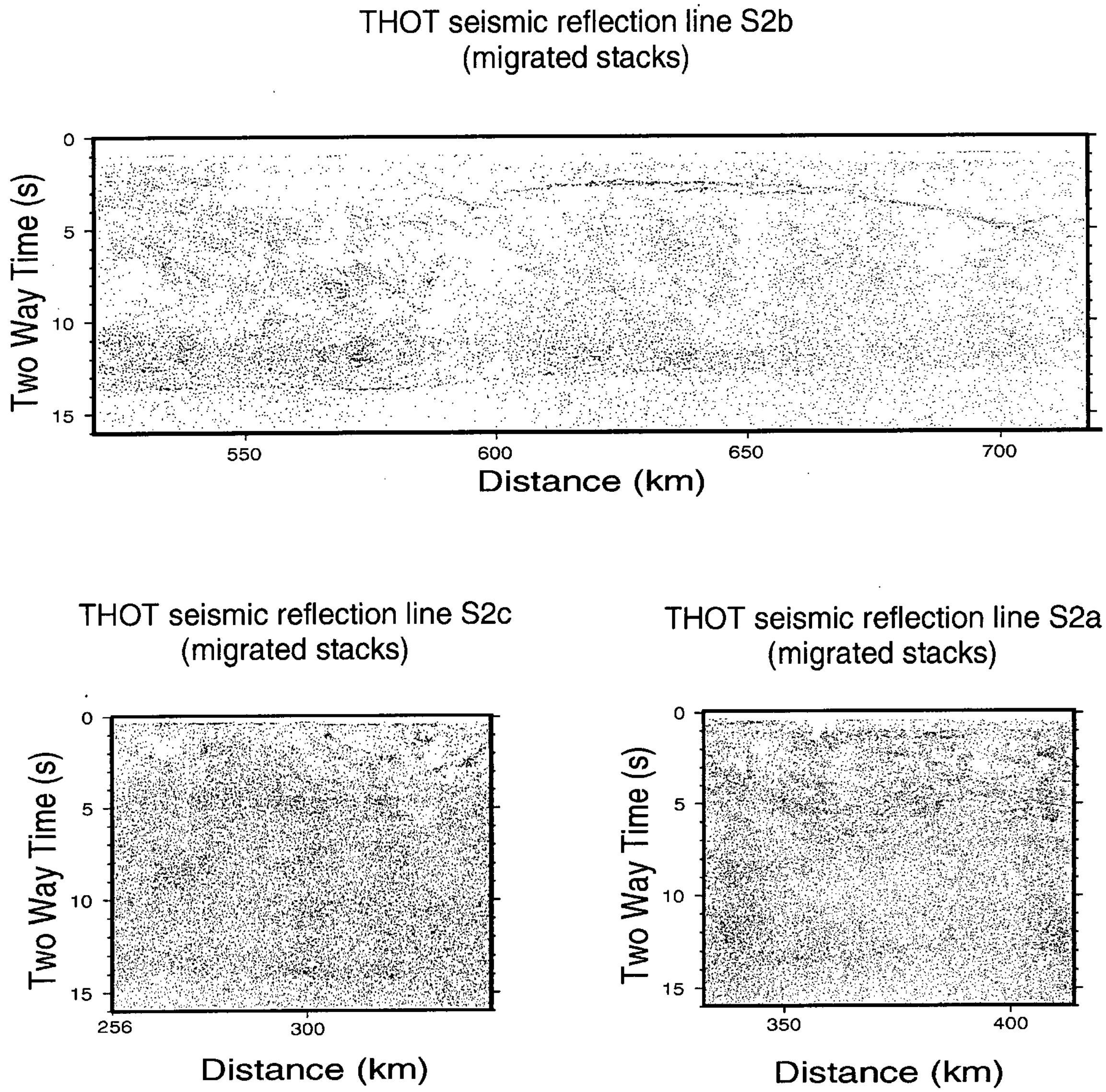

Figure 6.3: Reflection sections S2b, S2c and S2a.

≈1-2 seconds shallower. Such differences are to be expected since Line S2c intersects the interpreted crustal root of Line 9 (Fig. 1.6) and is located approximately 50 km west of line R3.

Line S2b runs along the northern 200 km of line R3. The southern section of the line has north-dipping reflections that flatten out in the lower crust. The reflections appear to thrust beneath the Peter Lake domain and terminate at ≈625 km offset. The base of thrusting is interpreted as the upper boundary of the Sask craton extended to the north. Another prominent feature is the high amplitude reflection at 2-4 seconds to the north. This is interpreted by Mandler and Clowes (1997) to be a sill. The sill terminates when it intersects the dipping reflection layers. It is not easy to distingush between the upper, mid- and lower crust, but the Moho reflectivity is relatively good. The crustal thickness decreases northward by ≈12-14 seconds. There is no clear connection between the upper and mid-crusts when superimposing the refraction model onto the reflection section. However, the refraction layer boundaries decrease from the end of the dipping reflectors towards the north. There is also a decrease of ≈0.1 km/s in velocity although the absolute uncertainties in determination of the velocity structures (see Table 6 and related discussion) cautions against attaching a lot of significance to this change. The Moho topography of the refraction model coincides very well with the Moho on the reflection section, thus confirming the crustal thickness in that region.

6.1.3 Comparison with other Refraction Studies

In 1977, 1979 and 1981, the Consortium for Crustal Reconnaissance Using Seismic Techniques (COCRUST) recorded over 2250 km of reversed in-line refraction data (Morel-à-l'Huissier, 1987). The crustal velocity models of lines D and E (Fig. 1.4 and 1.5) of that study, which lie just to the south of line R3 (Fig. 1.1), will be compared to the model of this thesis.

The northern point of line D is 20 km from the southern end of line R3. In Figure 1.4, the sediment layer has an average velocity of 5.5-5.75 km/s. The upper, mid- and lower crust thins towards the south from 10 km to 7 km with velocities of 6.12 and 6.41 km/s respectively. A 7.2 km/s layer was needed from 40-45 km (north) to 30-40 km (south) to fit the data. The upper mantle velocity was modelled at 8.4 km/s.

Line E, situated $\approx$ 60 km west of line D, has an upper crustal layer with velocities increasing from 6.13 km/s to 6.43 km/s over a depth extent of $\approx$ 12 km. A high-velocity layer in the lower crust of 7.0 - 7.2 km/s was required to fit the data. It has a domal shape with depths ranging from 38-30-35 km from north to south. The mantle velocity was determined at 8.4 km/s.

Comparing the above two models with the final model of this thesis, the following can be deduced. Models of lines D and E do not differentiate the mid and lower crust as the current model does. However, the velocities are similar at the same depths. The crustal thicknesses are also similar. The biggest difference is in the upper mantle velocities. The discrepancy of 0.3 km/s between the models could be attributed to the differences in the acquisition of the data. The COCRUST data are limited by a large and irregular receiver spacing, preventing the resolution of small-scale crustal structures. Also, PmP reflections were absent in some cases which limits the accuracy of the crustal thickness and structure.

6.2 Crustal Refraction Model within the Tectonics of the THO

The main objectives of this thesis were to determine the north-south extent of the Sask craton and to define the crustal velocity structure in the area.

To the south, the Sask craton extends beyond the most southern shot of line R3. This is further evidenced by drill core samples containing Archean material beneath the Phanerozoic cover in the Dakota segment of the orogen (Collerson et al., 1988, 1990). To the north however, the Sask craton is interpreted to thrust beneath the LaRonge, Rottenstone, Wathaman and Peter Lake domains terminating at the Wollaston fold belt. This interpretation stems primarily from the dipping reflectors of the reflection data S2b discussed in Section **6.1.2**, as well as the decreasing velocities (by 0.1 km/s) and crustal thickness by 1-3 km towards the north. The northern extent of the Sask craton constrained in the refraction model and the reflection data fits well with the hypothesis that an Archean craton collided to the south of the THO as described in Section **1.2**.

The crustal thickness in the region of line R3 varies significantly from 38-49 km along lateral distances of $\approx$ 100 km. Also, there is an anomalously high velocity zone in the mantle between 200-350 km distance (measured from the south end of line R3.) These features are well constrained by the data and model interpretation and are consistent with results of the other studies described above. The variation in crustal thickness does not coincide with major crust/lithosphere boundaries such as suture/paleo-subduction zones. Thus, it is believed to have formed due to post-collisional processes.

Baird et al. (1995) describe the processes contributing to the formation of the Williston Basin, some of which may directly apply to explain the varying crustal thicknesses apparent throughout the THO. Using reflection data from COCORP (Fig. 1.7), they describe how remanent crustal keels of the Archean craton (Dakota Block) can be altered through a metamorphic phase transition (eclogitization) increasing the density of the rock columns in the lower crust which in turn may cause the overlying crust to subside (Hamdani et al.,

1994) as in the case of the Williston Basin. It may also explain why the Moho reflections were more shallow than the expected 45 km derived from the refraction results of the CO-CRUST survey located about 100 km further north.

Eclogitization involves transforming lower-density, lower-velocity materials such as plagioclase to high density, high-velocity materials (garnets and omphatic pyroxenes). Eclogites exhibit compressional wave velocities in excess of 8 km/s (Manghnani et al., 1974), thus they would be considered mantle. As the eclogitization progresses upward, the crust-mantle boundary will also move, creating the 'new' Moho. The structural fabric formed during the THO collision is preserved with the 'new' Moho (M2) overprinting the older M1 Moho.

Using the data from the 1991 *LITHOPROBE* reflection section line 9 (Fig. 1.1), Hajnal et al. (1996) describe two ages of the Moho reflections based on cross-cutting relations (Fig. 6.4). The older Moho (labelled M2 in this case) is the preserved crustal root R and has sub-horizontal and dipping reflections parallel to those in the mid- and lower-crust. The younger, sub-horizontal Moho (M1) is at 37-40 km and its structure is attributed to ductile shear, possibly related with detachment at the crust-mantle boundary during post-collisional deformations. The younger Moho has reflectors parallel to some in the lower crust. However, using vertical-incidence reflection data with a dynamite source along the same line, Bezdán and Hajnal (1996) were able to see reflections parallel to the older Moho beneath M1 (Fig. 6.5). Because of this, the differences between the two are most likely caused by the heterogeous development of younger Moho associated with eclogitization as opposed to deformation of a single Moho.

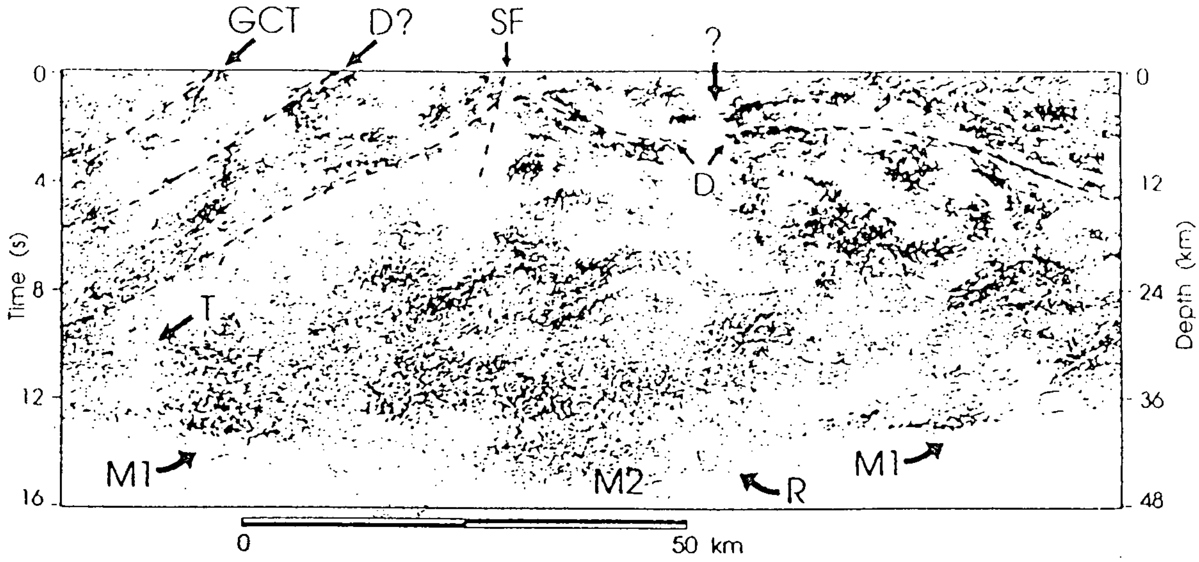

Figure 6.4: Migrated Vibroseis seismic reflection data from the culmination image on line 9. The Moho (M2) associated with the crustal root (R) is not defined by distinct subhorizontal reflections as is observed in the regions adjacent to the culmination (M1). After Hajnal et al. (1996)

The concepts described above can be used to explain the large variations in crustal thickness along line R3. To the south (between 25-200 km offset), the crust reaches a maximum depth of 49 km and has an average upper mantle velocity of 8.1 km/s. This is interpreted to be part of the remanent Archean keel that has not undergone eclogitization. Immediately to the north, the crust underlain by an anomalous high velocity layer reaches a minimum thickness of 38 km over a lateral distance of less than 150 km. This section is suggested to be a block of eclogitized crust, which thus has caused the Moho to be identified at more shallow depths. The crustal thicknesses to the north also vary along the profile with relatively high velocities. Perhaps the secondary Moho high from 500 - 650 km distance (Fig 5.2) can be considered to be crust at an earlier stage of eclogitization. The interpreted high velocities are within the range of eclogite compressional velocities of 7.9-8.5 km/s at

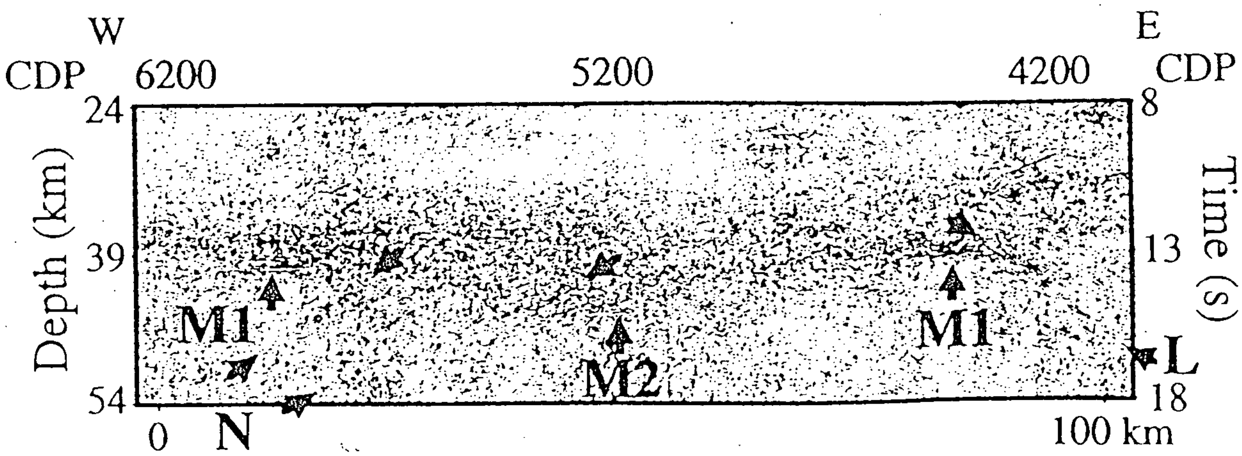

Figure 6.5: Migrated seismic reflections data derived from a dynamite source experiment along line 9. Image highlights both M1 and M2 Moho and also sub-Moho reflections that dip moderately to the east (L) and west (N). After Bezdán and Hajnal (1996)

20 km depth (Christensen and Mooney, 1995). Beneath the Wollaston fold belt however, the velocities drop to 8.1 km/s, but this value is not well constrained. Detailed analysis of the reflection data of lines S2a, S2b and S2c will provide a better understanding of the eclogitization processes and how they occured along line R3, if indeed this process is one of the causes of variability in crustal thickness.

The depths between the interpreted Moho of the line 9 reflection line interpretation (Fig 1.6) and the refraction model of R3 match at the intersection of the profiles. The question is why are there greater variations in crustal thickness running N-S as opposed to E-W? Also, why do certain areas of the Archean crust possibly undergo eclogitization while others only hundreds of km away do not? Perhaps certain portions of the lower crust differ significantly making them more or less susceptible to metamorphism. It is unclear why this may occur, but perhaps it is the result of changing the properities of some sections of the lower crust as the Sask craton moved towards the NE. The crustal velocity model of this thesis, and particularly reflection line S2b, show the northern extent of the Sask craton. Thus the southern section of line R3 would be the bounding position of the collision and deformation may be more extensive in this area, making the lower crust more prone to eclogitization. It would explain why the crustal thicknesses vary more N-S than E-W. Much more study is needed to ascertain that hypothesis. Heat flow studies to date do not indicate significant temperature variations to cause regional eclogitization in this area.

Another interesting feature is the occurance of a diamondiferous kimberlite field just above the mantle high where velocities are $\approx$8.4 km/s at the southern section of line R3. The varying velocities and structure found here are comparable to those in several regions of the Siberian craton which also yield diamondiferous kimberlies (Pavlenkova et al., 1996). Why this occurs is unclear, but this velocity model may help solve the problem since it is very well constrained and would be a good working model. Much more study needs to be done to answer these questions.

6.3 Final Conclusions

Through extensive inversion modelling and amplitude comparisons, a crustal velocity model was constructed for line R3 of the 1993 Trans-Hudson Orogen Refraction Experiment with the help of Jonathan (Fig. 6.6).

It was determined that crustal velocities decreased steadily northward, but the crustal thickness varied ≈10 km over relatively short lateral distances of 100 km. A zone of high upper-mantle velocity was found beneath the shallowest segment of the crust.

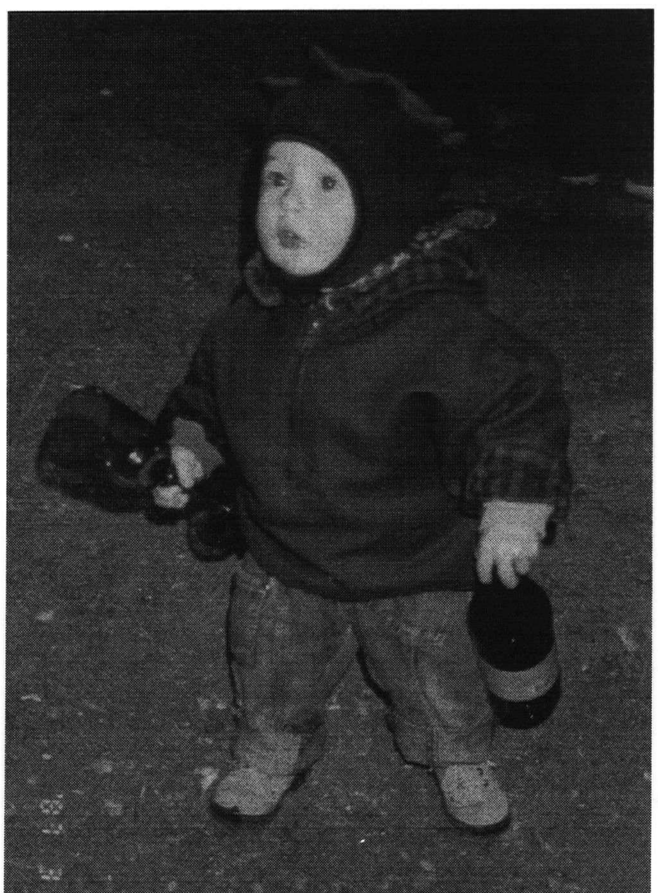

Figure 6.6: Jonathan helping Denise gain valuable insight into seismic sections.

The decreasing velocities towards the north and the terminations of dipping structures in the S2b reflection section suggest the northern extent of the Sask craton thrusts beneath the LaRonge, Rottenstone, Wathaman and Peter Lake domains terminating below the Wollaston fold belt.

Variations of crustal thickness and upper mantle velocities are explained by the process of eclogitization in which lower density, lower velocity materials in the lowermost crust are metamorphosed to high-density, high-velocity materials. Exactly why this occurs in this particular region is uncertain. Perhaps the thrusting of the thick (?) Archean craton alters the state of the lower crust making it more susceptible to eclogitization. Much further study is needed to justify this hypothesis.

References

Amor, J. 1996. PLOTSEC: Generalised Software for Seismic Refraction Data *LSPF Newsletter*, **23**, 1039-1043.

Anderson, T.W. , 1971. *An Introduction to Multivariate Statistical Analysis*, Wiley, New York.

Ansdell, K. M., S. B. Lucas, K. Connors and R. A. Stern, 1995. Kisseynew metasedimentary gneiss belt, Trans-Hudson Orogen (Canada): back-arc origin and collisional inversion, *Geology*, **9**, 24-31.

Aspler, L.B., and J.R. Chianrenzelli, 1996. Stratigraphy, sedimentology and physical volcanology of the Henik Group, central Ennadai-Rankin greenstone belt, Northwest Territories, Canada; late Archean paleogeography of the Hearne Province and tectonic implications, *Precambrian Research*, **77**, 59-89.

Bailes, A.H. and E.C. Syme, 1989. Geology of the Flin Flon-White Lake area, *Manitoba Energy Min. Geol. Rep. GR87-1*, 313 pp.

Baird, D. J., J. H. Knapp, D.N. Steer, L.D. Brown, K.D. and K.D. Nelson, 1995. Uppermantle reflectivity beneath the Williston basin, phase-change Moho and the origin of intracratonic basins, *Geology*, **23**, 431-434.

Baird, D. J., K.D. Nelson, J. H. Knapp, J.J. Walters and L.D.Brown, 1996. Crustal structure and evolution of the Trans-Hudson orogen: Results form seismic reflection profiling, *Tectonophysics*, **264**, 101-109.

Bezdàn, S. and Z. Hajnal 1996. Coincident vibroseis and dynamite surveys across the western flank of the Trans-Hudson Orogen, *Tectonics*, **15**, 416-426.

Bickford, M.E., K.D. Collerson, J.F. Lewry, W.R. Van Schmus and J.R. Chianrenzelli, 1990 . Proterozoic collisional tectonism in the Trans-Hudson Orogen, Saskatchewan, *Geology*, **18**, 14-18.

Bzdel, L., Z. Hajnal, B. Nemeth, M. Argyle, I. Asudeh, D. White, D.A. Forsyth, B. Roberts, R.M. Clowes, R.M. Ellis, P. Carroll, G. Spence, W. Kohler and M. Alvarez 1995. The 1993 Trans-Hudson Orogen Refraction Experiment (THORE): Deployment, Acqusition and Processing Report. *LITHOPROBE Report*, **43**, and *Geological Survey of Canada Open File* **3025**.

Červený, V., I. Molotkov, and I. Pšenčik 1977. *Ray method in seismology*, Charles University Press, Prague.

Christensen, N.I., and W.D. Mooney, 1995. Seismic velocity structure and composition of the continental crust: A global view *Journal of Geophysical Research*, **100**, 9761-9788.

Clowes, R.M. (editor) 1993. LITHOPROBE Phase IV Proposal: Studies of the Evolution of a Continent, *LITHOPROBE Secretariat*, 290 pp.

Collerson, K.D., R.W. Van Schmus, J.F. Lewry and M.E. Bickford, 1988. Buried Precambrian basement in south-central Saskatchewan: Provisional results for Sm-Nd model ages and U-Pb zircon geochronology, *Misc. Rep., Sask. Geol. Surv., Sask*, **88** , 142-150 .

Collerson, K.D., J.F. Lewry, M.E. Bickford and R.W. Van Schmus, 1990. Crustal evolution of the buried Precambrian of southern Saskatchewan: Implications for diamond exploration, *Modern Explorations Techniques, Special Publication*, **10**, 150-165 .

Gordon, T.M., P.A. Hunt, A.H. Bailes and E.C. Symes, 1990. U-Pb ages from the Flin Flon and Kisseynew belts, Manitoba: Chronology of crust formation at an Early Proterozoic accretionary margin in: J. F. Lewry and M. R. Stauffer (eds.), The early Proterozoic Trans-Hudson Orogen of North America, *Geological Association of Canada Special Paper*, **37**, 177-199.

Hajnal, Z., S.Lucus, D. White, J. Lewry, S. Bezdàn, M.R. Stauffer and M.D. Thomas, 1996 Seismic reflection images of the high angle faults and linked detachment in the Trans-Hudson Orogen. *Tectonics*, **15**, 427-439.

Hajnal, Z., B. Nemeth, R. M. Clowes, R. M. Ellis, G. D. Spence, M. J. A. Burianyk, I. Asudeh, D. J. White, D. A. Forsyth, 1997. Mantle involvement in lithospheric collision: seismic evidence from the Trans-Hudson Orogen, western Canada, *Geophysical Research Letters*, **24**, 2079-2082.

Halden, N.M., G.S. Clark, M.T. Corkery, P.G. Lenton and D.C.P. Scledewtiz, 1990. Trace element and Rb-Sr whole-rock isotopic constraints on the origin of the Chipewan, Thorsteinsson and Baldock batholiths, Churchill Province, Manitoba in: J. F. Lewry and M. R. Stauffer (eds.), The early Proterozoic Trans-Hudson Orogen of North America, *Geological Association of Canada Special Paper*, **37**, 201-214.

Hamdani, Y., J.C. Mareschal, and J. Arkani-Hamed, 1994. Phase change and thermal subsidence of the Williston basin, *Geophysical Journal International*, **116**, 585-597.

Hoffman, P. F., 1988. United plates of America, the birth of a craton: early Proterozoic assembly and growth of Laurentia, *Ann. Rev. Earth and Planet .Sciences* , **16**, 543-603.

Hoffman, P. F., 1989. Precambrian geology and tectonic history of North America, *The Geology of North America-An Overview* , 447-512.

Lewry, J. F. and K. D. Collerson, 1990. The Trans-Hudson Orogen: extent, subdivision, and problems, in: J. F. Lewry and M. R. Stauffer (eds.), The early Proterozoic Trans-Hudson Orogen of North America, *Geological Association of Canada Special Paper*, **37**, 1-14.

Lewry, J. F., 1981. Lower Proterozoic arc-microcontinent collisional tectonics in the western Chruchill Province, *Nature*, **294**, 69-72.

Lewry, J. F. and M. R. Stauffer (editors), 1990. The early Proterozoic Trans-Hudson Orogen of North America, *Geological Association of Canada Special Paper*, **37**, 507 pp.

Lewry, J. F. and T.I. Sibbald, 1980. Themotectonic evolution of the Chruchill Province in northern Saskatchewan, *Tectonphysics*, **68**, 45-82 pp.

Lewry, J. F., Z. Hajnal, A. Green, S. B. Lucas, D. White, M. R. Stauffer, K. E. Ashton, W. Weber and R. Clowes, 1994. Structure of a Paleoproterozoic continent-continent collision zone: a LITHOPROBE seismic reflection profile across the Trans-Hudson Orogen, Canada, *Tectonophysics*, **232**, 143-160.

Lewry, J.F., D.J. Thomas, R. Macdonald and J. Chiarenzelli, 1990. Structural relations in accreted terranes of the Trans-Hudson Orogen, Saskatchewan: Telescoping in a collisional regime? in: J. F. Lewry and M. R. Stauffer (eds.), The early Proterozoic Trans-Hudson Orogen of North America, *Geological Association of Canada Special Paper.*, **37**, 177-199.

Lewry, J., S. Lucas, R. Stern, K. Ansdell and K. Ashton, 1996. Tectonic assembly and orogenic closure in the Trans-Hudson Orogen, *Geological Association of Canada Annual Meeting*, Abstracts, p. A56.

Lewry, J.F., M.R. Stauffer, S. Fumerton, 1981. A Cordilleran-type batholithic belt in the Churchill Province in northern Saskatchewan. *Precambrian Research*, **14**, 277-313.

Loève, M., 1951 *Probability Theory*, Van Nostrand, Princeton, New Jersey.

Lucas, S. B., A. Green, Z. Hajnal, D. White, J. Lewry, K. Ashton, W. Weber and R. Clowes, 1993. Deep seismic profile across a Proterozoic collision zone: surprises at depth, *Nature*, **363**, 339-342.

Mandler, H., R.M. Clowes, 1997. Evidence for extensive tabular intrusions in the Precambrian shield of western Canada: A 160-km-long sequence of bright reflections, *Geology*, **25**, 271-274.

Manghnani, M.H., R. Ramananantoandro, and S.P. Clarke Jr., 1974. Compressional and shear wave velocities in granulite facies rocks and eclogites to 10 kbar *Journal of Geophysical Research*, **79**, 5427-5446.

Meyers, M.T., M.E. Bickford and J.F. Lewry 1992. The Wathaman Batholith, an early Proterozoic continental arc in the Trans-Hudson orogenic belt, Canada, *Geological Society of America Bulletin*, **104**, 1073-1085.

Morel-à-l'Huissier, P., A. G. Green and C. J. Pike, 1987. Crustal refraction surveys across the Trans-Hudson Orogen - Williston Basin of south central Canada, *Journal of Geophysical Research*, **92**, 6403-6420.

Nemeth, B., Z. Hajnal and S. B. Lucas, 1996. Moho signature from wide-angle reflections: Preliminary results of the 1993 Trans-Hudson Orogen refraction experiment, *Tectonophysics*, **264**, 111-122.

Pavlenkova, N.I., G.A. Pavlenkova and L.N.Solodilove, 1996. High velocities in the upper mantle of the Siberian craton, *Tectonophysics*, **262**, 51-65.

Singh, S. and R.B. Herrmann, 1983. Regionalization of crustal coda Q in the continental United States, *Journal of Geophysical Research*, **88**, 527-538.

Stauffer, M.R., 1984. Manikewan: an Early Proterozoic ocean in Central Canada, its igneous history and orogenic closure, *Precambrian Research*, **25**, 257-281.

Stern, R.A., E.C. Symes, A.H. Bailes, A.G. Galley, D.J. Thomas, and S.B. Lucus. 1992. Nd-isotropic stratigraphy of Early Proterozoic Amisk Group metavolcanic rocks from the Flin Flon belt, Manitoba and Saskatchewan. In: Tadiogenic Age and Isotopic Studies *Geological Survey of Canada Paper*, **92-2**, 73-84.

Syme, E.C. 1990. Stratigraphy and geochemistry of the Lynn Lake and Flin Flon metavolcanic belts, Manitoba in : J. F. Lewry and M. R. Stauffer (eds.), The early Proterozoic Trans-Hudson Orogen of North America, *Geol. Assoc. Can. Spec. Pap.*, **37**, 143-162.

Ulrych, T.J., M.D. Sacchi and L.M. Freire, 1998. Eigenimage processing of seismic sections, *in Geophysical Development Series Volume: Covariance analysis for seismic signal processing*, Chapter 12, Society of Exploration Geophysics, Tulsa, in press.

Van Schmus, W.R., M.E. Bickford, J.F. Lewry, and R. Macdonald, 1987. U-Pb geochronology in the Trans-Hudson Orogen, northern Saskatchewan, Canada, *Canadian Journal of Earth Sciences*, **24**, 407-424.

Walters, B.R., and J. Pearce, 1987. Metavolcanic rocks of the La Ronge domain in the Chruchill Province, Saskatchewan: evidence for a volcanic arc origin, *Geological Society of London Special Publication*, **33**, 167-182.

Zelt, C.A. and R.M. Ellis, 1988. Practical and efficient ray tracing in 2-D media for rapid traveltime and amplitude forward modelling, *Canadian Journal of Exploration Geophysics*, **24**, 16-31.

Zelt, C.A., and R.B. Smith, 1992. Seismic traveltime inversion for 2-D crustal velocity structure, *Geophysical Journal International*, **108**, 16-34.

Zwanzig, H.V., 1990. Kisseynew gneiss belt in Manitoba: stratigraphy, structure and tectonic evolution in: J. F. Lewry and M. R. Stauffer (eds.), The early Proterozoic Trans-Hudson Orogen of North America, *Geological Association of Canada Special Paper*, **37**, 95-120.

A Description of PLOTSEC routines

Plotsec is a combination of software routines for handling seismic refraction and wide-angle reflection data from SEG-Y files. It includes algorithms for header updating, simple stacking of data by offset, amplitude/phase spectrum, slant-stack, interactive phase picking, merging of multiple data sets in time and/or offset, reading/writing SEG-Y files, reading/writing MATLAB matrix files, writing INSIGHT data files, and creating postscript output sections.

plotsec_raw: reads most types of SEG-Y data (even some non-standard) and can do various types of trace selection or resampling.

plotsec_segy: creates a SEG-Y file.

plotsec_pick: picks phases and displays plotsec data. It can also be used for setting up mutes and select traces for removal.

plotsec_plot creates plots of true offset in traditional wiggle/variable area or colour amplitude. It is capable of displaying traces scaled in relative or true amplitude as well as "reducing" the plotted time axis using a scaling or reducing velocity to compress the time axis. The output formats include postscript file creation or display in an X11 window. Other features include the overlay of picked phases, the application of reference lines, an offset based plot on the top of the section displaying any header value or combination, location map with shot and receiver locations, a comment box.

plotsec_update: updates header information. Includes updating of shot and receiver information obtained from survey files, recalculation of offset/azimuth from updated shot/receiver locations, application of time correction headers, the transfer of header information from one keyword to another, and selectively writing values into header word by all traces, or by keyword selected traces.

plotsec_win: applies various windowing operations (in traces and in time) to the data file. In Traces: Data can be windowed in traces by trace sequential range or by offset range. The offset range can be modified by the azimuthal range over which it is either positive or negative. In Time: Data can be windowed in time (with or without a reduction velocity) or relative to picked phase horizon (so many seconds before and after a picked phase time).

plotsec_filt applies various filter operations to the data file such as: the application of trace mutes from a mute file, the application of trace kills from a mute file, the application of a bandpass filter, scale all data values by a constant, scale selected traces by keying on a header word.

plotsec_spec: calculates the amplitude or phase spectrum of each trace of the input data set and outputs the result in section format. This would be best viewed using a colour plot.

plotsec_stk: combines data from similar offset ranges in the hope of improving the signal-to-noise ratio, or for the purpose of creating a data set with evenly sampled offsets. The time alignment of data to stack can be by reducing velocity or directly sample to sample.

In combination with plotsec_win, the later method can be used to stack along a picked phase horizon.

plotsec_taup: A program to transform an ordinary refraction data set from x-t space to tau-p space.

plotsec_mat: translates a plotsec head/data set in to a MATLAB matrix file (.mat), or reads a matrix file and produces a plotsec data file. Note the reverse process does not produce a head.dmp file, the translation from matrix to plotsec data is only intended for retrieving data that has already been translated. The matrix file must also not change size or ordering after creation. Data can be pre-flattened to a horizon (phase pick) or windowed using plotsec_win before creating the matrix file. You may also wish to decimate the data since the maximum matrix size is 1,000,000 points.

plotsec_elcor: calculates a simple terrain correction. This routine includes input variables for: water depth and velocity, sediment thickness and velocity, basement velocity, initial surface ray angle (or angle below basement), turning ray velocity

plotsec_amppk: calculates the amplitude and the uncertainty of each pick in a pick file. The uncertainty is selected by comparing the energy before and after the pick. The ratio of these two is taken as the signal-to-noise ratio.

plotsec_tranpk: translates picks from one pick format to another and can also map picks from one line to another by matching offsets.

Further details can be found on the plotsec website, http://www.geop.ubc.ca/~amor/plotsec.html.